Structure-Performance Relationships in the Selective Catalytic Reduction of Nitric Oxide with Ammonia over Copper-Based Zeolites

Structure-Performance Relationships in the Selective Catalytic Reduction of Nitric Oxide with Ammonia over Copper-Based Zeolites

Relatie tussen Structuur en Activiteit van Koperhoudende Zeolieten voor de Selectieve Katalytische Reductie van Stikstofoxide met Ammoniak

(met een samenvatting in het Nederlands)

Proefschrift

ter verkrijging van de graad van doctor aan de Universiteit Utrecht op gezag van de rector magnificus, prof.dr. H.R.B.M. Kummeling, ingevolge het besluit van het college voor promoties in het openbaar te verdedigen op

maandag 10 oktober 2022
des middags te 2.15 uur

door

Xinwei Ye

geboren op 2 maart 1993
te Guangdong, China

Promotor:
Prof. dr. B.M. Weckhuysen

Co-promotoren:
Dr. F. Meirer
Dr. J.E. Schmidt

TABLE OF CONTENTS

CHAPTER **1**

Introduction

1.1   Heterogeneous Catalysis and Zeolites

### 1.1.1   Heterogeneous Catalysis

A catalyst is generally defined as a substance that accelerates a reaction but is not consumed.[1] The addition of a catalyst has no effect on the thermodynamic equilibrium of a reaction. Rather, by lowering the activation energy it enhances the reaction rate, and therefore catalysis is purely a kinetic process.[1,2] Ideally, a catalyst affects the rate of the desired reaction by allowing an energetically favorable pathway, while not catalyzing undesired side reactions. The efficiency of a catalytic reaction is evaluated by determining the activity and selectivity of this reaction. The activity indicates how fast the reaction proceeds, while the selectivity is expressed by the ratio of the desired products to the total amount of products.[3] A higher yield of the desired product can be achieved by either increasing reaction activity or lowering the formation of undesired byproducts.

Catalytic processes are vital in various sectors such as in the petrochemical industry, pharmaceutical industry or in environmental applications. Catalysis is usually divided into heterogeneous catalysis, homogeneous catalysis and biocatalysis, among which heterogeneous catalysis contributes the most to the modern chemical industry in terms of produced products. It has been reported that 8 of the 10 most produced synthetic chemicals rely on heterogeneous catalysts in the US, and 90% of all chemical processes are performed by heterogeneous catalysts.[1,4] Heterogeneous catalysis involves multiple phases in a reaction, i.e., the catalyst is a different phase from the reaction mixture.[5] Usually, a solid catalyst is employed in a gas phase reaction or a liquid phase reaction, which facilitates the separation of catalysts and products. The heterogeneous catalytic reaction consists of the following elementary steps: the diffusion of reactants to the catalyst, the adsorption of reactants on the catalyst's surface, the catalyzed reaction at the surface, desorption of products and diffusion of the products away from the catalyst. This implies the great importance of the surface properties of a heterogeneous catalyst as catalyst surface provides binding sites for direct contact with reactant molecules and the subsequent catalyzed reaction. Therefore, catalysts with a large surface area are beneficial to host large amounts of accessible active sites. Solid catalysts are classified into supported metal catalysts (either metallic, metal oxide or metal sulfide), and acid or base catalysts.[2] As many industrial processes require high reaction temperatures as well as high pressures, solid catalysts are required to be thermally and mechanically robust.

1.1.2 Zeolites as Catalysts

Zeolites are naturally-occurring crystalline materials that consist of silica and alumina. Since the discovery of synthetic zeolites in 1950s, they have been under intensive investigation because of their proven potential as adsorbents and catalysts in industrial processes.[6,7] Zeolites are typically classified as solid acid catalysts, but there are also examples of zeolite catalysts with basic or metallic sites.
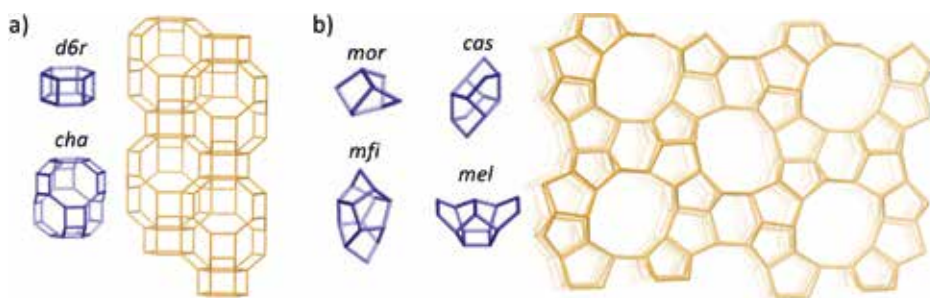
Figure 1.1 The composite building units and topology of zeolite a) CHA (viewed along [001]) and b) MFI (viewed along [010]). Reproduced from the International Zeolite Association (IZA) database of zeolite structures.[8]

Depending on the structure of the zeolite, it possesses an ordered microporous structure of channels that may be interconnected and present in one, two or three dimensions.[2] The primary building units of zeolites are the tetrahedral silica [SiO_4] and tetrahedral alumina [AlO_4]$^-$ with a negative charge. By sharing the corner oxygens in the tetrahedron, the primary building units are connected into Secondary Building Units (SBUs) and further into rings and cages, finally forming a 'continuous' zeolite framework.[2] The structure of a zeolite framework depends on the types and the tilling arrangements of the building units, resulting in small, medium, and large pore zeolites. Figure 1.1 shows the topology and the composite building units of two industrially important zeolites, CHA and MFI.[8] The small pore CHA topology with equally-sized micropores in three-dimensions is assembled by layered stacking of the *cha* cages in the *c*-direction of the rhombic unit cell, forming double-6-membered ring units (*d6r*) between *cha* layers. The widest openings are the 8-Membered Rings (MR) in the hexagonal *cha* cage, which are accessible for molecules with kinetic diameters smaller than approximately 3.7 Å.[8] The structure of the medium pore zeolite with the MFI topology is much more complicated than the CHA topology. The SBUs of *mor*, *cas*, *mfi* and *mel* make up the three-dimensional MFI framework structure with orthorhombic symmetry having two zigzag channels (along [100] and [001]) and

one straight channel (along [010]) that are all intersecting. All channels have 10 MR openings with the maximum diffusional diameter of 4.7 Å. Diffusion along the [001] direction is achieved by movement between these zigzag and straight channels.[9]
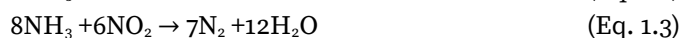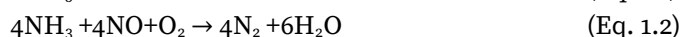
With the incorporation of an $[AlO_4]^-$ unit replacing a $[SiO_4]$ unit, the zeolite framework gets a local negative charge. Therefore, cations are needed to balance the charged zeolite framework. When a proton is the charge-balancing cation, the zeolite can act as a solid acid because of its ability to provide free H^+, also known as a Brønsted acid site. The nature of the strong acidity of proton-exchanged zeolites makes them commercially significant catalysts, for example, zeolite Y has been applied as a catalytic isomerization and cracking catalyst since around 1960.[2,7] Another successful industrial implementation of a proton-exchanged zeolite is the application of zeolite ZSM-5 in the Methanol-to-Hydrocarbons (MTH) process, where the Brønsted acid sites stabilize the surface methoxy species for C-C coupling.[10] The catalytic application of zeolites is broadened owing to their ability to ion-exchange. The charge-balanced sites in the zeolites can host various types of metal cations. In the case of zeolites ion-exchanged with transition metals, a redox center of Cu^{2+} or $Fe^{2+/3+}$ could be integrated, and these have been used for the partial oxidation of methane and Ammonia Selective Catalytic Reduction (NH_3-SCR) reaction.[11,12] Alternatively, the zeolites can also function as a support for highly dispersed metal nanoparticles, and simultaneously provide a Brønsted acidic function. In this scenario, the metal supported zeolites act as bifunctional catalysts in that both supported metal and Brønsted acid contribute to the reaction. For instance, in the hydroisomerization of alkanes over Pt/zeolites, hydrogenation takes place on Pt nanoparticles while isomerization occurs on Brønsted acid sites.[13]

1.2   Cu-exchanged Zeolites for Ammonia Selective Catalytic Reduction of NO_x

1.2.1   Ammonia Selective Catalytic Reduction of NO_x
NO_x (NO, NO_2) emissions are strictly regulated worldwide due to their adverse impacts on the environment and human health. It is inevitable to generate NO_x from diesel combustion at high temperatures such as in an internal combustion engine. Besides the Lean NO_x Trap (LNT) technique, the other widely applied efficient treatment of automotive NO_x emissions is the SCR reaction using NH_3 as an external reducing agent. Three reactions are most relevant for NH_3-SCR, namely: fast SCR reaction (Eq. 1.1), standard SCR reaction (Eq. 1.2) and slow

SCR reaction (Eq. 1.3), while the ratios between these reactions depend on the real-time gas compositions generated in the engine.[14] The reduction rate of the equimolar NO/NO_2 (fast SCR), NO (standard SCR) and NO_2 (slow SCR) by NH_3 under lean-burn condition follows the order of $r_{NO/NO2} \gg r_{NO} > r_{NO2}$.[15] The standard SCR reaction is the most prevalent reaction under real-world operational conditions because the automotive exhaust NO_x contains more than 90% NO.[16] The addition of NO_2 into the NH_3-standard SCR reaction system accelerates the reaction rate by following the fast SCR reaction. If the amount of NO_2 exceeds NO, the slow SCR reaction is also likely to take place.

$$4NH_3 + 2NO + 2NO_2 \rightarrow 4N_2 + 6H_2O \qquad \text{(Eq. 1.1)}$$
$$4NH_3 + 4NO + O_2 \rightarrow 4N_2 + 6H_2O \qquad \text{(Eq. 1.2)}$$
$$8NH_3 + 6NO_2 \rightarrow 7N_2 + 12H_2O \qquad \text{(Eq. 1.3)}$$

The abatement of NO_x is accomplished by one of the catalytic converters in the automotive emission control system, which is placed after the engine. Typically, the commercial automotive emission control system consists of a precious metal-based Diesel Oxidation Catalyst (DOC) to oxidize the CO or hydrocarbons from incomplete combustion, a Diesel Particulate Filter (DPF) wherein fine particles are trapped and a NH_3-SCR reaction unit including an Ammonia Slip Catalyst (ASC) (Figure 1.2).[17,18] NH_3 comes from the hydrolysis of urea, which is supplied by an external source. Therefore, the NH_3-SCR unit is rather complex because besides the NH_3-SCR reaction module using Cu-exchanged zeolites as catalysts, a urea injection system and a number of gas sensors are needed to regulate the appropriate amount of NH_3 for the constantly changing NO_x concentrations.[12,19] Finally, the ASC is employed to prevent the emission of excess NH_3 through the selective oxidation of NH_3 to N_2.
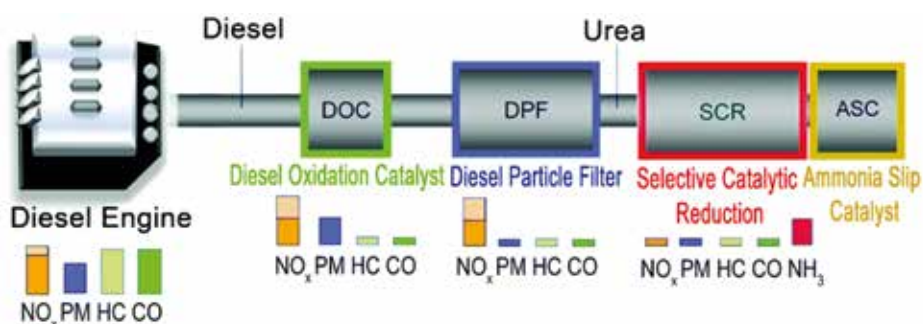

Figure 1.2 Schematic of key components in an automotive emission control system.[18] Copyright 2018 Royal Society of Chemistry.

The operational temperatures of NH_3-SCR are over a wide range, from low temperature (~150 °C) during vehicle cold start to high temperatures (occasionally up to 650 °C) at heavy loads. High temperatures may also occur when the NH_3-SCR unit is placed downstream of a DPF module which periodically regenerates.[20,21] Generally, the operational temperature of the diesel engine is in range of 150-500 °C. In practice, the vanadium-based oxide catalyst that is commercially used in stationary NO_x reduction is not suitable for diesel engine NO_x reduction systems, mainly due to its low efficiency at low operational temperatures and its high activity to unwanted SO_2 oxidation, that eventually leads to corrosion.[22] Furthermore, combustion gasses always contain water vapor which creates a hydrothermal environment for an operational NH_3-SCR unit. Therefore, suitable catalysts implemented in an automotive exhaust system need to be hydrothermally stable and active over a wide temperature range. In 1977, the Cu-containing zeolite Y was noted to be particularly active for low-temperature SCR, motivating the exploration of Cu-exchanged zeolites such as Cu-ZSM-5 and Cu-Beta for the NH_3-SCR reaction.[14] The most recent and promising approach was disclosed in a US patent over a decade ago. In this case, a Cu-exchanged zeolite with the CHA topology showed high performance and stability for the removal of NO. But the hydrothermal stability and the low-temperature NH_3-SCR activity needed to be further improved to match the long-life cycle of a vehicle.

1.2.2   Cu²⁺ as Active Species in Cu-exchanged Zeolites

According to a general understanding of the zeolite structure, the cations balance the negatively charged Si-O⁻-Al units in a zeolite framework, and can be replaced by ion-exchange with different cations. From the ion-exchange procedure, Cu^{2+} can be hosted in the zeolites in the form of bare Cu^{2+} or $[CuOH]^+$, which is in the proximity of paired Al or isolated Al, respectively. Therefore, the distribution of Al pairs determines the location of bare Cu^{2+}, which is greatly affected by Si/Al ratio and Cu loading in the zeolites. Figure 1.3 shows the possible positions of bare Cu^{2+} in CHA and MFI zeolites, showing that the paired Al only appears in the small rings.[18,23] It has been reported that with a lower ion-exchange level, the less reducible bare Cu^{2+} primarily locates in the 6MR, while the $[CuOH]^+$ favors the 8MR with an increasing Cu loading in zeolite CHA.[24,25] This is supported by the Rietveld refinement of the synchrotron-based XRD diffractogram of the dehydrated Cu-SSZ-13 (Si/Al=15.5, Cu/Al=0.45).[26] The dehydration of Cu-SSZ-13 (Si/Al=12, Cu/Al=0.44) under O_2 increases the population of tri-coordinated $[CuOH]^+$ sitting in the 8MR.[25] In Cu-ZSM-5, there are more possible sites to anchor bare Cu^{2+} and $[CuOH]^+$ due to the more complex structure. Bare Cu^{2+} could be found in

the 5MR or 6MR as indicated in a combined Electron Paramagnetic Resonance (EPR) and Density Functional Theory (DFT) simulation study.[27] It suggested the presence of square-pyramidal Cu^{2+} in the 5MR; and in the 6MR, three-fold, five-fold and square planar Cu^{2+} are possible coordination structures.
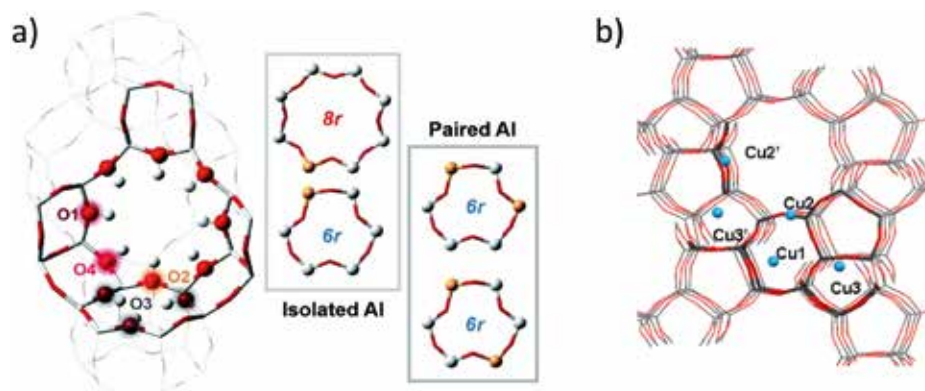
Figure 1.3 Possible location of Cu^{2+} and/or $[CuOH]^+$ in zeolites with a) CHA and b) MFI framework topology.[18,23] Copyright a) 2018 Royal Society of Chemistry and b) 2013 American Chemical Society.

It is noted that the speciation and location of Cu^{2+} can be changed in zeolites by alternating process conditions. The singly charged $[CuOH]^+$ commonly exists in Cu-exchanged zeolites especially with dominant isolated Al when Si/Al ratio is high. This is confirmed by the OH stretching (~3660 cm^{-1}) and the perturbed framework T-O-T vibration in Diffuse Reflectance Infrared Fourier-Transform Spectroscopy (DRIFTS).[28,29] The redox-active $[CuOH]^+$ can experience auto-reduction of Cu^{2+} during dehydration under vacuum or in inert gas flow, which was observed in a variety of Cu-exchanged zeolites, such as MFI, MOR, BEA, CHA and FAU.[30] It is proposed that two $[CuOH]^+$ ions are involved, resulting in a Cu^+ pair or isolated Cu^+ with the loss of oxygen and H_2O according to Eq. 1.4 and 1.5.[31] The auto-reduction has recently been observed even in an oxidative atmosphere above 400 °C in Cu-SSZ-13. The reduction of Cu^{2+} to Cu^+ was accompanied by the migration of Cu species from an 8MR to 6MR, suggested by an in-situ time-resolved Powder X-Ray Diffraction (PXRD) experiment and a combined PXRD/X-ray Absorption Near-Edge Structure (XANES) experiment.[32,33]

$2\ [CuOH]^+ = [Cu-O-Cu]^{2+} + H_2O = [Cu-\square-Cu]^{2+} + 0.5\ O_2 + H_2O$ (Eq. 1.4)

$2\ [CuOH]^+ = Cu^+ + Cu^{2+}O^- + H_2O$ (Eq. 1.5)

13
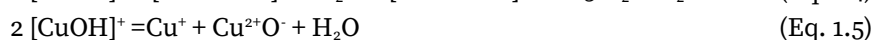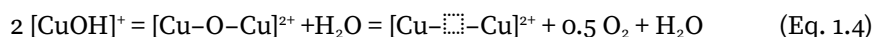
In an oxidative environment, a Cu dimer with bridged oxygen ($[Cu_2O]^{2+}$) was observed in N_2O or O_2 activated Cu-ZSM-5, giving a typical $O^{2-} \rightarrow Cu^{2+}$ charge transfer band in the UV-Visible (UV-Vis) Diffuse Reflectance Spectrum (DRS) located at ~22,700 cm^{-1}.[34,35] A subsequent study revealed the detailed structure of the possible Cu-dimers in Cu-ZSM-5 with resonance Raman (rR) spectroscopy.[36] An additional charge transfer band at ~29,000 cm^{-1} was observed in a Cu-ZSM-5 with a higher Cu loading. It was defined as a side-on bridged μ-(η^2-η^2) peroxo dicopper core, $[Cu_2(O_2)]^{2+}$, characterized by $^{18}O_2$ isotope sensitive and insensitive vibrations in rR spectroscopy. Similarly, Cu dimers with subtle structural differences can also be formed in the 8MR in Cu-SSZ-13 after O_2 activation, and their structures have been experimentally determined and optimized by ab initio simulations.[37]

1.2.3 Reaction Mechanisms and Deactivation

The reaction mechanism of the standard NH_3-SCR reaction is rather complicated over Cu-exchanged zeolites, not only because of the diversity of N-containing intermediates, but also the variation of Cu species and their corresponding reaction dynamics depending on reaction conditions. Micro-kinetic modeling of the NH_3-SCR reaction reinforces its complexity by the number of elementary steps observed.[38–40] Although reaction mechanisms have been globally proposed, normally with extensive reaction networks there are still debates on the structure of the Cu active center, the rate-determining step, the elementary steps in the $Cu^+ \rightarrow Cu^{2+}$ oxidation half-cycle and the role of Brønsted sites. The favored reaction pathways could vary on different catalysts, but it is generally accepted that low- and high-temperature NH_3-SCR do not follow the same reaction pathways and a redox cycle is involved in NH_3-SCR regardless of temperature.

Cu-exchanged zeolite CHA (Cu-CHA) is a model system for the study of the NH_3-SCR reaction mechanism due to its less complex framework structure compared to Cu-exchanged zeolite MFI (Cu-MFI). The following description of NH_3-SCR mechanisms and deactivation has been mostly acquired from studies of Cu-CHA, but the similar chemical nature of Cu^+/Cu^{2+} isomers or dimers in Cu-exchanged zeolites makes the conclusion broadly valid for Cu-exchanged zeolites with different framework structures.

1.2.3.1 The Low- and High-Temperature Operational Windows

The structures of Cu sites in the Cu-exchanged zeolites are highly dependent on process conditions, such as the gaseous atmosphere and reaction temperature. Therefore, it is conceivable that the low- and high-temperature NH_3-SCR could

follow different reaction mechanisms, because of the preferential Cu speciation and location. There is no clear demarcation line to separate the low- and high-temperature reaction, but usually a reaction temperature lower than 300 °C is considered to be 'low-temperature NH_3-SCR'.

Figure 1.4 Phase diagrams for Cu speciation in the 6MR in Cu-CHA at 1Al site (left) and 2Al site (right) with varying temperature and partial pressure of O_2 in 300 ppm NH_3 and 2% H_2O.[41] The Gibbs formation energies ΔG_{form} of various Cu species at 473 K and 10 % H_2O are listed in the sidebar of each phase diagram. Copyright 2016 American Chemical Society.

Cu speciation has been studied computationally under NH_3-SCR reaction conditions with varying reaction temperatures and O_2 partial pressures.[41] It shows that Cu^+/Cu^{2+}, balanced by isolated or paired Al, saturates with NH_3 at 473 K, and the NH_3 starts to release with increasing temperature (Figure 1.4). With 5-10% O_2, the complete removal of NH_3 takes place at ~500 °C for both Cu species in 1Al site and 2Al site. The ammoniated Cu species is more stable at low temperature but framework-stabilized Cu^+ or Cu^{2+} is preferred at high temperature. The variation of coordinated ligands on Cu^+/Cu^{2+} at low and high reaction temperature is also experimentally shown by in-situ X-ray Absorption Spectroscopy (XAS).[42,43] The mobile NH_3-solvated Cu^+ and Cu^{2+} ions are the dominant species up to 200 °C , while above 250 °C , the coordinated NH_3 is replaced by framework oxygen. There is a discrepancy in the exact temperature of NH_3 detachment between simulated and experimental results, but both give the same trends of temperature-dependent replacement of ligands.

1.2.3.2 The Cu^{2+}/Cu^+ Redox Cycle

The involvement of a Cu^{2+}/Cu^+ redox cycle in the NH_3-SCR reaction has been confirmed because of the co-existence of Cu^+ and Cu^{2+} during reaction revealed by operando or in-situ XAS studies.[42] Two proposed reaction pathways are

shown in Figure 1.5, with an isolated Cu^{2+}, either bare Cu^{2+} or $[CuOH]^+$, as the active center.[41,44] The proposed redox cycles maintain mass balance and charge balance, and only stable molecules are considered as NH_3-SCR reactants and products. The reduction half-cycle is consistent in both proposed pathways. The Cu^{2+} monomer is reduced by NO and NH_3 together. The NO-assisted dissociation of NH_3 accounts for the Cu^{2+} reduction, because it is more energetically favorable than the NH_3 activation of Cu^{2+} without NO.[45,46] Reduction of Cu^{2+} by only NH_3 is easier on the redox active $[CuOH]^+$ sites than on Cu^{2+} as indicated by Figure 1.4, where $[Cu(NH_3)_2]^+$ is dominant below 300 °C. The strong adsorption of NH_3 on Cu^+ ions causes a high energy barrier for its re-oxidation to Cu^{2+}, which therefore has been considered as a rate-determining step in low-temperature NH_3-SCR.[47] The weaker bonding of NO on Cu^{2+} makes it difficult to carry out the reduction half-cycle without coordinative NH_3.[41] Both NH_3 and NO are indispensable for efficient proceeding of the reduction half-cycle.
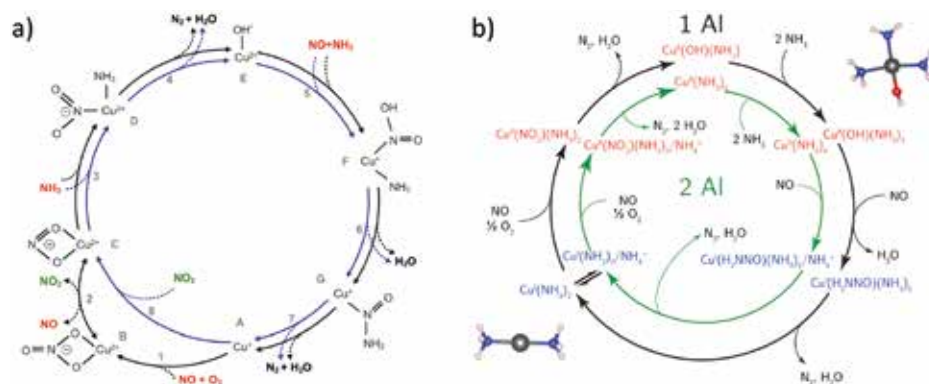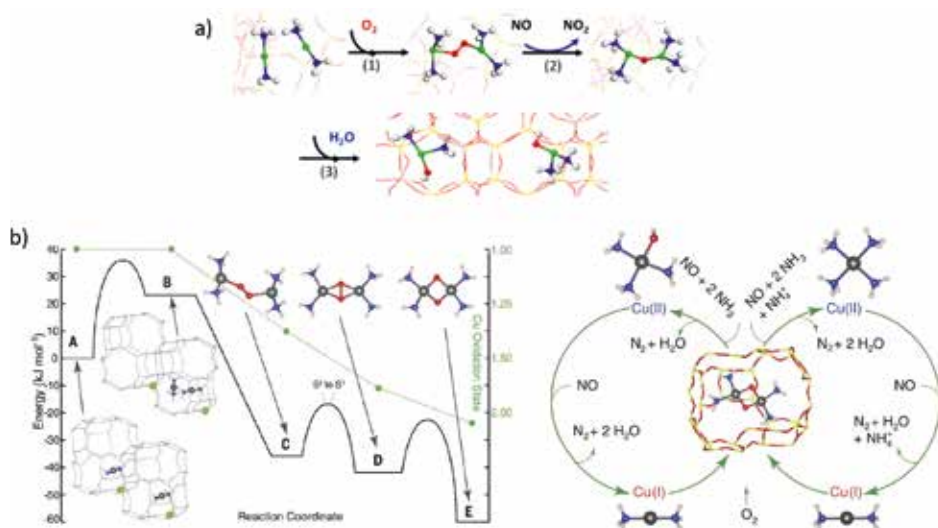

Figure 1.5 Two proposed low-temperature Selective Catalytic Reduction (SCR) reaction redox cycles involving only an isolated Cu^{2+} monomer.[41,44] Copyright a) 2015 American Chemical Society and b) 2016 American Chemical Society.

The oxidation half-cycle is proposed to be achieved by NO and O_2 that forms NO_2. It is stressed by Janssens et al. that the oxidation of a NO molecule by O_2 to a bidentate ligand is the rate-determining step suggested by the calculated high activation energy (Figure 1.5a).[44] A higher reaction temperature is beneficial to the formation of NO_2, experimentally supporting the NO_2-nitrate/nitrite routes.[48] Consequently, surface nitrates/nitrites are formed and nitrates are the most commonly observed surface species from Fourier-Transform Infrared (FT-IR) spectroscopy.[49–51] However, it is also proposed that the co-adsorption of NO_2 and NH_3 on the same Cu^{2+} site is possible, followed by the surface reaction and desorption of N_2 (Figure 1.5b).[41] Low reaction free energy was also found on the

NO_2-adsorbed Cu^{2+} site with a neighboring NH_3-adsorbed Brønsted acid site.[45] In this scenario, the Brønsted acid site is regarded as a key intermediate because it is formed accompanied by the reduction of bare Cu^{2+} and is subsequently consumed by the reaction with surface NO_2.

Figure 1.6 a) The proposed oxidation half-cycle and b) simulated energy of O_2 adsorption and oxidation of two $[Cu(NH_3)_2]^+$ ions (left) of the proposed redox cycle (right) in low-temperature Selective Catalytic Reduction (SCR) reaction redox cycles involving a Cu dimer.[53,54] Copyright a) 2017 American Chemical Society and b) 2017 American Association for the Advancement of Science.

The structure of the active center of NH_3-SCR can be re-considered based on a kinetic study over a series of Cu-SSZ-13 zeolites with varying amounts of isolated Cu^{2+}.[52] The NH_3-SCR reaction was performed under kinetic control and temperature-dependent kinetic behavior was indicated in the Cu-SSZ-13 with low Cu loading (<0.2 wt.%). A following study of NH_3-SCR on Cu-SSZ-13 (Si/Al=12, Cu/Al=0.13) clearly demonstrates an unusual catalytic behavior, where a 'dip' of NO conversion was found between 250-350 °C.[53] A linear rate versus square of Cu loading is shown in the low-temperature NH_3-SCR (<250 °C).[52,53] Therefore, it is inferred from the function of $(Cu/Al)^2$ and reaction rate that the completion of the Cu^{2+} redox cycle requires the involvement of a Cu dimer in low-temperature NH_3-SCR. A Cu dimer intermediate in the structure of $[Cu(NH_3)_2]^+$-O_2-$[Cu(NH_3)_2]^+$ was proposed, which is also suggested as the rate-determining step of the low-temperature NH_3-SCR over Cu-exchanged zeolites with low Cu loading.[53] The oxidation of Cu^+ to Cu^{2+} in this case also requires the participation of NO to form $[Cu(NH_3)_2]^{2+}$-O-$[Cu(NH_3)_2]^{2+}$, which is accompanied by the release of NO_2 (Figure

1.6a). In contrast, another simulation shows that the oxidation of Cu^+ can be achieved only by O_2, where two $[Cu(NH_3)_2]^+$ ions associate with a molecule of O_2 followed by the rearrangement and dissociation of O_2 across two Cu^+ centers (Figure 1.6b).[54] Eventually the $[Cu(NH_3)_2]^{2+}$-O_2-$[Cu(NH_3)_2]^{2+}$ is formed and is ready for the subsequent reaction with NO and NH_3. The formation of a Cu dimer $[Cu_2(NH_3)_4O_2]^{2+}$ with a side-on μ-η^2, η^2-peroxo diamino dicopper(II) structure in Cu-SSZ-13 (Si/Al=15, 2.6 wt% Cu) during low-temperature NH_3-SCR has also been identified by the detailed analysis of Extended X-ray Absorption Fine Structure (EXAFS) data.[55]

There is no agreement of the exact active center of the NH_3-SCR reaction in Cu-exchanged zeolites. Both a Cu monomer and a Cu dimer structure have been experimentally and computationally demonstrated.[41,44,53,54] The disagreement from different studies stems from the variation of the studied Cu-exchanged zeolites in that the zeolite framework topology, Si/Al ratio, Cu loading, Cu speciation and location can result in different conclusions. However, the consensus of the involvement of a Cu^{2+} redox cycle has been generally settled, i.e., the reduction of Cu^{2+} to Cu^+ with NH_3 and NO, which is then re-oxidized into Cu^{2+}, and both the reduction and oxidation half-cycles generate the desired product N_2.

1.2.3.3 The Mobility of Cu^+/Cu^{2+} complexes

The redox-driven migration of Cu^+/Cu^{2+} ions has been reported during the catalytic activation step as well as under the NH_3-SCR reaction conditions.[32] As mentioned above, Cu^{2+} preferentially locates in the 6MR in CHA, while the monovalent species $[CuOH]^+$ is more prevalent in the 8MR. After the O_2 activation process, the 8MR occupancy of $[CuOH]^+$ decreases, accompanied by an increasing population of Cu^{2+} in the 6MR, indicating the migration of Cu^{2+} from 8MR to 6MR during reduction. In the subsequent NH_3-SCR reaction, the local dynamics of Cu^+/Cu^{2+} ions are significantly enhanced, especially with the formation of highly mobile Cu^+ from the interaction of NO and NH_3 on Cu^{2+}, releasing the Cu center from the zeolite framework.[56] The higher mobility of Cu^+ is claimed for the weaker interaction and lower coordinative level with framework oxygen compared to Cu^{2+}.[57,58] The Cu^+/Cu^{2+} ion occupancy of the 6MR considerably exceeds the 8MR occupancy in Cu-SSZ-13 at a reaction temperature of 200 °C as revealed by the Rietveld refinement of PXRD data under reaction conditions, pointing to the correlation of NH_3-SCR activity and the population of Cu^+/Cu^{2+} ions in the 6MR.[33]
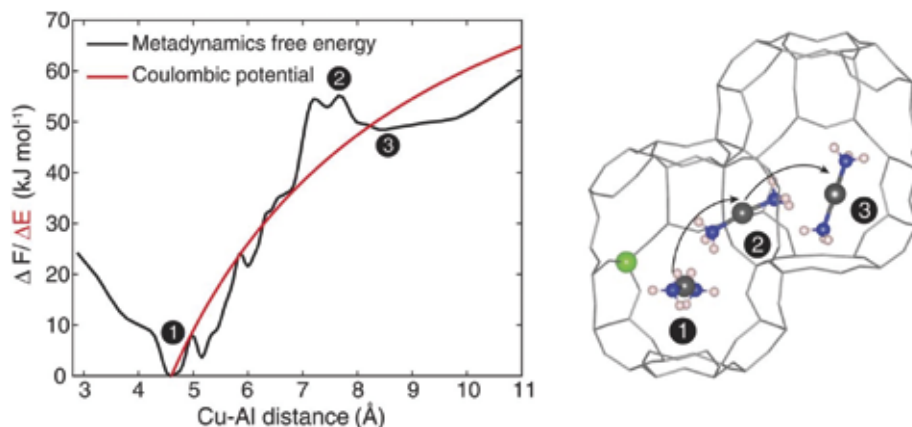
Figure 1.7 Free energy profile as a function of Cu-Al distance. The simulated $[Cu(NH_3)_2]^+$ diffusion from a *cha* cage with the charge-compensating Al (atom in green) to the adjacent *cha* cage without Al at 200 °C.[54] Labels are reactant state (1) $[Cu(NH_3)_2]^+$ at the same cage as Al, (2) $[Cu(NH_3)_2]^+$ diffusion through the 8MR and (3) $[Cu(NH_3)_2]^+$ arrival in the adjacent cage. Copyright 2017 American Association for the Advancement of Science.

Moreover, the ammoniated Cu^+/Cu^{2+} ions are mobile in the low-temperature NH_3-SCR reaction. The mobility of Cu^+/Cu^{2+} ions with a series of possible coordinating ligands (e.g., NH_3, NO, NO_2 NO_2^- and NO_3^-) under realistic operating conditions of the NH_3-SCR reaction was investigated by Ab Initio Molecular Dynamics (AIMD) simulations.[59] It is found that only NH_3 can solvate the Cu^+/Cu^{2+} and drive the migration of $[Cu(NH_3)_2]^+$ and $[Cu(NH_3)_4]^{2+}$ from the plane of the 6MR to the direction of the 8MR in Cu-SSZ-13. This was experimentally proven by the vibrational fingerprint of a perturbed framework vibration in the FT-IR spectrum. The above-mentioned hypothesis based on the formation of a Cu^{2+} dimer requires the migration of $[Cu(NH_3)_2]^+$, whose diffusion was pioneeringly simulated by Paolucci *et al.* (Figure 1.7).[54] The starting position of $[Cu(NH_3)_2]^+$ has the lowest free energy at a Cu-Al distance of 4.7 Å in a charge-balanced position. The Cu-Al distance reaches 8 Å as the $[Cu(NH_3)_2]^+$ moves across the 8MR towards the adjacent cages. The free energy then decreases once the $[Cu(NH_3)_2]^+$ enters the adjacent *cha* cage. The $[Cu(NH_3)_2]^+$ cannot diffuse further than 4.3 Å in this model, which is constrained by electrostatic tethering to the charge-balancing Al site close to the starting position. The mobility of NH_3-solvated Cu^+ ions increases the chance of the encounter of two $[Cu(NH_3)_2]^+$ complexes for the sequent formation of a transient Cu-dimer. This restrained mobility of $[Cu(NH_3)_2]^+$ does not entirely fit the conventional understanding of homogeneous and heterogeneous catalysts with mobile and immobile active sites, respectively. Instead, a quasi-homogeneous reaction environment presents in NH_3-SCR reaction considering the movement of Cu active centers.[53]

1.2.3.4 The Role of the Brønsted Acid Site

In Cu-exchanged zeolites, Brønsted acidity exists when it is not fully exchanged with Cu^{2+}. The study of the reaction mechanism over the Cu-exchanged zeolites has been based on the vanadium oxide-based catalyst for the NH_3-SCR reaction. It provokes an argument about the importance and functions of Brønsted acid sites since an acid cycle is proposed to be included in vanadia/titania, a conventional NH_3-SCR catalyst.[60] But in the Cu-exchanged zeolites, it is still under debate whether the Brønsted acid is a reaction intermediate.

It has been reported that zeolite Cu-SSZ-13 with the lowest Brønsted acidity had the highest NH_3-SCR activity in a series of Cu-SSZ-13 zeolites, indicating a necessary role of the Cu^{2+} redox cycle but not the Brønsted acid site.[61] But in the same study, it was pointed out that the reaction rate of NH_3-SCR appeared to increase with decreasing Si/Al ratio, suggesting the promotion effect of Brønsted acid sites. An apparent zero-order dependency on the Brønsted acid sites has been determined on Cu-SSZ-13, indicating that either the Brønsted acid site does not participate in NH_3-SCR or that the NH_4^+ is excessively provided.[62,63] Therefore, the benefit of a Brønsted acid site to the NH_3-SCR reaction rate can be assigned to increasing the exponential factor.

The function of the Brønsted acid site can be rationalized by the observed formation of an ammonium nitrate intermediate by FT-IR spectroscopy. The Brønsted acid site turns into NH_4^+ when NH_3 is adsorbed. If there is a proximal surface NO_2^- on Cu^{2+}, the formed NH_4NO_2 is unstable and decomposes to N_2 and H_2O.[49] Alternatively, the close coupling of NH_4^+ with a Cu site promotes the formation of Cu^{2+}-NO_2/NH_4^+ that also further decomposes to N_2 and H_2O.[45,56] Although NH_4NO_3 can also be formed in the oxidative atmosphere of NO/O_2, the conversion of nitrate to nitrite is possible through Eq. 1.6. The nitrite-nitrate equilibrium regulates the product selectivity if there is no side reaction because the decomposition of NH_3NO_4 produces N_2O at temperatures higher than 200 °C.

$$NO_3^- + NO \rightleftharpoons NO_2^- + NO_2 \qquad\qquad \text{Eq. 1.6}$$
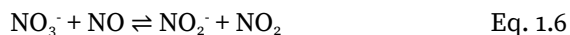
However, NH_4^+ has a slower consumption rate than the NH_3 adsorbed on Cu^+/Cu^{2+} according to the diminishing of their IR absorption bands, meanwhile, the time-resolved DRIFT spectra of $NO+O_2+ND_3/ND_3$ modulation experiment clearly indicates that NH_4^+ is more kinetically significant at non-steady state than at steady state at a low reaction temperature.[64] Therefore, the Brønsted acid sites might function as an NH_3 reservoir, increasing the local concentration

of NH_3.[49,61,64] Another recent in situ FT-IR study shows that the NH_3 adsorbed on a Brønsted acid site can migrate to the proximal Cu^{2+} site to participate the reduction half-cycle, proving that the Brønsted acid sites serve as an NH_3 reservoir.[65]

Higher Brønsted acid density can increase the NH_3-SCR reaction rate. It is difficult to determine whether NH_4^+ is a spectator or a reaction intermediate from an in situ/operando FT-IR study. Summarizing from the above-mentioned studies, the Brønsted sites facilitate the NH_3-SCR reaction, acting as an NH_3 reservoir that is not involved in the Cu^{2+} redox cycle; and the formation of NH_4NO_2/NH_4NO_3 during reaction cannot be excluded.

1.2.3.5 Catalyst Deactivation

In general, the deactivation of a zeolite catalyst can be attributed to the following causes: fouling, poisoning, thermal degradation (sintering), leaching of active sites, vapor-solid/solid-solid reaction and attrition.[66,67] Except for attrition, the mechanical loss of catalyst materials, the rest of the deactivation mechanisms are related to the blockage or loss of the accessible active sites. Fouling is commonly observed where the micropores in the zeolites are filled with inactive byproducts, hindering the diffusion of reactants/products. Solid-solid reactions occur when a zeolite loses its crystallinity, forming an amorphous phase.[68] Poisoning and thermal degradation occur on metal-containing zeolites. Metal can have very strong adsorption with impurities in real-world reaction process, occupying the adsorption sites for reactants and at the same time tuning the electronic properties of the surface. At a high reaction temperature, any structural change of the zeolite support or the metal nanoparticles brings about a weaker metal-support interaction and therefore sintering of dispersed active sites.

In the case of Cu-exchanged zeolites for the NH_3-SCR reaction, two main types of deactivation pathways are likely to happen under tailpipe conditions, i.e., sulfur poisoning and hydrothermal degradation. Sub-ppm SO_x levels from the engine exhaust originates from the combustion of ultra-low sulfur diesel fuel, which turns into SO_3/H_2SO_4 via SO_2 oxidation before reaching the NH_3-SCR unit in an automotive emission control system.[69] Surface sulfate, bisulfite and bisulfate can adsorb strongly on isolated Cu^{2+} sites, inhibiting the NH_3-SCR reaction by poisoning the active center.[70] Usually, sulfur poisoning has a more significant impact on the low-temperature NH_3-SCR reaction, because the Cu-exchanged zeolites can be regenerated by a periodic desulfation process at high

1

temperature under operational lean-burn conditions. The decomposition of ammonium sulfate needs a temperature of ~350 °C, while a higher temperature (>550 °C) is required for the removal of sulfate adsorbed on Cu^{2+}.[70,71]

In contrast to the reversible sulfur poisoning, continuous hydrothermal aging causes permanent destruction of Cu-exchanged zeolites. The NH_3-SCR catalysts are exposed to combustion product steam in the vehicle tailpipe. The zeolite framework can undergo hydrolysis at the Al-containing sites at high temperature, generating octahedral or tri-coordinated Al, that partially or completely detaches from the zeolite framework (dealumination).[72,73] Although it has been claimed that part of the framework Al could be restored by lowering the temperature, the severe ongoing steam treatment eventually causes irreversible destruction of the zeolite framework by the formation of amorphous $Al(OH)_3$.[74] The loss of framework Al also releases the charge balanced Cu^{2+} sites, resulting in the ultimate formation of Cu_xO_y or $CuAl_xO_y$ clusters/nanoparticles.[75] Another proposed hydrothermal degradation mechanism is that the aggregation of the Cu induced the loss of framework Al in the zeolites upon mild hydrothermal aging.[76] But, irrespective of the order, the interaction between Cu and framework Al is affected at hydrothermal conditions, eventually leading to the local degradation of zeolite framework and the formation of an NH_3-SCR inactive Cu phases. Undesired side reactions, for example the unselective NH_3 oxidation reaction, could then be promoted by the aggregation of Cu.

In practice, typical additives in the engine lubricating oil, such as phosphorous, calcium, magnesium and zinc, can also lead to catalyst deactivation in the NH_3-SCR unit.[77] The influence of inorganic additives on the NH_3-SCR reaction was extensively performed on zeolite Cu-SSZ-13.[78] It was found that compared to Zn and Ca, P causes a more severe suppression of NH_3-SCR activity since it induces pore blockage by polyphosphates, aggregation of Cu active sites and the destruction of the zeolite framework as well.

The deactivation of Cu-exchanged zeolites is a slow process. Cyclic exposure to a hydrothermal atmosphere is the most detrimental to the Cu-zeolites, causing the irreversible destruction of the zeolite framework structure and the sintering of Cu^{2+} active centers. Potential poisoning from a low concentration of impurities and incomplete combustion of byproducts deteriorates the catalytic activity, although it could be recovered. The hydrothermal stability is still one of the main concerns when choosing suitable catalysts for the NH_3-SCR unit as they should remain active over the vehicle lifetime.

1.3 Advanced Techniques for Nanoscale Characterization on Solid Catalysts
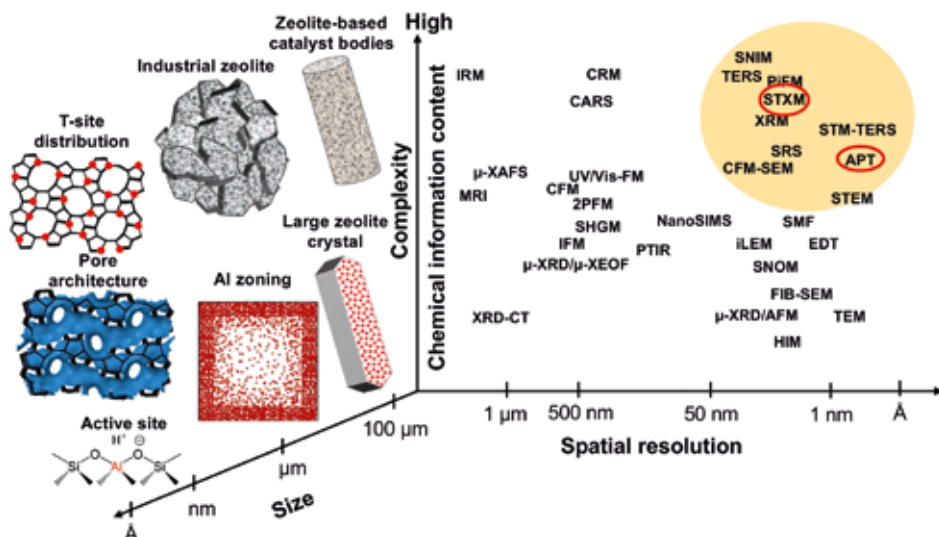
Figure 1.8 Highest reported spatial resolution of various characterization techniques with spatial resolutions at the micron scale and below, compared to the length scales of zeolite features of interest. The abbreviations are as follows: APT, Atom Probe Tomography; CARS, Coherent Anti-stokes Raman Scattering; CFM, Confocal Fluorescence Microscopy; CRM, Confocal Raman Microscopy; EDT, Electron Diffraction Tomography; FIB-SEM, Focused Ion Beam Scanning Electron Microscopy; CFM-SEM, Correlative Fluorescence Microscopy and Scanning Electron Microscopy; HIM, Helium Ion Microscopy; IFM, Interference Microscopy; iLEM, integrated Laser and Electron Microscope; IRM, Infrared Microscopy; MRI, Magnetic Resonance Imaging; NanoSIMS, Nano Secondary Ion Mass Spectrometry; PTIR, Photothermal Induced Resonance; SHGM, Second-Harmonic Generation Microscopy; SMF, Single Molecule Fluorescence; SNIM, Scanning Near-field Infrared Microscopy; SNOM, IR-scattering Scanning Near-field Optical Microscopy; SRS, Stimulated Raman Scattering microscopy; STEM, Scanning Transmission Electron Microscopy; STM-TERS, Scanning Tunneling Microscope-Tip Enhanced Raman Spectroscopy; STXM, Scanning Transmission X-ray Microscopy; TEM, Transmission Electron Microscopy; TERS, Tip Enhanced Raman Spectroscopy; 2PFM, two-Photon Fluorescence Microscopy; UV/Vis-FM, UV/Vis-Fluorescence Microscopy; XRD-CT, X-ray Diffraction-Computed Tomography; XRM, X-ray Microscopy; μ-XAFS, microbeam X-ray Absorption Fine Structure spectroscopy; μ-XRD/AFM, microbeam X-ray Diffraction/Atomic Force Microscopy; μ-XRD/μ-XEOF, synchrotron micro-X-ray Diffraction/micro-X-ray Excited Optical Fluorescence. Adapted from ref [79].

Investigating solid catalysts at various length scales provides a more comprehensive picture of their composition-structure-property relationships. The most common techniques usually belong to one of the categories of electronic spectroscopy (e.g., UV-vis), vibrational spectroscopy (e.g., IR and Raman) as well as methods assisted with X-ray radiation (e.g., XRD and XAS).[79]

These methods carry chemical information from the bulk or surface of catalysts, and generally provide average information of the examined samples.

However, in a real catalyst, a minority group of active sites might contribute the most to the activity or the deactivation. For example, in the methane partial oxidation reaction using Cu-exchange zeolites, CuO nanoparticles are commonly found in the Transmission Electron Microscopy (TEM) images, yet Cu clusters with low nuclearity are proposed to be responsible for methane activation.[80,81] Therefore, characterization techniques with high spatial resolution are required to obtain highly local chemical information. The pursuit of highly resolved spatial and temporal imaging meets the requisite of deep insight into the catalysts, with the ultimate purpose of understanding real catalysts at the atomic level. In Figure 1.8, an overview of characterization techniques along with their reported spatial resolutions and the estimated chemical information content is provided. There are only a few techniques capable of delivering sub 100 nm resolution while also delivering a high chemical information content as indicated in yellow circle in the figure. Particularly, in this PhD Thesis, Scanning Transmission X-ray Microscopy (STXM), with high chemical information content, and Atom Probe Tomography (APT), with sub-nanometer resolution, are studied due to their potential to obtain highly spatially resolved chemical information about both Cu and Al in Cu-exchanged zeolites to extend the understanding of their composition-structure-property relationships.
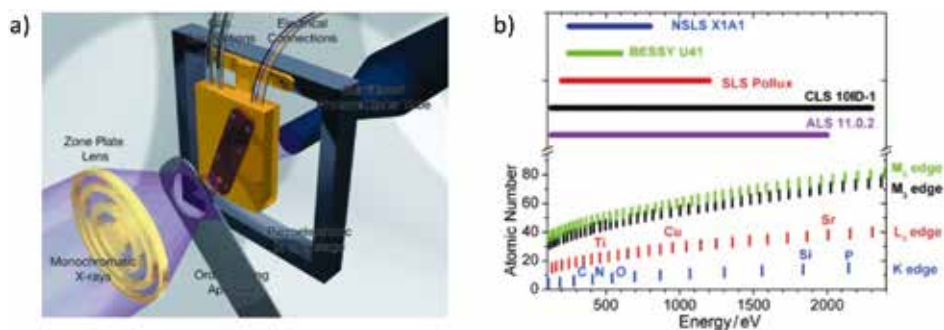
1.3.1 Scanning Transmission X-ray Microscopy

The general idea of soft X-ray STXM is to combine the advantages of XAS and microscopy, to attain chemical maps with detailed local information at nanometer scale spatial resolution. The basic components of a STXM microscope are illustrated in Figure 1.9a. The synchrotron-based mono-energetic X-ray is focused by a Fresnel zone plate, which determines the spot size and thus the spatial resolution.[82,83] The focused beam reaches the sample after blocking the unfocused zero order light by a so called Order Sorting Aperture (OSA). During the measurement, the sample plate is scanned pixel by pixel, while the transmitted photon flux is detected to make up a 2D image. This image is the Field of View (FOV) of the scanned area. Different energies across the absorption edge of a target element are measured, and as a result, a three-dimensional data set is obtained with the applied X-ray energy as the third dimension, yielding a full X-ray absorption spectrum in each pixel. But it is noted that, limited by the small sample volume of the specimen, the EXAFS is excluded because of

the insufficient signal-to-noise ratio, and XANES spectra are the source of local chemical information in the STXM measurements.

The utilization of soft X-rays decides the absorption edges that are allowed to be obtained. As shown in Figure 1.9b, the energy range of 200-2000 eV covers the K-edge (1s core) of light elements from C to P, $L_{2,3}$-edge (2p core) of metallic elements from K to Sr, as well as the $M_{4,5}$-edge (3d core) of rare-earth elements,[83] which includes most of the common elements contained in heterogeneous catalysts such as O, Al, Si, and P in the support and Mn, Fe, Co, and Ni in the active phase. The K-edge XANES describes the Density of States (DOS) of completely or partially unfilled electronic states by electron excitation with an X-ray photon from the 1s core to the final state, usually referring to the antibonding molecular orbital for ligand X-ray absorption and the p orbital for metal X-ray absorption.[84] The L-edge XANES is more complicated mainly because of the large overlap of p and d orbitals that causes a multiplet effect, and also because of the covalence with ligands (metal-ligand interaction) in the final state.[85,86] Therefore, for both K- and L-edge, the shape and position of the adsorption edge delivers abundant information including valance state and coordination environment (e.g., symmetry and coordination number) of the measured element.

Figure 1.9 a) Schematic of the Scanning Transmission X-ray Microscopy (STXM) experiment. b) The binding energies of K, L_3, M_3 and M_5 edges in the range of soft X-ray (bottom) and the X-ray energy range of STXM in NSLS X1A1, BESSY U41, SLS Pollux, CLS 10ID-1 and ALS 11.0.2.[83] Copyright 2010 Wiley-VCH.

The wide range of available elements for a STXM measurement ensures its broad applicability for solid catalyst characterization. Challenges in the application of STXM on heterogeneous catalysts come from the soft X-ray attenuation upon interacting with matter.[87] On one hand, sample thickness is usually in (sub)

micron range to avoid either too few counts remaining after transmission due to absorption or insufficient reduction of the incident beam intensity leading to a low signal. On the other hand, the path length of the X-ray should be minimized when designing the in-situ cell because substrates such as gas/liquid phases reduce transmitted X-ray intensity. A nanoreactor with a total path length of 50 μm designed for in-situ TEM was successfully adapted as an in-situ STXM nanoreactor in an experiment on an iron based Fischer–Tropsch Synthesis (FTS) catalyst under working conditions, with a spatial resolution of 35 nm.[88,89] Fe L-edge and O K-edge XANES were employed to track the transformation of the active phase, revealing the reduction of α-Fe_2O_3 and the formation of Fe_2SiO_4 during the pretreatment and reaction. While the C K-edge verified the existence of iron carbide in Fe-rich region as well as the FTS products in the area with less Fe. Moreover, the observation of carboxylic species in the Fe-deficient area implied the potential role of SiO_2 support in the spillover of (hydro)carbon species, which could only be observed in a specific area within the FOV. The beauty of STXM comes from the spatially resolved information that it provides a map of the local chemical environments (oxidation state and coordination) of measured elements. This allows heterogeneity, minor features, and the interplay between species to be discovered in an intuitive and straightforward way. For a study of $AlPO_4$ binder formation in zeolites, the types and locations of $AlPO_4$ islands were revealed by clearly chemical mapping of Al and P in an in-situ STXM measurement.[90] The crystalline $AlPO_4$ located on the external surface of zeolite mordenite grew from the amorphous $AlPO_4$, whilst in the zeolite interior, $AlPO_4$ phase was more amorphous. Another example is using STXM to study the C K-edge of the hydrocarbon product from the Methanol-to-Olefins (MTO) reaction. Here, bulkier hydrocarbon formation was visualized in the outer rim of the zeolite crystal through the feeble feature of a C 1s → C=C σ^* transition.[91] The above-mentioned examples demonstrate the power of STXM to study heterogeneous catalysis. The observed heterogeneity within catalysts particles provides additional local chemical information at nanometer scale of the catalyst, deepening the understanding of intrinsic structural features of catalysts.

1.3.2   Atom Probe Tomography

Further developments in nanoscience have led to advanced characterization techniques that achieve true nanometer resolution. APT is a 3-D microscopy that gives the location and speciation of atoms in the examined specimen, and further pushes the boundary of the resolution to the atomic level. APT was developed from Field-Ion Microscopy (FIM) which successfully imaged He^+ atoms for the

first time in October 1955 by Müller and Bahadur. By slowly applying a strong positive voltage on the needle-shaped tungsten tip to generate a sufficiently high electronic field of 30-50 V nm^{-1}, the imaging gas atoms such He and Ne are field ionized to He$^+$ or Ne$^+$ above the surface atom, and then accelerate to a phosphor screen with an Earth potential at cryogenic temperature under ultrahigh vacuum chamber back-filled with 1×10^{-5} mBar He.[92,93] A key development of this technology was the invention of Atom Probe Field Ion Microscopy (APFIM), a combination of FIM and a time-of-flight mass spectrometer, a decade after the field evaporation phenomenon was discovered.[94] When the electric field employed on the microtip is high enough at cryogenic temperatures, the surface atoms from the specimen evaporate as ions, and the flight time to the detector, which is determined by the mass-to-charge ratio, is recorded for the chemical identification.[95,96] Hence APFIM provides atomically resolved imaging with quantitative chemical analysis of elements and their isotopes. The prototype of APT dates back to the 1970s – the three-dimensional atom probe was invented by Panitz.[96,97] All ions of a given specimen could be detected and recorded in a two dimensional area and the third dimension was reconstructed from the order of evaporation.[98] At this point, the development of the atom probe technique was limited by the capability of detectors to simultaneously record the hit time and position of an individual ion in an evaporation event.

The modern APT instrument has been upgraded based on a position-sensitive atom probe, where a position-sensitive detector was adapted in the APFIM, mapping all detected atoms in two-dimensions.[99] The revolution of the performance improvement of APT was the incorporation of the local electrode close to the apex of the needle-shape specimen to reduce the required voltage for field evaporation,[100] as shown in Figure 1.10, illustrating the main components of the Local Electrode Atom Probe (LEAP), the most popular instrument for APT nowadays. The specimen is usually fabricated by Focused Ion Beam (FIB) milling, a common method for Scanning Electron Microscopy (SEM) sample preparation. For the APT measurement a laser pulse is applied to the needle-shaped specimen to generate momentary heating of the microtip, which could trigger field evaporation even for poorly conductive materials. The ionized atoms then travel through the local electrode in the electric field towards the position sensitive detector that records the flight event of individual atoms including the time-of-flight for chemical identification and the x-/y-coordinates.[96] The third dimension comes from the destructed volume on top of the microtip, which is projected on the detector and requires reconstruction based on order of evaporation to determine the position of individual atoms in the specimen.

1
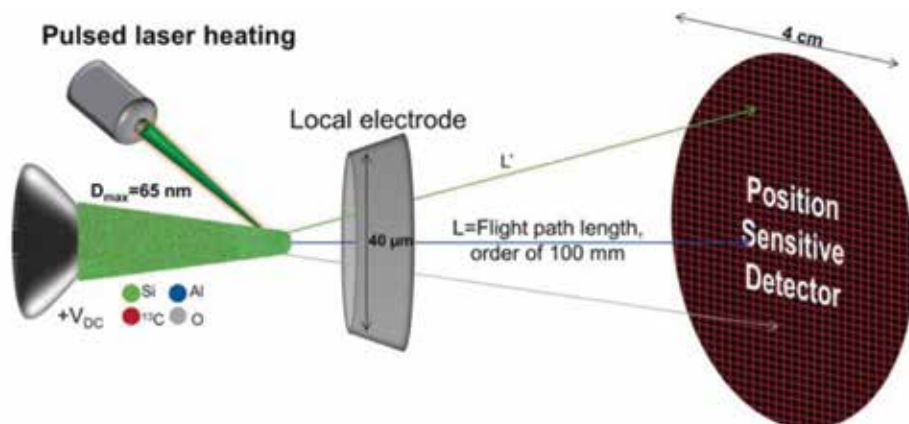
Figure 1.10 Schematic of the local electrode atom probe.[111] Copyright 2018 Wiley-VCH.

APT pushes the boundaries of spatial resolution to sub-nanometer length scales with chemical identity, thereby providing new insights with highly local elemental information. The early usage of APT was on metallic alloys, where the diffusional phase transformation, precipitation-nucleation in the solid-solid phase transformation, as well as phase separation and dislocation were extensively studied.[93,101] The application of APT has now been extended to a wide range of research topics due to the advance of laser heating allowing the technique to be applied to nonconductive materials, for example, to study the organic-inorganic interfaces in biominerals[102], isotopic fractionation and structure deformation in geological materials[103], dopant distribution and grain boundary diffusion in semiconductor devices,[104,105] and transition metal cation distribution in lithium-ion battery cathodes.[106] Although APT studies have been successfully carried out on real-world catalysts such as core-shell Au@Ag nanoparticles and supported catalysts Au/MgO, it is still challenging to prepare APT specimens of catalysts that are in submicron powder form, especially porous nanomaterials because the high mechanical stress in the specimen near the apex can easily cause specimen fracture during APT measurement.[93,107] Nevertheless, it is still feasible to prepare APT needles from robust zeolite crystals, allowing to analyze spatial distribution of individual atoms and can be used to detect nanoscale chemical heterogeneities. With the assistance of APT, a probable Al-Al neighboring distance was determined in a zeolite ZSM-5 single crystal, and the preferential location of Al clusters was unveiled in discrete patches or grain boundaries with relatively high Al density upon zeolite steaming.[108] Coke formation in the MTH reaction was spatially correlated with Brønsted acid sites from the affinity between coke and Brønsted acidic Al or Si in zeolite ZSM-5 or zeotype SAPO-34, respectively.[109,110] APT, the atomically resolved

microscopy, makes it possible to study the proximity of atoms and therefore the heterogeneity at the atomic scale, and local defects can now be discovered.

1.4   Scope and Outline of PhD Thesis

The work presented in this PhD Thesis is focused on the detailed characterization of Cu-exchanged zeolites with framework topologies CHA and MFI that are NH_3-SCR catalysts. Fresh catalysts have experienced simulated tailpipe aging by hydrothermal treatment (650-850 °C steaming). Fresh and aged Cu-changed zeolites were studied by advanced ex-situ and in-situ/operando spectroscopy and microscopy, including STXM, APT, UV-Vis DRS and DRIFTS, all aiming to reveal the steaming-induced local structural changes that account for the catalyst deactivation during real world application of the NH_3-SCR reaction.

In **Chapter 2**, STXM was employed on the fresh and aged zeolites Cu-CHA and Cu-MFI. The results provide detailed information of the local environment of the zeolite framework, formal oxidation state and geometric structure of Cu sites by Al K-edge and Cu L-edge XANES in two-dimensional maps with a 50×50 nm^2 resolution. The deactivation of Cu-exchanged zeolites is caused by multiple factors, including the degradation of zeolite framework and the degradation of the Cu phase. A spatial correlation between extra-framework Al and inactive Cu species was found near the surface of the individual zeolite particles. A weak, positive correlation between Cu^+ and tri-coordinated Al^{3+} is also presented.

In **Chapter 3**, a correlated APT-STXM study was performed on the zeolite Cu-SSZ-13 with a simulated 135,000-mile aging. APT, a single atom microscopic method, indicated local heterogeneity in the center of the zeolite crystal, which matches the spatially non-uniform portion of Al removal from the zeolite framework indicated by Al K-edge XANES from STXM measurement. The attempt to correlate the highly spatial resolved APT and STXM information for the characterization of the NH_3-SCR catalyst zeolite Cu-SSZ-13 was successful, revealing the heterogeneous degradation of the zeolite framework at length scales from micrometers to tens of nanometers.

In **Chapter 4**, a series of fresh and steamed Cu-ZSM-5 zeolites were applied for the NH_3-SCR reaction tests. An unusual catalytic behavior was observed in the steamed materials. It can be explained by the co-occurrence of an unselective NH_3 oxidation reaction, which is commonly attributed to the aggregation of Cu. Operando UV-Vis DRS and operando DRIFTS were employed to gain insights into the reaction and deactivation mechanism from the aspects of both Cu structure

1

and reaction intermediates. The high coordination number on Cu^{2+} during the NH_3-SCR reaction in fresh Cu-ZSM-5 contributed to its high NO conversion allowing a high surface coverage of nitrate intermediates. Pseudo-tetrahedral Cu^{2+} with coordinated NH_3 was prevalent in the low-temperature region, which might account for the NH_3 adsorption on the surface of $[Cu_x(OH)_{2x-1}]^+$ oligomers/clusters. The slow reaction between surface nitric acid and adsorbed NH_3 was ascribed for the low NH_3-SCR activity on the steamed Cu-ZSM-5. Practical suggestions are postulated from the revealed reaction mechanism and catalyst deactivation pathways.

Overall, in this PhD Thesis, the deactivation of Cu-exchanged zeolites with CHA and MFI structures was studied. The main findings and conclusions of each Chapter are summarized in **Chapter 5**, ending with challenges and future perspectives for NH_3-SCR catalyst development for lab-based research and industrial application.

REFERENCES

1   J. A. Dumesic, G. W. Huber and M. Boudart Eds., in *Handbook of Heterogeneous Catalysis*, Wiley-VCH, Weinheim, 2008, pp. 1–15.

2   U. Hanefeld and L. Lefferts Eds., *Catalysis: An Integrated Textbook for Students*, Wiley-VCH, Weinheim, 2018.

3   J. Hagen, *Industrial Catalysis*, Wiley-VCH, Weinheim, 2015.

4   P. Atkins, T. Overton, J. Rourker and M. Weller, *Shriver and Atkin's Inorganic Chemistry, Fifth Edition*, Oxford University Press, Oxford, 2010.

5   P. Atkins and J. de Paula, *Physical Chemistry, Ninth Edition*, Oxford University Press, Oxford, 2010.

6   C. S. Cundy and P. A. Cox, *Chem. Rev.*, 2003, **103**, 663–702.

7   E. M. Flanigen, *Stud. Surf. Sci. Catal.*, 2001, **137**, 11–35.

8   C. Baerlocher, Database of Zeolite Structures, can be found under http://www.iza-structure. org/databases/, 2017.

9   D. H. Olson, G. T. Kokotailo, S. L. Lawton and W. M. Meier, *J. Phys. Chem.*, 1981, **85**, 2238–2243.

10   I. Yarulina, A. D. Chowdhury, F. Meirer, B. M. Weckhuysen and J. Gascon, *Nat. Catal.*, 2018, **1**, 398–411.

11   M. Ravi, V. L. Sushkevich, A. J. Knorpp, M. A. Newton, D. Palagin, A. B. Pinar, M. Ranocchiari and J. A. van Bokhoven, *Nat. Catal.*, 2019, **2**, 485–494.

12   A. M. Beale, F. Gao, I. Lezcano-Gonzalez, C. H. F. Peden and J. Szanyi, *Chem. Soc. Rev.*, 2015, **44**, 7371–7405.

13   J. Zecevic, G. Vanbutsele, K. P. de Jong and J. A. Martens, *Nature*, 2015, **528**, 245–254.

14   C. Paolucci, J. R. Di Iorio, F. H. Ribeiro, R. Gounder and W. F. Schneider, *Adv. Catal.*, 2016, **59**, 1–107.

15   G. Tuenter, W. F. van Leeuwen and L. J. M. Snepvangers, *Ind. Eng. Chem. Prod. Res. Dev.*, 1986, **25**, 633–636.

16   M. Koebel, M. Elsener and G. Madia, *Ind. Eng. Chem. Res.*, 2001, **40**, 52–59.

17   F. Gao, J. H. Kwak, J. Szanyi and C. H. F. Peden, *Top. Catal.*, 2013, **56**, 1441–1459.

18   E. Borfecchia, P. Beato, S. Svelle, U. Olsbye, C. Lamberti and S. Bordiga, *Chem. Soc. Rev.*, 2018, **47**, 8097–8133.

19   S. Brandenberger, O. Kröcher, A. Tissler and R. Althoff, *Catal. Rev.*, 2008, **50**, 492–531.

20   F. Gao and J. Szanyi, *Appl. Catal. A Gen.*, 2018, **560**, 185–194.

21   W. Su, Z. Li, Y. Peng and J. Li, *Phys. Chem. Chem. Phys.*, 2015, **17**, 29142–29149.

22   L. Han, S. Cai, M. Gao, J. Y. Hasegawa, P. Wang, J. Zhang, L. Shi and D. Zhang, *Chem. Rev.*, 2019, **119**, 10916–10976.

23   U. Deka, I. Lezcano-Gonzalez, B. M. Weckhuysen and A. M. Beale, *ACS Catal.*, 2013, **3**, 413–427.

24   J. Hun Kwak, H. Zhu, J. H. Lee, C. H. F. Peden and J. Szanyi, *Chem. Commun.*, 2012, **48**, 4758.

25   E. Borfecchia, K. A. Lomachenko, F. Giordanino, H. Falsig, P. Beato, A. V. Soldatov, S. Bordiga and C. Lamberti, *Chem. Sci.*, 2015, **6**, 548–563.

26   C. W. Andersen, M. Bremholm, P. N. R. Vennestrøm, A. B. Blichfeld, L. F. Lundegaard and B. B. Iversen, *IUCrJ*, 2014, **1**, 382–386.

27   M. H. Groothaert, K. Pierloot, A. Delabie and R. A. Schoonheydt, *Phys. Chem. Chem. Phys.*, 2003, **5**, 2135–2144.

28   F. Giordanino, P. N. R. Vennestrøm, L. F. Lundegaard, F. N. Stappen, S. Mossin, P. Beato, S. Bordiga and C. Lamberti, *Dalt. Trans.*, 2013, **42**, 12741–12761.

29   J. H. Kwak, T. Varga, C. H. F. Peden, F. Gao, J. C. Hanson and J. Szanyi, *J. Catal.*, 2014, **314**, 83–93.

30   V. L. Sushkevich, A. V. Smirnov and J. A. van Bokhoven, *J. Phys. Chem. C*, 2019, **123**, 9926–9934.

31   V. L. Sushkevich and J. A. van Bokhoven, *Chem. Commun.*, 2018, **54**, 7447–7450.

32   C. W. Andersen, E. Borfecchia, M. Bremholm, M. R. V. Jørgensen, P. N. R. Vennestrøm, C. Lamberti, L. F. Lundegaard and B. B. Iversen, *Angew. Chem. Int. Ed.*, 2017, **56**, 10367–10372.

33   A. M. Beale, I. Lezcano-Gonzalez, W. A. Slawinksi and D. S. Wragg, *Chem. Commun.*, 2016, **52**, 6170–6173.

34   M. H. Groothaert, P. J. Smeets, B. F. Sels, P. A. Jacobs and R. A. Schoonheydt, *J. Am. Chem. Soc.*, 2005, **127**, 1394–1395.

35   M. H. Groothaert, K. Lievens, H. Leeman, B. M. Weckhuysen and R. A. Schoonheydt, *J. Catal.*, 2003, **220**, 500–512.

36   P. J. Smeets, R. G. Hadt, J. S. Woertink, P. Vanelderen, R. A. Schoonheydt, B. F. Sels and E. I. Solomon, *J. Am. Chem. Soc.*, 2010, **132**, 14736–14738.

37   D. T. Bregante, L. N. Wilcox, C. Liu, C. Paolucci, R. Gounder and D. W. Flaherty, *ACS Catal.*, 2021, **11**, 11873–11884.

38   H. Sjövall, R. J. Blint and L. Olsson, *Appl. Catal. B Environ.*, 2009, **92**, 138–153.

39   L. Olsson, K. Wijayanti, K. Leistner, A. Kumar, S. Y. Joshi, N. Kamasamudram, N. W. Currier and A. Yezerets, *Appl. Catal. B Environ.*, 2015, **174**–**175**, 212–224.

40   M. Bendrich, A. Scheuer, R. E. Hayes and M. Votsmeier, *Appl. Catal. B Environ.*, 2018, **222**, 76–87.

41   C. Paolucci, A. A. Parekh, I. Khurana, J. R. Di Iorio, H. Li, J. D. Albarracin Caballero, A. J. Shih, T. Anggara, W. N. Delgass, J. T. Miller, F. H. Ribeiro, R. Gounder and W. F. Schneider, *J. Am. Chem. Soc.*, 2016, **138**, 6028–6048.

42   K. A. Lomachenko, E. Borfecchia, C. Negri, G. Berlier, C. Lamberti, P. Beato, H. Falsig and S. Bordiga, *J. Am. Chem. Soc.*, 2016, **138**, 12025–12028.

43   E. Borfecchia, C. Negri, K. A. Lomachenko, C. Lamberti, T. V. W. Janssens and G. Berlier, *React. Chem. Eng.*, 2019, **4**, 1067–1080.

44   T. V. W. Janssens, H. Falsig, L. F. Lundegaard, P. N. R. Vennestrøm, S. B. Rasmussen, P. G. Moses, F. Giordanino, E. Borfecchia, K. A. Lomachenko, C. Lamberti, S. Bordiga, A. Godiksen, S. Mossin and P. Beato, *ACS Catal.*, 2015, **5**, 2832–2845.

45   C. Paolucci, A. A. Verma, S. A. Bates, V. F. Kispersky, J. T. Miller, R. Gounder, W. N. Delgass, F. H. Ribeiro and W. F. Schneider, *Angew. Chem. Int. Ed.*, 2014, **53**, 11828–11833.

46   Y. Mao, Z. Wang, H.-F. Wang and P. Hu, *ACS Catal.*, 2016, **6**, 7882–7891.

47   A. Marberger, A. W. Petrov, P. Steiger, M. Elsener, O. Kröcher, M. Nachtegaal and D. Ferri, *Nat. Catal.*, 2018, **1**, 221–227.

48   L. Ma, Y. Cheng, G. Cavataio, R. W. McCabe, L. Fu and J. Li, *Appl. Catal. B Environ.*, 2014, **156**–**157**, 428–437.

49   D. Wang, L. Zhang, K. Kamasamudram and W. S. Epling, *ACS Catal.*, 2013, **3**, 871–881.

50   C. Negri, P. S. Hammershøi, T. V. W. Janssens, P. Beato, G. Berlier and S. Bordiga, *Chem. Eur. J.*, 2018, **24**, 12044–12053.

51   M. Moreno-González, R. Millán, P. Concepción, T. Blasco and M. Boronat, *ACS Catal.*, 2019, **9**, 2725–2738.

52   F. Gao, E. D. Walter, M. Kollar, Y. Wang, J. Szanyi and C. H. F. Peden, *J. Catal.*, 2014, **319**, 1–14.

53   F. Gao, D. Mei, Y. Wang, J. Szanyi and C. H. F. Peden, *J. Am. Chem. Soc.*, 2017, **139**, 4935–4942.

1

54 C. Paolucci, I. Khurana, A. A. Parekh, S. Li,
    A. J. Shih, H. Li, J. R. Di Iorio, J. D. Albarracin-
    Caballero, A. Yezerets, J. T. Miller, W. N. Delgass,
    F. H. Ribeiro, W. F. Schneider and R. Gounder,
    Science, 2017, **357**, 898–903.

55 C. Negri, T. Selleri, E. Borfecchia, A. Martini,
    K. A. Lomachenko, T. V. W. Janssens, M. Cutini, S.
    Bordiga and G. Berlier, *J. Am. Chem. Soc.*, 2020,
    142, 15884–15896.

56 P. Chen, A. Khetan, M. Jabłońska, J. Simböck,
    M. Muhler, R. Palkovits, H. Pitsch and U. Simon,
    Appl. Catal. B Environ., 2018, **237**, 263–272.

57 A. Martini, E. Borfecchia, K. A. Lomachenko,
    I. A. Pankin, C. Negri, G. Berlier, P. Beato,
    H. Falsig, S. Bordiga and C. Lamberti,
    Chem. Sci., 2017, **8**, 6836–6851.

58 F. Göltl, P. Sautet and I. Hermans,
    Catal. Today, 2016, **267**, 41–46.

59 R. Millan, P. Cnudde, A. E. J. Hoffman,
    C. W. Lopes, P. Concepción, V. van Speybroeck
    and M. Boronat, *J. Phys. Chem. Lett.*, 2020, **11**,
    10060–10066.

60 N. Y. Topsoe, J. A. Dumesic and H. Topsoe,
    J. Catal., 1995, **151**, 241–252.

61 F. Gao, N. M. Washton, Y. Wang, M. Kollár,
    J. Szanyi and C. H. F. Peden,
    J. Catal., 2015, **331**, 25–38.

62 S. A. Bates, W. N. Delgass, F. H. Ribeiro,
    J. T. Miller and R. Gounder,
    J. Catal., 2014, **312**, 26–36.

63 S. A. Bates, A. A. Verma, C. Paolucci, A. A. Parekh,
    T. Anggara, A. Yezerets, W. F. Schneider, J. T.
    Miller, W. N. Delgass and F. H. Ribeiro, *J. Catal.*,
    2014, **312**, 87–97.

64 Y. Zhang, Y. Peng, K. Li, S. Liu, J. Chen, J. Li,
    F. Gao and C. H. F. Peden,
    ACS Catal., 2019, **9**, 6137–6145.

65 H. Kubota, T. Toyao, Z. Maeno, Y. Inomata,
    T. Murayama, N. Nakazawa, S. Inagaki, Y. Kubota
    and K. I. Shimizu, *ACS Catal.*, 2021, **11**, 11180–
    11192.

66 C. H. Bartholomew,
    Appl. Catal. A Gen., 2001, **212**, 17–60.

67 M. D. Argyle and C. H. Bartholomew,
    Catalysts, 2015, **5**, 145–269.

68 S. Bhatia, J. Beltramini and D. D. Do,
    Catal. Rev., 1989, **31**, 431–480.

69 J. Luo, D. Wang, A. Kumar, J. Li,
    K. Kamasamudram, N. Currier and A. Yezerets,
    Catal. Today, 2016, **267**, 3–9.

70 Y. Jangjou, Q. Do, Y. Gu, L.-G. Lim, H. Sun,
    D. Wang, A. Kumar, J. Li, L. C. Grabow and
    W. S. Epling, *ACS Catal.*, 2018, **8**, 1325–1337.

71 Y. Jangjou, D. Wang, A. Kumar, J. Li and
    W. S. Epling, *ACS Catal.*, 2016, **6**, 6612–6622.

72 J. A. van Bokhoven, A. M. J. van der Eerden and
    D. C. Koningsberger, *J. Am. Chem. Soc.*, 2003,
    125, 7435–7442.

73 B. H. Wouters, T. Chen and P. J. Grobet,
    J. Phys. Chem. B, 2001, **105**, 1135–1139.

74 M. C. Silaghi, C. Chizallet, J. Sauer and
    P. Raybaud, *J. Catal.*, 2016, **339**, 242–255.

75 P. N. R. Vennestrøm, T. V. W. Janssens, A. Kustov,
    M. Grill, A. Puig-Molina, L. F. Lundegaard,
    R. R. Tiruvalam, P. Concepción and A. Corma,
    J. Catal., 2014, **309**, 477–490.

76 J. Luo, F. Gao, K. Kamasamudram, N. Currier,
    C. H. F. Peden and A. Yezerets, *J. Catal.*, 2017,
    348, 291–299.

77 P. Kern, M. Klimczak, T. Heinzelmann, M. Lucas
    and P. Claus, *Appl. Catal. B Environ.*, 2010, **95**,
    48–56.

78 I. Lezcano-Gonzalez, U. Deka, H. E. van der Bij,
    P. Paalanen, B. Arstad, B. M. Weckhuysen and
    A. M. Beale, *Appl. Catal. B Environ.*, 2014, **154**–
    155, 339–349.

79 I. L. C. Buurmans and B. M. Weckhuysen,
    Nat. Chem., 2012, **4**, 873–886.

80 P. Tomkins, A. Mansouri, S. E. Bozbag,
    F. Krumeich, M. B. Park, E. M. C. Alayon,
    M. Ranocchiari and J. A. van Bokhoven,
    Angew. Chem. Int. Ed., 2016, **55**, 5467–5471.

81 H. V. Le, S. Parishan, A. Sagaltchik, C. Göbel,
    C. Schlesiger, W. Malzer, A. Trunschke,
    R. Schomäcker and A. Thomas,
    ACS Catal., 2017, **7**, 1403–1412.

82 W. Chao, B. D. Harteneck, J. A. Liddle,
    E. H. Anderson and D. T. Attwood,
    Nature, 2005, **435**, 1210–1213.

83 F. M. F. de Groot, E. de Smit,
    M. M. van Schooneveld, L. R. Aramburo and B. M.
    Weckhuysen,
    ChemPhysChem, 2010, **11**, 951–962.

84 J. G. Chen, *Surf. Sci. Rep.*, 1997, **30**, 1–152.

85 F. de Groot, *Chem. Rev.*, 2001, **101**, 1779–1808.

86 E. C. Wasinger, F. M. F. de Groot, B. Hedman, K. O.
    Hodgson and E. I. Solomon,
    J. Am. Chem. Soc., 2003, **125**, 12894–12906.

87 B. M. Weckhuysen, *Angew. Chem. Int. Ed.*, 2009,
    48, 4910–4943.

88 J. F. Creemer, S. Helveg, G. H. Hoveling,
    S. Ullmann, A. M. Molenbroek, P. M. Sarro and
    H. W. Zandbergen, *Ultramicroscopy*, 2008, **108**,
    993–998.

89 E. de Smit, I. Swart, J. F. Creemer, G. H. Hoveling, M. K. Gilles, T. Tyliszczak, P. J. Kooyman, H. W. Zandbergen, C. Morin, B. M. Weckhuysen and F. M. F. de Groot, *Nature*, 2008, **456**, 222–225.

90 H. E. van der Bij, D. Cicmil, J. Wang, F. Meirer, F. M. F. de Groot and B. M. Weckhuysen, *J. Am. Chem. Soc.*, 2014, **136**, 17774–17787.

91 L. R. Aramburo, E. de Smit, B. Arstad, M. M. van Schooneveld, L. Sommer, A. Juhin, T. Yokosawa, H. W. Zandbergen, U. Olsbye, F. M. F. de Groot and B. M. Weckhuysen, *Angew. Chem. Int. Ed.*, 2012, **51**, 3616–3619.

92 E. W. Müller and K. Bahadur, *Phys. Rev.*, 1956, **102**, 624–631.

93 T. F. Kelly and M. K. Miller, *Rev. Sci. Instrum.*, 2007, **78**, 031101.

94 E. W. Müller, J. A. Panitz and S. B. McLane, *Rev. Sci. Instrum.*, 1968, **39**, 83–86.

95 F. de Geuser, B. Gault, A. Bostel and F. Vurpillot, *Surf. Sci.*, 2007, **601**, 536–543.

96 D. N. Seidman, *Annu. Rev. Mater. Res.*, 2007, **37**, 127–158.

97 J. A. Panitz, *Rev. Sci. Instrum.*, 1973, **44**, 1034–1038.

98 T. F. Kelly and J. A. Panitz, *Micros. Today*, 2017, **25**, 12–17.

99 A. Cerezo, T. J. Godfrey and G. D. W. Smith, *Rev. Sci. Instrum.*, 1988, **59**, 862–866.

100 T. F. Kelly and D. J. Larson, *MRS Bull.*, 2012, **37**, 150–158.

101 A. Devaraj, D. E. Perea, J. Liu, L. M. Gordon, T. J. Prosa, P. Parikh, D. R. Diercks, S. Meher, R. P. Kolli, Y. S. Meng and S. Thevuthasan, *Int. Mater. Rev.*, 2018, **63**, 68–101.

102 S. M. Reddy, D. W. Saxey, W. D. A. Rickard, D. Fougerouse, S. D. Montalvo, R. Verberne and A. van Riessen, *Geostand. Geoanalytical Res.*, 2020, **44**, 5–50.

103 D. W. Saxey, D. E. Moser, S. Piazolo, S. M. Reddy and J. W. Valley, *Scr. Mater.*, 2018, **148**, 115–121.

104 A. D. Giddings, S. Koelling, Y. Shimizu, R. Estivill, K. Inoue, W. Vandervorst and W. K. Yeoh, *Scr. Mater.*, 2018, **148**, 82–90.

105 R. Agrawal, R. A. Bernal, D. Isheim and H. D. Espinosa, *J. Phys. Chem. C*, 2011, **115**, 17688–17694.

106 A. Devaraj, M. Gu, R. Colby, P. Yan, C. M. Wang, J. M. Zheng, J. Xiao, A. Genc, J. G. Zhang, I. Belharouak, D. Wang, K. Amine and S. Thevuthasan, *Nat. Commun.*, 2015, **6**, 8014.

107 C. Barroo, A. J. Akey and D. C. Bell, *Appl. Sci.*, 2019, **9**, 2721.

108 D. E. Perea, I. Arslan, J. Liu, Z. Ristanović, L. Kovarik, B. W. Arey, J. A. Lercher, S. R. Bare and B. M. Weckhuysen, *Nat. Commun.*, 2015, **6**, 7589.

109 J. E. Schmidt, J. D. Poplawsky, B. Mazumder, Ö. Attila, D. Fu, D. A. M. de Winter, F. Meirer, S. R. Bare and B. M. Weckhuysen, *Angew. Chem. Int. Ed.*, 2016, **55**, 11173–11177.

110 J. E. Schmidt, L. Peng, A. L. Paioni, H. L. Ehren, W. Guo, B. Mazumder, D. A. Matthijs de Winter, Ö. Attila, D. Fu, A. D. Chowdhury, K. Houben, M. Baldus, J. D. Poplawsky and B. M. Weckhuysen, *J. Am. Chem. Soc.*, 2018, **140**, 9154–9158.

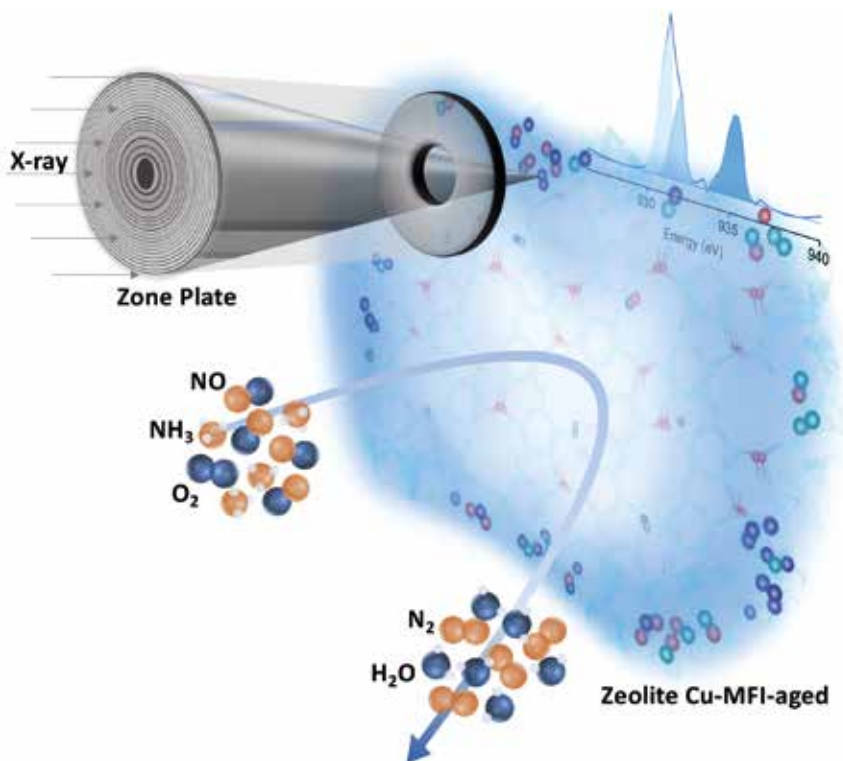111 J. E. Schmidt, L. Peng, J. D. Poplawsky and B. M. Weckhuysen, *Angew. Chem. Int. Ed.*, 2018, **57**, 10422–10435.

1

2

Deactivation of Cu-exchanged Automotive Emissions NH$_3$-Selective Catalytic Reduction Catalysts Elucidated with Nanoscale Resolution using Scanning Transmission X-ray Microscopy

ABSTRACT

To gain nanoscale insights into the underlying mechanisms of catalyst durability for the Selective Catalytic Reduction (SCR) of NO_x with ammonia as reductant, Scanning Transmission X-ray Microscopy (STXM) was employed to study Cu-exchanged zeolites with the CHA and MFI framework structures before and after a simulated 135,000-mile aging procedure. X-ray Absorption Near-Edge Structure (XANES) measurements were performed at the Al K- and Cu L-edges using a spot size of 50×50 nm². The local environment of framework Al, Cu oxidation state and geometric changes were analyzed, showing a multi-factor induced catalytic deactivation. In Cu-exchanged zeolite ZSM-5, a transformation of Cu^{2+} to Cu^+ and Cu_xO_y was observed as a result of the aging process. A spatial correlation between extra-framework Al and deactivated Cu species near the surface of the zeolite particle was also found. In addition, a weak, positive correlation between Cu^+ and tri-coordinated Al was present. By inspecting both Al and Cu species within fresh and aged Cu-exchanged zeolites, it is concluded that the importance of the preservation of isolated Cu^{2+} sites trumps that of Brønsted acid sites for NH_3-SCR activity.

2.1. Introduction

Increased fuel efficiency in diesel vehicles results in the undesirable production of environmentally unwanted nitrogen oxides (NO$_x$).[1,2] The commonly employed solution in mobile vehicles is ammonia Selective Catalytic Reduction (NH$_3$-SCR) of NO$_x$ over Cu-exchanged zeolite catalysts. This was first proposed in a landmark study in 1986 with Cu-exchanged zeolite ZSM-5 with the MFI framework structure, which showed high activity, but had insufficient lifetime under the harsh operational conditions of a real vehicle.[3] To meet the actual requirements of a mobile tailpipe, SCR catalysts must maintain activity throughout a vehicle's lifetime, while experiencing a wide range of temperatures between 150 and 550 °C in the presence of steam as well as hydrocarbons and other poisons (e.g., sulfur).[4,5] Another Cu-exchanged zeolite, SSZ-13 with the CHA framework, has recently been commercialized for diesel vehicle NH$_3$-SCR as it provides the required catalytic performance and lifetime. Although it was only first disclosed in the mid-2000s, this material has already been the subject of numerous studies aiming at further improving its catalytic performance and lifetime.[5]

To understand the reasons for the high catalytic activity and lifetime of Cu-exchanged zeolites in the NH$_3$-SCR reaction, mechanistic insights about the catalytic reaction are needed, which is why the behavior of both the Cu sites and the role of the Brønsted acid sites are topics of extensive investigations.[6] It is commonly agreed upon that the reaction pathway is conducted by the Cu^{2+}/Cu$^+$ redox cycle under standard NH$_3$-SCR conditions, where the oxidation of Cu$^+$ is considered as the rate-determining step.[7–9] As for Brønsted acid sites, it is proposed that they act as an NH$_3$ reservoir for Cu sites, but are not involved in forming reactive species.[10] Most of our understanding of Cu speciation and location, and acid properties that might affect the NH$_3$-SCR reaction, originates from X-Ray Diffraction (XRD),[11] X-ray Absorption Spectroscopy (XAS),[8,11–13] ^{27}Al Magic Angle Spinning solid-state Nuclear Magnetic Resonance (MAS ssNMR) spectroscopy,[12] Fourier-Transform Infrared (FT-IR spectroscopy),[13] UV-Vis Diffuse Reflectance Spectroscopy (DRS)[14] and Electron Paramagnetic Resonance (EPR)[15]. These studies of Al and/or Cu properties have led to a more complete picture of sites contributing to NO$_x$ reduction, which gives insight into the catalytic mechanism to guide rational catalyst design. However, to further extend the boundaries of our understanding of NH$_3$-SCR deactivation, spatially resolved chemical studies at resolutions below 100 nm, that is, significantly smaller than the size of most single catalyst particles, are required, which allow studying the behavior and correlation between species within one catalyst particle in an intuitive way.

So far, only a few techniques could deliver the necessary sub-100 nm spatial resolution and high chemical information content.[16] An Atom Probe Tomography (APT) study of Cu-exchanged zeolites probed the Al and Cu clustering after aging with single atom sensitivity.[17] For the sake of a comprehensive study of local chemical information, Scanning Transmission X-ray Microscopy (STXM) in combination with X-ray Absorption Near-Edge Structure (XANES) spectroscopy routinely allows chemical imaging at sub-100 nm spatial resolution, making it a powerful technique to study heterogeneous catalysts in a spatially resolved manner.[18] From a STXM measurement a stack of images is obtained that can be regarded as a three-dimensional data volume. The x axis and y axis make up the Field of View (FOV) of the scanned area, while the z axis represents the scanned energy. Therefore, each scanned pixel contains an X-ray absorption spectrum, that is here, more specifically, one XANES spectrum. The power of X-ray chemical imaging lies in the abundant chemical information of detailed local environments revealed in a specific FOV, which enables exploitation of the local relationship between different species.

To reinforce previous studies on Cu-exchanged zeolites as automotive emissions catalysts from our group,[17,19] in this Chapter, we report the use of STXM to study the local chemical environment and distribution of Al and Cu in two distinct NH_3-SCR catalysts, namely zeolites Cu-SSZ-13 and Cu-ZSM-5. Both fresh and aged (135,000-mile simulation[20]) versions of each catalyst material with similar Si/Al ratios and Cu loadings were studied. By comparing the chemical properties of fresh and aged counterparts, the dramatic decrease of NH_3-SCR performance in the most deactivated Cu-exchanged zeolite particles could be attributed to the distortion and aggregation of isolated Cu^{2+} expedited by the formation of extra-framework Al species, as revealed by the heterogeneity in the recorded Al and Cu distribution maps. This finding is complemented with conventional characterization methods, including XRD, FT-IR spectroscopy with NO as probe molecule and ammonia Temperature-Programmed Desorption (NH_3-TPD). The evolution of both Al and Cu species in Cu-exchanged zeolites caused by the aging procedure is discussed and the general properties of the deactivated NH_3-SCR catalysts are pictured in detail. Due to the spatially resolved nature of the STXM data, it was feasible to explore the chemical properties of Al and Cu in different regions within the examined catalyst particle and make statements on the differences between the performances of fresh and aged zeolites Cu-SSZ-13 and Cu-ZSM-5.

2.2.   **Experimental Section**

2.2.1   **Catalyst Preparation**

Zeolite SSZ-13 was prepared by combining 25.3 g of 25 wt% solution of a N,N,N-trimethyl-1-adamantammonium (Sachem) with 10 g of a 1 M NaOH solution and 10 g of zeolite Y (Zeolyst, CBV720), and then water was added to bring the total mass to 70 g. The mixture was homogenized using magnetic stirring, and then divided into several 23 mL Parr autoclaves reactors, placed in an oven at 160 °C and allowed to react for 4 days while rotating. The product was recovered using centrifugation and washed with copious amounts of water and dried in an oven at 80°C. Prior to reaction testing samples were calcined in air by initially holding them at 150 °C for 3 h before heating the samples further to 580 °C for 6 h to remove the organic structure directing compound. After calcination they were exchanged to ammonium form using 1 M NH$_4$NO$_3$ (100 mL of solution per gram of catalyst) at 80 °C with stirring for 3 h; this was done a total of three times. NH$_4^+$-SSZ-13 and NH$_4^+$-ZSM-5 (Zeolyst, CBV2314) were then calcined to its proton form using the standard method in air at 550 °C before ion-exchanged with Cu^{2+}. 1 g zeolite in proton form was suspended in 250 mL 10 mM Cu(II) acetate solution and stirred at room temperature for 24 h, followed by washing with a large excess of demineralized water. After drying, the catalyst was then calcined again in air using the same calcination program. The calcined Cu-SSZ-13 and Cu-ZSM-5 materials are labelled as Cu-CHA-fresh and Cu-MFI-fresh, respectively.

The 10 % steam in air flow was produced by using a bubbler at 47 °C and was first introduced to the fresh zeolite Cu-CHA or Cu-MFI in a porcelain boat-shaped crucible placed in a tube furnace at 120 °C to prevent condensation. The steaming procedure was conducted at 800 °C using a ramping rate of 2°C/min and held for 16 h. The steamed Cu-exchanged zeolites were then cooled down to room temperature in dry air and are labelled as Cu-CHA-aged and Cu-MFI-aged.

2.2.2   **Catalyst Characterization**

X-ray Diffraction (XRD) patterns of Cu-exchanged zeolites were collected by a Bruker D2 Phaser with a cobalt radiation X-ray source (Co k$_\alpha$ = 1.789 Å). Powdered samples were pressed on the sample holder and rotated at 15 revolutions/min during the measurement.

Inductively Coupled Plasma-Optical Emission Spectroscopy (ICP-OES) was measured using a SPECTRO CIROSCCD (SPECTRO Analytical Instruments) at the GeoLab of Utrecht University. Cu-exchanged zeolites were dissolved at

90 °C overnight by aqua regia with HF solution. After cooling down to room temperature, the solution was neutralized by boric acid followed by dilution to an appropriate concentration.

The morphologies of Cu-exchanged zeolites CHA and MFI were studied on a Philips XL30 Scanning Electron Microscope (SEM) at an accelerating voltage of 5 kV or 10 kV.

Temperature-Programmed Desorption of Ammonia (NH_3-TPD) was taken on a Micromeritics Autochem II 2920 instrument equipped with a Thermal Conductivity Detector (TCD). The Cu-exchanged zeolite sample was first degassed in He flow for 1 h at 600 °C with a heating ramp of 10 °C/min. Ammonia then flowed pass the sample at 100 °C, followed by flushing with He at 100 °C for 2 h. The ammonia desorption was tracked using TCD at a ramping rate of 5°C min^{-1} in a 25 mL min^{-1} He flow.

NO-adsorbed Fourier-Transform Infrared (FT-IR) spectra in transmission mode were measured on a Perkin-Elmer 2000 instrument. 20 mg sample was grounded and pressed into a slice to fit the self-supported wafer, which was then placed in a holder with CaF_2 window for the FT-IR spectroscopy measurements. The sample was dehydrated at 200 °C for 1 h in vacuum of 1.2×10^{-6} mBar, the cell was then cooled down to room temperature. The NO dosing was operated at -188 °C achieved by liquid nitrogen. FT-IR spectra were recorded upon NO adsorption at elevated cell pressure from 1×10^{-1} to 15 mBar by dosing 1 % NO/Ar.

2.2.3   Catalytic Testing

The NH_3-SCR activity testing was performed in a plug flow fixed bed reactor as described in a previous study of our group.[17] 50 mg of sieved catalyst (0.425-0.150 mm) was loaded into a 1 cm quartz tubular reactor and firstly calcined with 5 % O_2 in He flow at 550 °C, followed by treating with SCR gas feed (provided by Linde) of 1000 ppm NO, 1000 ppm NH_3 and 5 % O_2 balanced by He under a Gas Hourly Space Velocity (GHSV) of 100,000 h^{-1}. The conversion of NO was calculated when the reaction reached the steady-state and took the average conversion in the stabilization period of 60 min from 150 to 450 °C. The concentration of output gases was analyzed by a gas phase FT-IR spectrometer (Spectrum Two, PerkinElmer) with a non-heated gas cell with KBr windows and a beam path length of 5 cm. NO conversion was calculated as follows:

$$\text{NO conversion (\%)} = \frac{[NO_{in}] - [NO_{out}]}{[NO_{in}]} \times 100\ \%. \qquad \text{(Eq. 2.1)}$$

2.2.4 Data Collection and Analysis by Scanning Transmission X-ray Microscopy
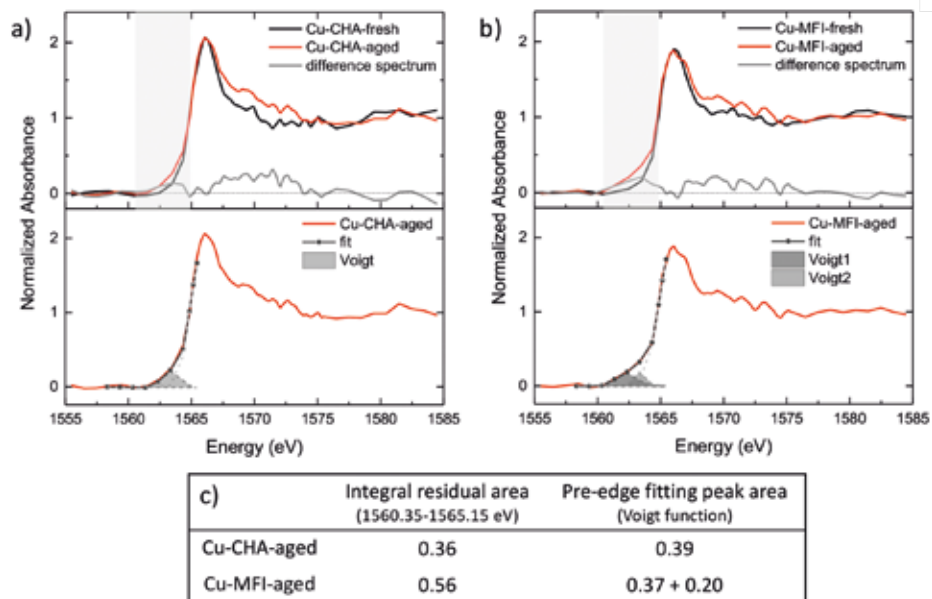
2.2.4.1 Data Collection

Scanning Transmission X-ray Microscopy (STXM) measurements were performed at the Advanced Light Source (ALS) beamline 11.0.2, Lawrence Berkeley National Laboratory (LBNL), Berkeley, California, USA. Zeolite samples were dispersed in deionized water followed by drop casting them on a silicon nitride window, which was then mounted perpendicular to the X-ray beam on a piezo motor stage. The chamber was first evacuated, followed by back filling with He to around 0.27 bar to minimize X-ray absorption by air and reduce the drift of the motor stage caused by heat generated during the measurement. The X-ray beam was focused by a 45 nm Fresnel Zone Plate (ZP) and sequentially an Order Sorting Aperture (OSA) with a 90 μm pinhole to a spot size of 50×50 nm^2. A stack of transmission images at various energy points across the Al K- and Cu L-edges were collected by raster scanning the sample with a step size of 50 nm.

2.2.4.2 Al K-edge and Cu L-edge X-ray Absorption Near-Edge Structure

STXM data was processed in aXis2000, TXM-Wizard, Athena and Matlab. TXM-Wizard provides various functions for synchrotron-based X-ray microscopy, which are used to get spatially resolved chemical information by performing Principal Component Analysis (PCA) and Cluster Analysis (CA). The aligned images representing Optical Density (OD) were obtained from processing in aXis2000 and then imported to TXM-Wizard, followed by cropping them where necessary to remove empty pixels. A pixel size of 25×25 nm^2 was generated from the original pixel size of 50×50 nm^2 by oversampling using a factor of 2 using bicubic interpolation to a have spatial exploration of fine differences within catalyst particles. Then the background was determined and filtered based on the X-ray absorption spectrum of each pixel, leaving only the particle of interest in the Field of View (FOV) for further analysis.

Background pixels and pixels with extremely noisy X-ray Absorption Near-Edge Structure (XANES) spectrum (i.e., pixels with XANES that could not normalized) were first filtered and the XANES of the remaining pixels were normalized before performing PCA and k-means CA. PCA and CA were used to group single pixel XANES based on their spectral similarity. An edge jump filter was employed to remove the noisy pixels based on the difference between pre-edge and post-edge, followed by using a normalization filter to remove pixels with a distorted pre-edge or post-edge. After applying an edge jump filter and normalization

filter, the XANES spectrum of the whole image was obtained by summing up XANES spectrum of every pixel. Thus, the bulk XANES represents the overall chemical information of Al or Cu of the catalyst.

c)	Integral residual area (1560.35-1565.15 eV)	Pre-edge fitting peak area (Voigt function)
Cu-CHA-aged	0.36	0.39
Cu-MFI-aged	0.56	0.37 + 0.20

Figure 2.1 Estimation of the pre-edge area of Al K-edge XANES in a) Cu-CHA-aged and b) Cu-MFI-aged. The upper panels in a) and b) show the difference spectrum between the fresh Cu-exchanged zeolite and its aged counterpart. The residual area from 1560.35 to 1565.15 eV was integrated. The lower panels in a) and b) show the fitting of the pre-edge area by a Pseudo-Voigt function. The edge was fitted by error function represented by the light grey dash line. The integral area calculated by the above manners is shown in c).

The Al K-edge XANES was analyzed in Athena. The spectrum was first normalized before any other further analysis. The Least-Square Linear Combination (LSLC) fitting was used to quantify the amount of octahedral Al with the fitting range of 1560.35~1574.35 eV, where zeolite ZSM-5 and α-Al$_2$O$_3$ were chosen as the references which were measured previously by our group.[21] Because the edges of tetrahedral Al and tri-coordinated Al overlap, so the percentage of tetrahedral Al obtained from LSLC fitting was contributed from both of these Al species. The estimation of the pre-edge feature assigned to tri-coordinated Al was conducted in two ways. The difference spectrum between the aged Cu-exchanged zeolite and its fresh counterpart was used to calculate the area of the pre-edge feature. The area from 1560.35 to 1565.15 eV was integrated. Another way is fitting the shape of edge by an error function followed by fitting

the pre-edge region by a pseudo-Voigt function. These two methods gave the same results (Figure 2.1).

Cu L-edge XANES were extracted from the stack of absorption images in TXM-Wizard and the background was subtracted in Origin 9.0 followed by normalizing the maximum absorption to 1 in order to compare the differences between spectra. Since both the L$_2$- and L$_3$-edge of the L-edge XANES provide the same information, the L$_3$-edge exhibiting stronger absorbance was chosen to investigate the Cu species. The peak position of Cu L$_3$-edge was determined by fitting the peak maximum with a Gaussian-Lorentz peak. Cu L-edge XANES presents the intrinsic property of the ground-state configuration of the Cu atom, which determines the possibility and accessibility of an electronic transition from Cu 2p to higher unoccupied band. The L-edge absorption of Cu^{2+} with an unoccupied 3d orbital showing a strong absorption at 931~932 eV (L$_3$-edge), dominates in spectrum followed by a weaker absorption with ~20 eV energy gap (L$_2$-edge), referring to the 2p→3d transition. For Cu$^+$ with fully filled d orbitals, the L$_3$-edge absorption could be explained by the transition from 2p^{6}3d^{10} to 2p^{5}3d^{10}4s^1 transition[22] and hybridization of 3d-4s orbitals, resulting in a higher L-edge peak energy position for Cu$^+$ compared to Cu^{2+}.[23] Therefore, the L-edge peak area is related to the hole density in a destination orbital in a Cu atom, implying that the ratio of the integrated peak area reflects the relative amount of the different species. To estimate Cu L-edge peak area, reference spectra of CuO and Cu$_2$O were normalized to an edge jump of 1.0 at 1000 eV,[24,25] yielding Area(Cu^{2+})/Area(Cu$^+$) a factor of 1/1.9, which was then applied to samples.

2.2.4.3 Principal Component Analysis and *k*-means Cluster Analysis

In order to classify all pixels into different groups according to their spectral features, PCA and CA were performed after applying the edge jump filter and normalization filter. The pixels remaining after filtering (each containing a XANES with 80 energy points across the Al K-edge XANES) gave enough signal to obtain clear spectral features, including edge position and edge jump. Based on the eigenspectra and scree plot, the 80 dimensions (for the Al stack) in each pixel were reduced to two or three dimensions that ensured that 90% of data's variance was captured. The selected two or three PCs were then used to plot the data in two/three-dimensional principal component space (score plot) in which *k*-means CA was performed using a user-defined number clusters decided upon inspection of the score plot. Based on the initial result from *k*-means CA, the clusters were then optimized by an Expectation Maximization (EM) algorithm for Gaussian Mixture Modeling (GMM) considering point density. This

resulted in a class-membership value for each pixel based on its XANES; this value represents the degree (weight) to which each pixel belongs to a certain cluster. After CA, the XANES spectra of the different clusters were obtained as the weighted average of the XANES of all points of each cluster and the analysis of cluster XANES spectrum was the same as done for bulk XANES spectrum. PCA and CA of the Cu stack was performed in a similar way as for the Al stack. Because the Al scan and Cu scan were obtained separately, the FOVs of both scans of the same sample were different.

2.2.4.4 Detailed Analysis of Spatial Information of a Cu-MFI-aged Zeolite

Due to low absorption at the Al K-edge in each pixel that was only 25 nm after oversampling, it was more promising to start analysis from a Cu scan with a much higher absorption in the Cu L-edge range. All the following processing procedure was conducted in Matlab.

Pixels with square planar Cu^{2+} were first selected from the analyzed area. Based on the PCA and CA performed on the Cu map of zeolite Cu-MFI-aged, Cu L-edge XANES of one of the Cu clusters showed two peaks with an energy gap of ~1 eV. This is a sign of the existence of Cu^{2+} with both tetrahedral and square planar geometric structures. The slope between 931.4 and 931.9 eV around the position of the shoulder in the Cu L_3-edge region was defined to distinguish pixels with a shoulder as indicated in Figure 2.2a. By calculating the defined slop of Cu L_3-edge peak in each individual pixel, a map of slop was obtained as shown in Figure 2.2b. Ranges of the slope were set to group pixels with similarly defined slope. In this way, pixels with asymmetrical peak were grouped into four clusters labeled as Surface 1-4, exhibiting different fractions of square planar Cu^{2+} indicated by the Cu L-edge XANES.

The extremely degraded region of Cu-MFI-aged was excluded when studying the evolution of Al and Cu species within an individual zeolite particle. The most important feature from the Cu L-edge XANES is the area ratio of the Cu^+ and Cu^{2+} L_3-edge. Considering the high noise level of single pixel XANES, it is difficult to examine the peak area of Cu^+ and Cu^{2+} correctly. Therefore, PCA was applied to inspect the distribution of Cu properties. As seen from the eigenspectra of the first two Principal Components (PC) in Figure 2.2c, PC1 resembles the average spectrum of the analyzed pixels and the contribution of PC2 reflects the amount of Cu^{2+}. The positive value in the eigenimage of PC2 (Figure 2.2b) indicates pixels with a higher amount of Cu^{2+} compared to the average spectrum, while negative value indicates pixels with a lower amount of Cu^{2+}, i.e., higher Cu^+. Contribution

of PC2 in every pixel varies from around 0.05 to -0.05. By evenly splitting the contribution of PC2 into five regions, five clusters (Center 1-5 in Figure 2.11) with different levels of Cu^{2+} contribution were determined. Then, both Cu L-edge XANES and Al K-edge XANES of the clusters Center 1-5 were obtained, which is shown in Figure 2.11.
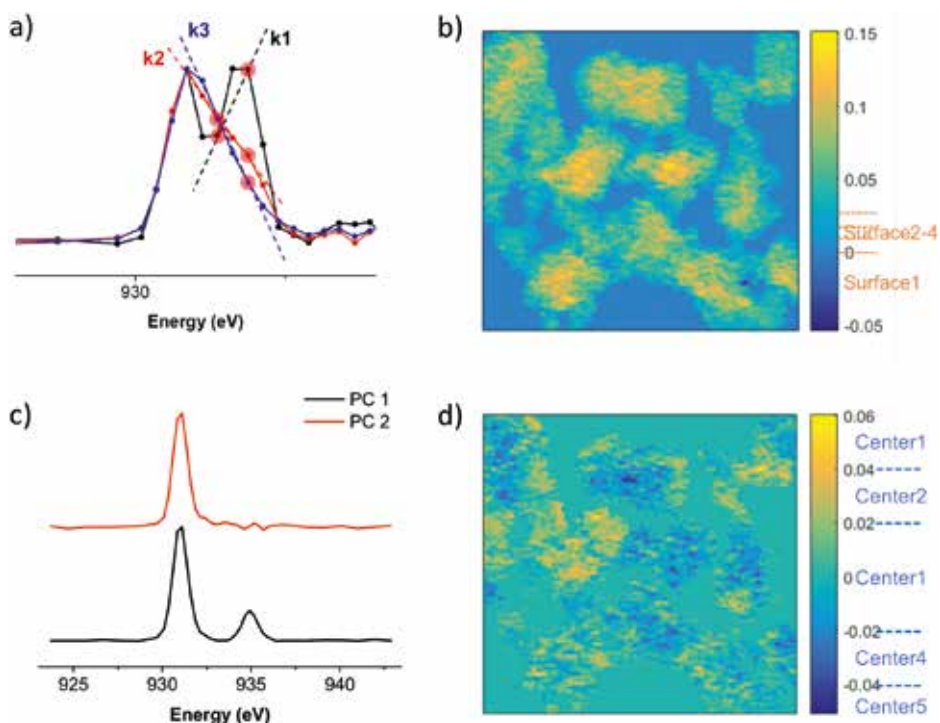
Figure 2.2 a) The slope between the energy of 931.4 eV and 931.9 eV was determined to discriminate Cu L$_3$-edge spectrum with more than one Cu^{2+} species. b) The map of slope in zeolite Cu-MFI-aged obtained by calculating the defined slop from Cu L$_3$-edge peak of each individual pixel, and the thresholds setting for clusters Surface 1-4. c) Eigenspectra of the first two principal components by employing Principal Component Analysis (PCA) on the Cu STXM-XANES (Scanning Transmission X-ray Microscopy-X-ray Absorption Near-Edge Structure) data after filtering the surface pixels. d) Eigenimage of the second Principal Component (PC2) and the thresholds setting for clusters Center 1-5.

2.2.4.5 Multiplet Calculations in a Crystal Field of Nearest Neighbors

The edge position reflects the geometric structure of Cu^{2+}. The crystal field splitting of the 3d orbital changes the energy level of the d orbital, resulting in different energy gaps between the 4s and 3d orbitals and thus changes the peak positions in the Cu L-edge XANES. In order to learn how the coordinate structure influences the Cu L$_{2,3}$-edge absorption spectra, we employ a multiplet

computation program MultiX which constructs the crystal field via the positions and charges of surrounding atoms instead of via the symmetrized matrix elements.[26] The atomic wave function was used in solving the multiplet energy levels, where the multiplet levels were calculated by determining the electron-electron, spin-orbit interactions, and the effect of the crystal-field. In the current model, the crystal environment is approximated to be the superpostion of point charges potential of the nearest neighbors, that is the crystal environment was determined only by the postion of the nearest neighbors. All the calculated spectra were normalized to the L_3 feature (~930 eV).

2.3.   Results and Discussion

2.3.1   Structure-Performance Relationships

This study was motivated by the NH_3-SCR catalytic performance tested on fresh and aged Cu-exchanged zeolites CHA and MFI. As shown in Figure 2.3, for both fresh Cu-exchanged zeolites CHA and MFI, a NO conversion of 80-100 % was achieved in the temperature regime of 200-450 °C, though a slow but steady decrease was observed for Cu-MFI-fresh starting at a temperature of 250 °C and above. Surprisingly, although the aged Cu-CHA underwent a steaming process (simulated aging) before starting the reaction, it exhibited high activity and stability for NO conversion, evidenced by the fact that almost 100 % NO conversion was maintained up to a temperature of 350 °C. In contrast, NO conversion was dramatically reduced for Cu-MFI after the aging process, with the highest observed NO conversion being 60 % at the highest temperature (450 °C). These results are consistent with those reported in numerous studies.[12,27,28]
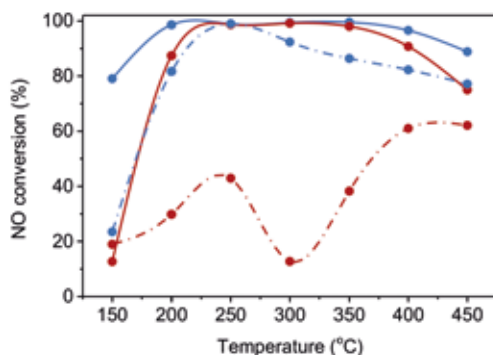
Figure 2.3 NO conversion of fresh (blue) and aged (red) Cu-exchanged zeolites CHA (solid) and MFI (dash) in NH_3-Selective Catalytic Reduction (SCR) reaction.

By comparing two aged zeolites Cu-CHA-aged and Cu-MFI-aged, a significant difference in NH$_3$-SCR activity was observed. One of the most straightforward explanations for this enormous gap in catalytic activity is the differences in stability of the framework structures. However, as indicated by the XRD patterns recorded for our samples, both Cu-CHA and Cu-MFI zeolite samples retained their framework structures after the aging process (Figure 2.4a-b). On the other hand, it is known that Brønsted acidity originating from framework Al can be hydrolyzed or dehydroxylated upon interacting with steam.[29] Therefore, even though the long-range order of the zeolite structure might be preserved upon steaming, the local structure of framework Al can change that one of the consequences was the loss of Brønsted acidity represented by the high temperature band at around 550 °C in the NH$_3$-TPD profiles (Figure 2.4c-d). Subsequently, the nature of Cu ions, that relies on the position and density of framework Al, might be affected. With the degradation of framework Al, a positive charge from the Cu cation is no longer necessary and futher leads to the migration and aggregation of Cu.

2
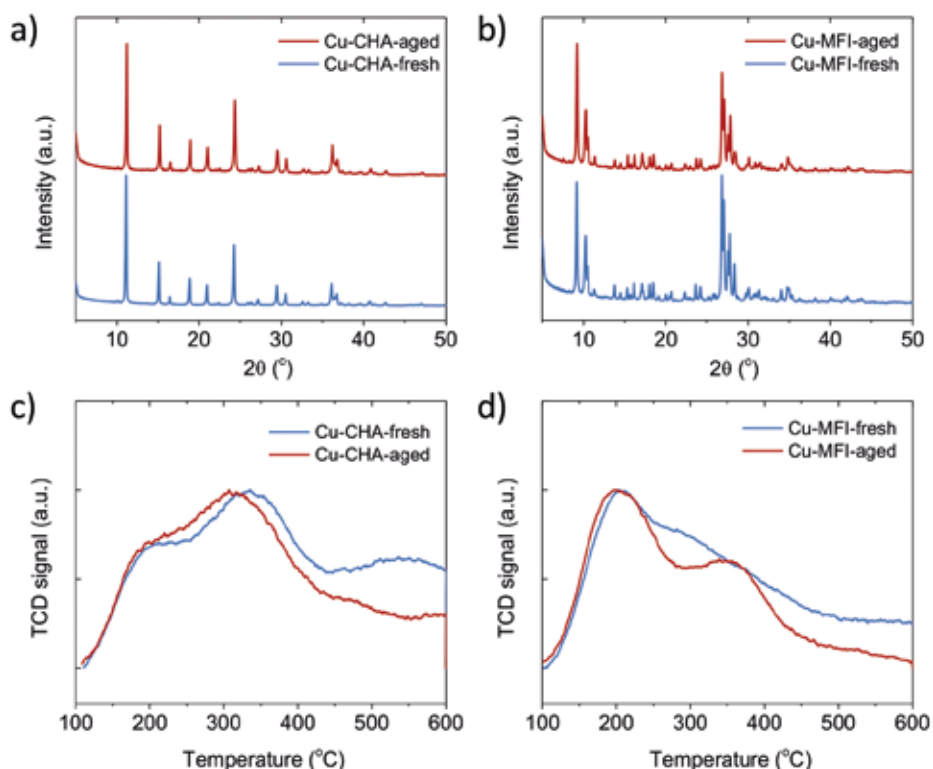
Figure 2.4 X-Ray Diffraction (XRD) patterns of fresh and age Cu-exchanged zeolites a) CHA and b) MFI. And ammonia Temperature-Programmed Desorption (NH$_3$-TPD) profiles of fresh and aged Cu-exchanged zeolites c) CHA and d) MFI.

Changes in the local environment of framework Al were evidenced in bulk Al K-edge XANES. It is a relatively straightforward and convincing way to distinguish and quantify Al coordination as compared to high resolution ^{27}Al MAS ssNMR, a commonly used technique that is, however, sensitive to a diminished signal or line broadening especially when paramagnetic species like Cu^{2+} (d^9) are present.[30,31] The 'bulk single particle XANES' we discuss is the XANES spectrum obtained by averaging all XANES spectra recorded for all pixels of a catalyst particle; details can be found in the experimental section. The aging procedure caused a similar effect on Al coordination in both zeolites Cu-CHA and Cu-MFI according to Figure 2.5a. Although tetrahedral Al, determined by the nature of tetrahedral T sites in the zeolite, was still the dominant species, the emergence of octahedral Al becomes measurable via the occurrence of a shoulder located at the edge position of tetrahedral Al and the peak that becomes visible in the 1569-1575 eV region for both aged zeolites. Furthermore, a pre-edge feature was observed for the aged zeolites, which was more pronounced in the aged Cu-MFI zeolite. This notable low energy feature in the energy range of 1561-1565 eV was assigned to tri-coordinated Al identified by full multiple scattering calculations in a previous study.[31]

A reversible tetrahedral-octahedral transformation of framework Al could be achieved by hydration and dehydration treatment, where either octahedral Al or Al-OH forms by partial hydrolysis with host water molecules.[32,33] In this way, Al is saturated with H_2O and without loss of lattice Al. In contrast, intensive steaming undoubtedly accelerates the hydrolysis of the framework Al-O bond, especially at high temperatures, directing the irreversible formation of extra-framework octahedral Al species.[34] Tri-coordinated Al was proposed to form by dehydroxylation of Brønsted acid sites followed by dealumination in zeolites, but it was mostly deduced indirectly by combining ^{27}Al MAS NMR, EPR and FT-IR spectra recorded after steaming or heating.[35–37] The distorted local environment and large quadrupolar coupling constant of tri-coordinated Al results in the "NMR-invisible" property, so a probe molecule was employed to certify their fine structure.[38,39] The most direct observation of this Al coordination is achieved by XAS via the presence of the aforementioned pre-edge feature that is indicative of the presence of empty mixed s, p, and d orbitals, i.e., the nature of unsaturated Al.[31] Previous observations of tri-coordinated Al were reversible in zeolite H-Beta and H-Mordenite, such that it could be restored to tetrahedral Al when exposed to air or wet He.[31,40] However, in our case, tri-coordinated Al was stable in steamed Cu-exchanged CHA and MFI. This irreversible nature implies that

the presence of Cu ions could stabilize tri-coordinated Al, which was previously considered as a metastable Al species.
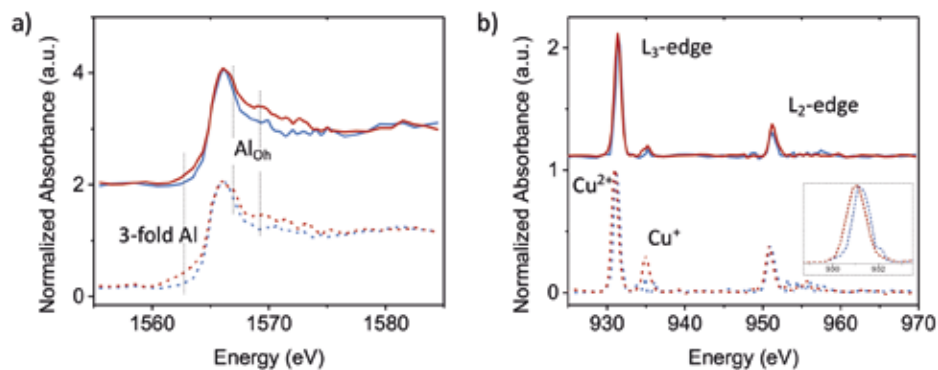
Figure 2.5 Bulk single particle a) Al K-edge and b) Cu L-edge X-ray Absorption Near-Edge Structure (XANES) of fresh (blue) and aged (red) Cu-exchanged CHA (solid) and MFI (dash) zeolites. The inset figure in Figure 2.5b is the Cu^{2+} L$_3$-edge of zeolites Cu-MFI, indicating the edge energy shift of 0.25 eV after steamed aging. Absorption features of octahedral Al (Al$_{Oh}$), tri-coordinated Al (3-fold Al), Cu$^+$ and Cu^{2+} are indicated.

Bulk, single particle Cu L-edge XANES were collected for all samples using the same setup, where the formal oxidation state of copper, indicated by the edge position, is the most straightforward information obtained. A noticeable absorption at ~931.5 eV indicates the predominance of Cu^{2+} in all Cu-exchanged zeolite samples (Figure 2.5b). The effect of steaming on Cu-exchanged CHA was imperceptible. However, in Cu-MFI the aging process induced the reduction of Cu^{2+} to Cu$^+$, evidenced by an obvious increase of the Cu$^+$ peak. Cu$^+$ sites were also observed in FT-IR spectroscopy by employing NO as a probe molecule (Figure 2.6). A well-defined 1810 cm^{-1} band was assigned to the Cu$^+$-ntirosyl adduct, where the Cu$^+$ was generated from auto-reduction of [CuOH]$^+$ during the dehydration process under vacuum before NO dosage. The [CuOH]$^+$ species is thought to have a higher redox ability compared to bare Cu^{2+}, which is pivotal for NH$_3$-SCR to complete the reduction-oxidation cycle.[41] Moreover, one additional different Cu$^+$ site represented by the 1788 cm^{-1} band was detected in the aged Cu-MFI. This Cu$^+$ was formed in the aging process of hydrothermal treatment in an oxidative atmosphere. Similar finding of Cu$^+$ formation under oxidizing conditions at 400 or 500 °C were previously detected by in-situ XANES and Rietveld Refinement of in-situ powder XRD patterns in Cu-SSZ-13.[11,13,42] Additionally, a theoretical study of Cu speciation in CHA indicated that when both H$_2$O and O$_2$ exist at temperatures higher than 673 K, Cu$^+$ located at a 1Al Cu-exchanged site is thermodynamically favorable.[43] Considering that Cu$^+$ has a fully filled d orbital,

it is not surprising to observe the formation of Cu⁺, which then most likely is stabilized by defects generated by the steaming of zeolite Cu-MFI.
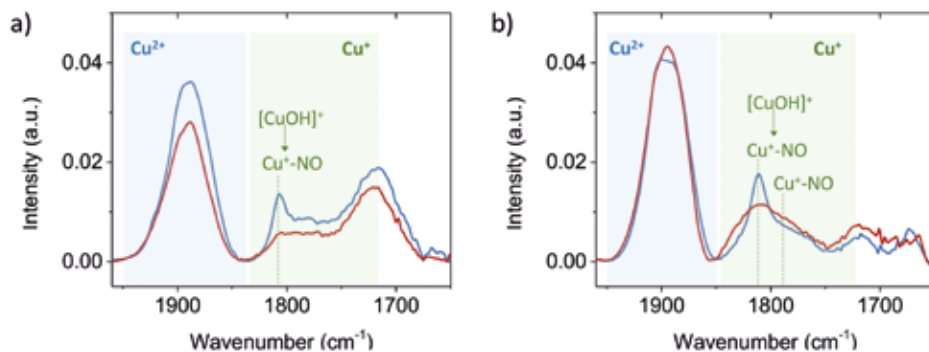
Figure 2.6 Low-temperature NO-adsorbed Fourier-Transform Infrared (FT-IR) spectroscopy data on fresh (blue) and aged (red) Cu-exchanged zeolites in the N-O stretching region of a) CHA and b) MFI at low NO equilibrium pressure of 0.1 mBar at 77 K. The blue label represents mono-nitrosyl adducts in Cu^{2+} sites, and the green labels represent the mono-nitrosyl adducts in Cu^+ sites.

Meanwhile, a subtle change of Cu local environment in Cu-MFI after aging is evidenced by a slight shift of the Cu^{2+} peak in Figure 2.5b. The edge position in Cu L-edge XANES is an indicator of Cu^{2+} geometric structure due to the crystal field splitting of the d orbital.[22] Although it is difficult to differentiate Cu^{2+} coordination geometries in Cu-exchanged zeolites merely by Cu L-edge XANES because of the complexity of the Cu^{2+} local environment, the shift of the Cu^{2+} edge position can be explained by a change of the Cu-O bonding length or geometric structure supported by multiplet calculations (Figure 2.7), which was also observed in previous studies.[23,44] A general trend of negative shift of Cu^{2+} L-edge position was shown when lengthening the Cu-O bond in a fixed Cu^{2+} coordination. The effect of changing Cu-O bond length on the Cu^{2+} L_3-edge position was examined in Cu^{2+} references with different geometric structures based on a previous study.[23] Malachite (octahedral Cu^{2+}) with a 0.147 Å longer average Cu-O bond length compared to La_2CuO_4 (octahedral Cu^{2+}), showed a negative shift of 0.64 eV in the Cu^{2+} L_3-edge. Similarly, $Y_2Cu_2O_5$ (square planar Cu^{2+}) with a 0.034 Å longer average Cu-O bond length compared to CuO (square planar Cu^{2+}), showed a negative shift of 0.21 eV in the Cu^{2+} L-edge. Accordingly, every 0.02 Å longer of Cu-O bond leads to a 0.1 eV negative shift of the Cu^{2+} L_3-edge. In Cu-exchanged zeolites, the average Cu-O bond length is 1.95 Å. However, even upon steaming treatment up to 750 °C, the average Cu-O bond length was only 0.02 Å longer when analyzed by EXAFS.[45] Therefore, the shifting of the

Cu^{2+} L-edge peak of 0.25 eV in the bulk XANES of zeolites Cu-MFI would be ascribed to the steam-induced distortion of fully saturated Cu^{2+} center that Cu-O bond length and/or the geometric structure of Cu^{2+} could change during the steaming process. In contrast, no obvious change of the Cu^{2+} local environment was detected in Cu-CHA, explaining why it retained NH₃-SCR activity.
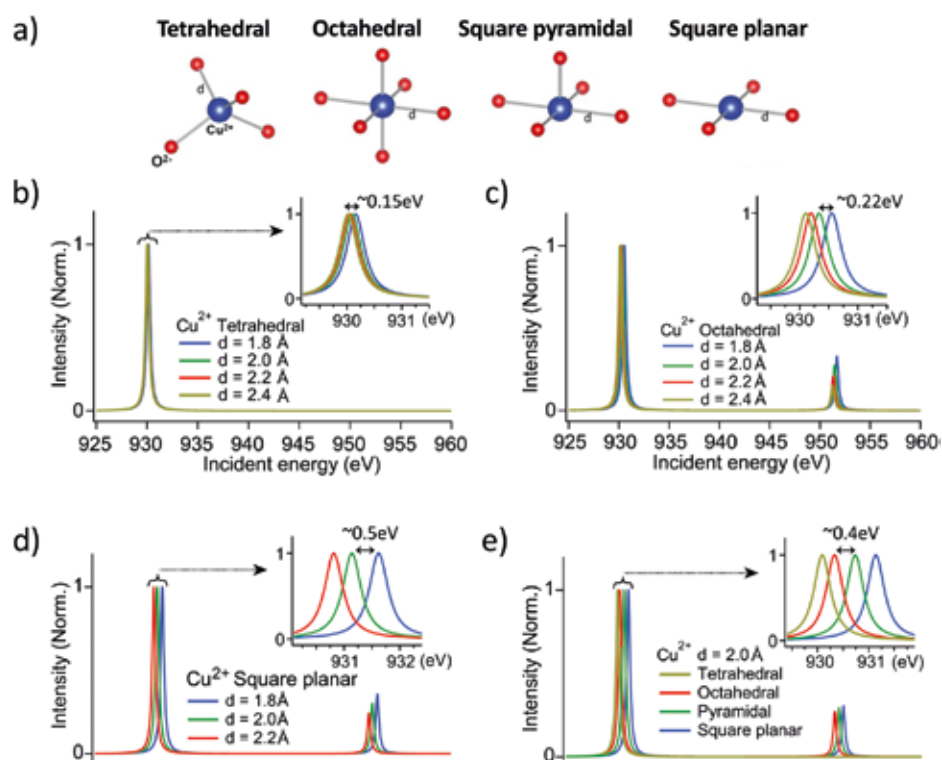

Figure 2.7 a) Illustration of Cu^{2+} in tetrahedral, octahedral, square pyramidal and square planar geometries. Multiplet calculations of Cu^{2+} in geometric structure b) tetrahedral, c) octahedral and d) square planar with Cu-O bond ranging from 1.8-2.4 Å. e) Multiplet calculations of Cu^{2+} in various geometric structures with a fixed Cu-O bond length of 2 Å.

The bulk XANES spectra provide an overview of catalyst properties that correlate with NH₃-SCR performance. Figure 2.8 summarizes bulk information obtained from bulk single particle XANES of Al and Cu, i.e., the relative amounts of Cu$^+$, Al$_{Oh}$ and tri-coordinated Al of fresh/aged Cu-exchanged CHA/MFI. There is a clear difference in the Al coordination between fresh and aged NH₃-SCR active zeolite Cu-CHA indicating that part of the framework tetrahedral Al transformed to octahedral Al and tri-coordinated Al. This dealumination after aging was confirmed by the loss of Brønsted acid sites via NH₃-TPD, indicating the degree of

framework Al degradation was not the dominant factor for catalyst deactivation, especially at temperatures higher than 250 °C when comparing the zeolites Cu-CHA-aged and Cu-MFI-fresh. The limited impact of the Brønsted acidity based on tetrahedral framework Al was previously studied both kinetically and spectroscopically, showing that Brønsted acid sites were not the rate limiting step in the NH_3-SCR reaction cycle and even that the extra-framework Al could have a positive influence on the reaction rate.[46–48]
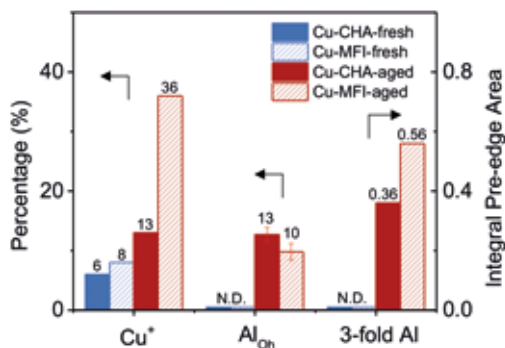
Figure 2.8 Comparison of Cu^+, Al_{Oh} and tri-coordinated Al amounts in fresh and aged Cu-exchanged zeolites CHA and MFI. The left axis represents the percentage of Cu^+ and Al_{Oh}. The axis on the right indicates the integrated pre-edge area determined from the normalized Al K-edge X-ray Absorption Near-Edge Structure (XANES) spectra. Error bars for the percentage of Al_{Oh} were determined from the Least-Square Linear Combination (LSLC) fitting. The references information, quantification results can be found in Figures AIII1-2 and Tables AIII1-2.

The common feature shared by these three active Cu-exchanged zeolites is the low percentage of Cu^+, emphasizing the vital role played by the nature of Cu species in NH_3-SCR. The Cu redox cycle is involved in the NH_3-SCR reaction where both reduction and oxidation half cycles would generate N_2.[7,49,50] In Cu-MFI-aged, a high percentage of Cu sites start their redox cycle from $[Cu(NH_3)_2]^+$ oxidation, which is considered as the rate-limiting step at temperatures lower than 250 °C, and that $[Cu(NH_3)_2]^+$ migrates and then oxidizes to $[Cu(NH_3)_2]^{2+}$.[7,8,51] The local defects generated by steaming might constrain this diffusion of $[Cu(NH_3)_2]^+$, which is linked with the low NO conversion in Cu-MFI-aged. With increasing temperature, the NH_3 ligand releases, and the oxidation of Cu^+ is thermally accelerated and thus the activity is restored in the higher temperature regions of NH_3-SCR.

In comparison with Cu-MFI, Cu-CHA, with a smaller pore size, was more resistant to hydrothermal treatment with slightly less Al leaching, as previously reported.[27] Therefore, the higher activity and stability of Cu-CHA-aged can

be attributed to well-preserved Cu^{2+} sites that balance framework Al, in both terms of oxidation state and geometric structure, which enable NH_3 solvation during reaction. In contrast, the Cu^{2+} sites in Cu-MFI seemed more susceptible to the aging treatment. Apart from the higher percentage of Cu^+ in aged Cu-MFI, our bulk single particle Cu L-edge XANES data together with the multiplet calculations provide evidence for a more distorted local structure of Cu^{2+}.
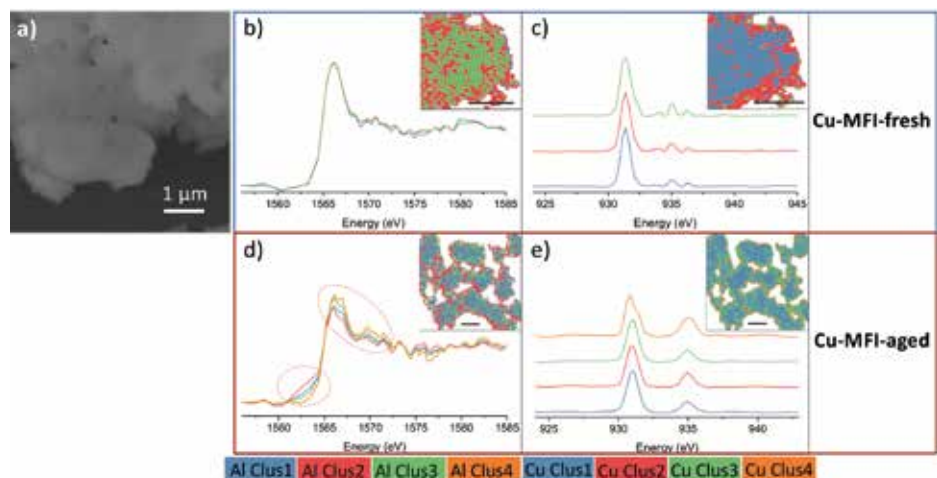
2.3.2 Phase Heterogeneities within Catalyst Particles
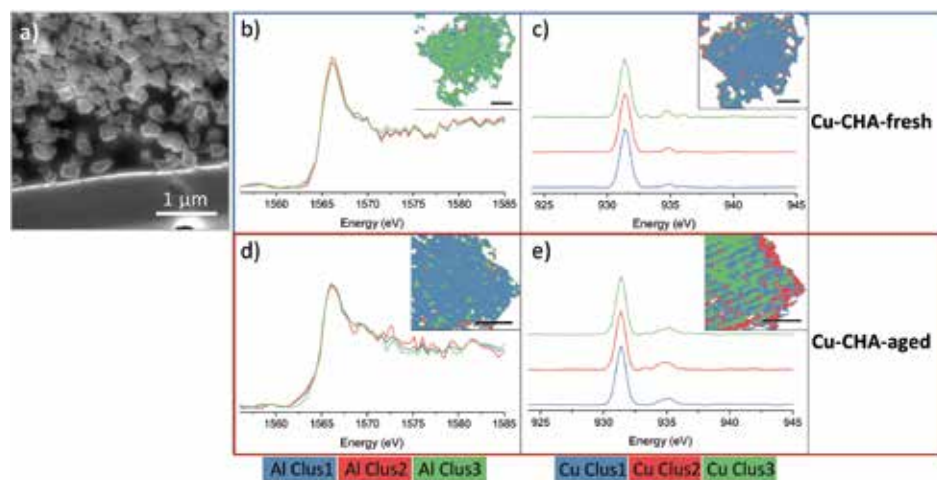
Figure 2.9 a) Scanning Electron Microscopy (SEM) image of Cu-exchanged zeolite CHA. b-e) Results of Principal Component Analysis (PCA) and Cluster Analysis (CA) on the Al and Cu STXM-XANES (Scanning Transmission X-ray Microscopy-X-ray Absorption Near-Edge Structure) data of Cu-exchanged zeolite CHA. b) Al K-edge XANES and c) Cu L_3-edge XANES and the corresponding distribution map (inset) of Cu-CHA-fresh. d) Al K-edge XANES and e) Cu L_3-edge XANES and the corresponding distribution map (inset) of Cu-CHA-aged. The intensity of the Cu^{2+} L_3-edge was normalized to 1 (as done in the processing of the bulk spectra). In the inserted distribution maps, the scale bars represent 1 μm and the pixel size is 25×25 nm². The Field of View (FOV) of the inserted map is 4.55×5.00 μm² in b-c), 2.70×3.05 μm² in d-e).

The scanned area was processed in a spatially resolved manner by PCA and *k*-means CA after filtering background pixels. With this method, the most similar spectra end up in the same cluster, which allows analysis of the spatial distribution of different phases in a sample without using *a priori* knowledge about the phases that are present. Here, it is important to note that the CA result is only based on spectral correlations and not influenced by any spatial correlations. It should be also added that the number of clusters is assigned manually and not an indication for the actual presence of three different spectroscopic phases – *k*-means CA will always produce the number of clusters

used as an input parameter. In this case we intentionally over-clustered the data by using 3 or 4 clusters to check for any spectroscopically distinct, and possibly minor phases, which would emerge in the average XANES of such (over-)clustered data. Therefore, clusters are the result of grouping pixels based on similarity of their spectra.

Figure 2.10 a) Scanning Electron Microscopy (SEM) image of Cu-exchanged zeolite MFI. b-e) Results of Principal Component Analysis (PCA) and Cluster Analysis (CA) on the Al and Cu STXM-XANES (Scanning Transmission X-ray Microscopy-X-ray Absorption Near-Edge Structure) data of Cu-exchanged zeolite MFI. b) Al K-edge XANES and c) Cu L_3-edge XANES and the corresponding distribution map (inset) of Cu-MFI-fresh. d) Al K-edge XANES and e) Cu L_3-edge XANES and the corresponding distribution map (inset) of Cu-MFI-aged. The intensity of the Cu^{2+} L_3-edge was normalized to 1 (as done in the processing of the bulk spectra). In the inserted distribution maps, the scale bars represent 1 μm and the pixel size is 25×25 nm². The Field of View (FOV) of the inserted map is 2.15×2.05 μm² in b-c), 5.05×5.30 μm² in d-e).

Generally, both Al K-edge and Cu L-edge XANES spectra of clusters in an individual zeolite Cu-CHA particle were the same within noise level. In zeolite Cu-CHA-fresh, a spatially uniform local chemical environment of Al and Cu was found within zeolite particles, indicated by a segmentation result of the measured particles and the corresponding XANES shown in Figure 2.9. In contrast, in aged Cu-CHA, a slightly lower amount of tri-coordinated Al was observed in Al Clus3 and Cu Clus2, which are preferentially present at the edge of the particle, and showed a slightly significant increase of Cu^+. However, the crystal size of zeolite CHA was found to be 100-250 nm by SEM analysis (Figure 2.9a), suggesting that the STXM-measured particle was an agglomerate of nanocrystals. The spatial resolution of 50 nm (beam size) was not high enough

to study the differences of chemical distribution in single nanocrystal zeolite CHA. Thus, the tiny variation among clusters found in Cu-CHA cannot be used as an indicator of Al or Cu heterogeneity at the single crystallite level but only at the nanocrystal agglomerate level.

The crystal size of Cu-exchanged MFI is 0.2 to a few microns, which enables spatial analysis at the single particle level. It is important to emphasize that this zeolite was an industrially manufactured catalyst, making insights especially valuable and difficult to obtain. Figure 2.10 shows Al and Cu cluster maps of fresh and aged Cu-MFI. Tetrahedral framework Al is distributed homogeneously in fresh Cu-MFI. Although the Cu clusters in Cu-MFI-fresh exhibited a pattern suggesting that Cu Clus1 was surrounded by Cu Clus2, and Cu Clus3 is preferentially located at the edge of the particle, the dissimilarity of the corresponding XANES spectra was found to be negligible within the noise level (Figure 2.10c); the three clusters were therefore interpreted as identical with respect to Cu oxidation state. Within the noise level we did not find evidence for the presence of more than one spectroscopic phase for both Al and Cu for the single catalyst particle data in fresh Cu-MFI.

As for the deactivated Cu-MFI-aged, statistically significant spatial heterogeneities of spectroscopically different phases of Al and Cu were discriminated within a catalyst particle (Figure 2.10d-e). A pattern of clusters was found, illustrating the slightly different Al geometries of octahedral and three-fold coordination between clusters. A strong degree of framework degradation was found to be preferentially located at the external surface of individual zeolite particles, as is evidenced by the distribution of Al Clus2 (representing the phase with tri-coordinated Al), and Al Clus4 (more octahedral Al), in Figure 2.10d. The oxidation state of Cu within this aged zeolite particle was also not completely uniform. The Cu$^+$ percentage was different between clusters and a shoulder peak assigned to Cu^{2+} was found in Cu Clus4 which are diagnosed as hot spots at the edge of the particles (inserted map in Figure 2.10e). The Cu^{2+} L$_3$-edge was split into two contributing peaks with an energy gap of ~1 eV, which could be explained by tetrahedral and square planar Cu^{2+} supported by the measured references (Table 2.1), multiplet calculations and literature[44]. The absolute edge position in Cu L$_3$-edge XANES could not give an accurate coordination number without measuring Cu compounds in well-defined geometric structures. However, the observed energy gap of ~1 eV between the main peak and the shoulder in the Cu^{2+} edge, presents strong evidence for the co-existence of two different geometric structures of square planar and tetrahedral. We have

included this discussion to reinforce the importance of carefully considering what can be considered as "real" differences in these analyses. Subtle changes of Cu^{2+} geometry now can be detected in through the spatial analysis which are usually covered in the bulk information.

Table 2.1 Cu L_3-edge peak information of Cu references measured by Scanning Transmission X-ray Microscopy (STXM).

	Cu^{2+} L_3-edge position /eV	Oxidation state of Cu	Coordination
CuO	932.04 ± 0.10	+2	square planar
Malachite	931.65	+2	octahedral
$CuAl_2O_4$	930.93, 931.54	+2	tetrahedral + octahedral
Cu_2O	934.72	+1	-

2.3.3 Spatial Correlation between Al and Cu Species

The square planar Cu^{2+} in Cu Clus4 (Figure 2.10e) implied the formation of Cu_xO_y nanoparticles,[52] which are regarded as an inactive species in NH_3-SCR[53]. To more closely investigate their spatial distribution, pixels with an asymmetric Cu^{2+} L_3-edge peak, such as the one shown in Figure 2.10e, i.e., Cu^{2+} present in multiple geometric structures, were selected and divided into four groups that varied in their fraction of square planar Cu^{2+}. It is clear from Figure 2.11a that these pixels with square planar Cu^{2+} (Surface 1-4) were almost exclusively located at the surface of the individual particles, that is, within a few hundred nanometers of the surface of each catalyst particle. This distribution implies that the aggregation of Cu happened near the particle surface, where it then gradually formed Cu_xO_y nanoparticles, strongly indicating that part of Cu^{2+} in Cu-MFI was no longer present as isolated sites after aging.

The deactivation of the Cu-exchanged MFI has previously been linked to the affinity of Cu to form Cu-Cu and Cu-Al bonds, indicating the formation of Cu_xO_y nanoparticles or a $CuAl_xO_y$ spinel phase, respectively.[12,17,54] By correlating the Al and Cu STXM data we could obtain additional information about the spatial correlation between Al and Cu: the very surface area containing a large fraction of Cu_xO_y and Cu^+ also shows partial destruction of the zeolite framework represented by the pronounced pre-edge feature of three-fold Al (Figure 2.11b-c). Due to the co-occurrence of octahedral Al and tetrahedral Cu, a $CuAl_xO_y$ spinel phase cannot be excluded in our case. The destroyed surface layer of Cu-MFI-aged can be explained by the fact that the surface area of each zeolite

particle was the first region that is exposed to steam, and therefore experienced the most severe steaming treatment. The detachment of extra-framework Al then induces migration and subsequently aggregation of Cu ions because it is no longer necessary to have a cation to balance the negative charge from framework Al. In turn, the aggregation of freed, isolated Cu ions causes them to lose their charge balance ability, which further exacerbates the severe framework damage in zeolite MFI. The interplay between degraded Al and Cu eventually leads to the zoning of inactive species that might further limit diffusion of reactants and products through the catalyst particle because of the collapse and blockage of zeolite channels on the catalyst particle surface. All of this leads to the "perfect storm" for deactivation.

Severe degradation of Al and Cu species was predominately found in the region of around 250 nm from the surface. However, the other areas within particles that were less degraded reveal the more general chemical properties of the catalyst. Hence, for a more detailed analysis of these areas, pixels with square planar Cu^{2+} composite, i.e., the surface region marked in orange in Figure 2.11a, were filtered before inspecting the main body of each particle of Cu-MFI-aged. Thus, Cu L-edge XANES of the remaining pixels showed a single Cu^{2+} L-edge peak representing distorted tetrahedral Cu^{2+} or octahedral Cu^{2+}. The classification of the central part of catalyst particle was achieved by examining the first two Principal Components (PC) based on the fact that PC1 closely resembles the average spectrum of all pixels (after background removal) and PC2 represents the strongest deviation from PC1 (being an orthonormal basis vector to PC1 and capturing the second largest variance in the data).

The pixels with a higher contribution of PC2 contained a lower percentage of Cu$^+$. The clusters Center 1-5 were labeled such that the Cu$^+$ amount increased when going from cluster Center 1 to Center 5. The corresponding Al K-edge XANES and Cu L$_3$-edge XANES of each cluster are shown in Figure 2.11d-e. The detailed quantification information of clusters Surface 1-4 and Center 1-5 can be found in Tables AIII3-4.

The clusters Center 1-5 in Figure 2.11a exhibit a spatially random pattern, suggesting that the transformation of Cu^{2+} to Cu$^+$ does not have a preferred location or direction within individual zeolite particles. Based on the estimated amount of degraded Al species obtained from LSLC fitting, all these clusters have a comparable percentage of octahedral Al but vary in tri-coordinated Al, as illustrated in the zoom-in to the pre-edge region in Figure 2.11d. The trend of

increasing three-fold Al coordination when going from cluster Center 1 to Center 5 was accompanied by an increasing Cu^+ percentage (Figure 2.11f). Undoubtedly, hydrolyzation or hydroxylation of Brønsted acidity would destroy the framework structure, directing the formation of defect sites consisting of tri-coordinated Al, such as Al-OH and AlO^+.[31] Subsequently, AlOOH, $Al(OH)_2^+$ and $Al(OH)_3$ might be formed in the presence of water.[12,55]
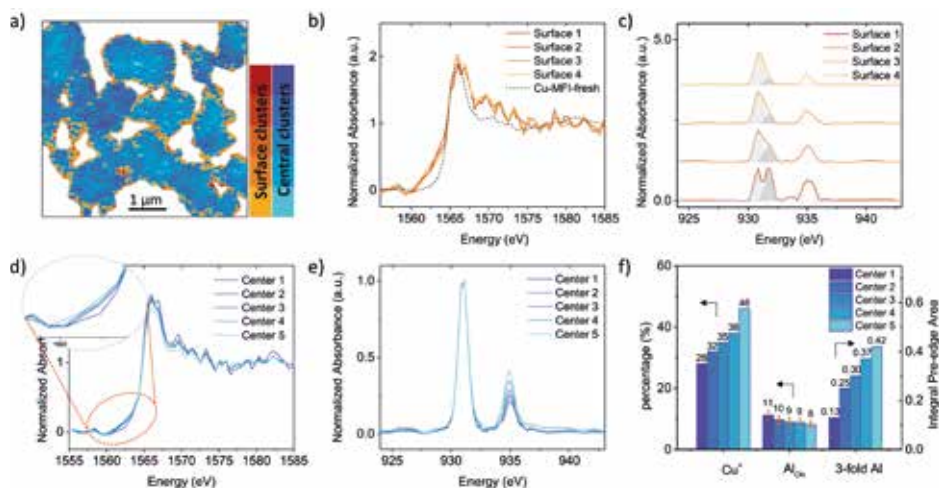
Figure 2.11 Spatial analysis on individual catalyst particles of aged Cu-exchanged zeolite MFI. a) Cluster map of both surface (orange) and central (blue) area in Cu-MFI-aged, where the color gradient represents a pool of pixels sharing similar spectral features. The classification of pixels was based on the deviation of their Cu L_3-edge spectra from the average spectrum of all pixels. Surface clusters 1-4 represent region with more degraded Al and Cu species, which were predominantly found on the surface of individual particle. The Central clusters 1-5 mostly describe the bulk information. STXM-XANES (Scanning Transmission X-ray Microscopy-X-ray Absorption Near-Edge Structure) spectra of b) Al K-edge and c) Cu L_3-edge with deconvolution of the Cu^{2+} peak in clusters Surface 1-4. The STXM-XANES spectra of d) Al K-edge inserted with enlarged pre-edge region and e) Cu L_3-edge in clusters Center 1-5. f) The relative amounts of Cu^+, Al_{Oh} and tri-coordinated Al determined based on the spectra in d-e). The left axis represents percentage, whereas the right axis represents the integrated area of the pre-edge region in Al K-edge XANES spectra.

On the other hand, Cu^+ was created by auto-reduction of either $[CuOH]^+$ or Cu^{2+}. The reduction of Cu^{2+} was proposed to associate with a thermally-driven decomposition of H_2O at temperatures higher than 300 °C, accompanied by the formation of a proton that can balance the framework charge.[56] However, independent of how Cu^+ is generated, Cu^+ could be stabilized by tri-coordinated Al if it is adjacent to the degraded Al site. Finally, considering the intimate

interaction between leached Al and Cu, the formation of CuAl$_x$O$_y$ phase cannot be excluded,[12] which was also proposed from APT studies[17,19] and XAS studies[12].

We have elucidated the deactivation of Cu-exchanged zeolites in terms of local environment and the spatial distribution of both Al and Cu. The sensitivity of XAS to the geometric structure enabled us to discover the "NMR invisible" tri-coordinated Al, which existed in both aged Cu-CHA and aged Cu-MFI. Since dealumination was found in NH$_3$-SCR active catalyst Cu-CHA-aged, the limited degree of framework destruction was not the main reason for the loss of activity. Instead, the loss of isolated Cu sites, which transformed into Cu$_x$O$_y$ nanoparticles or a CuAl$_x$O$_y$ spinel phase that was largely located on the particle surface, was more detrimental to the NH$_3$-SCR reaction. It was previously inferred from X-ray Photoelectron Spectroscopy (XPS) and calorimetry upon adsorption of the probe molecule NH$_3$ that the location of defect sites in zeolite ZSM-5 is mainly concentrated on the external surface of the zeolite crystals.[57] Via our spatial analysis of the data recorded for zeolite Cu-MFI-aged we could now directly visualize this, revealing that the most degraded framework structure is located at the edges of the individual catalyst particles and goes along with the formation of inactive Cu$_x$O$_y$ nanoparticles, which further limit the accessibility of less destroyed Cu sites in the central part of catalyst particles due to framework collapse and channel blockage near surface. This observed Al and Cu zoning is a good example of nanoscale destruction in industrial catalysts, which is caused by surface migration of nanoparticles.[58] The discovery of this minority species of Cu$_x$O$_y$ at the surface (4555 surface pixels from a total of 29759 analyzed pixels) illustrates the power of STXM for nanoscale spatial analysis of catalyst particles.

2.4. Conclusions

The observed variations in catalytic activity and stability between fresh and aged Cu-exchanged zeolites with different framework structures (CHA and MFI) motivated a detailed study of the deactivation factors with respect to the zeolite framework structure, i.e., Al and Cu species. Therefore in this Chapter, we have employed Scanning Transmission X-ray Microscopy (STXM), which combines the main functions of X-ray Absorption Spectroscopy (XAS) and high-resolution imaging, providing abundant information about the local chemical environment in the form of a chemical map of fresh and aged Cu-exchanged zeolites. The results obtained indicate that although the degradation of tetrahedral framework Al to octahedral Al or tri-coordinated Al caused the loss of Brønsted acid sites, NH$_3$-SCR activity was maintained in Cu-exchanged CHA even after aging, which is attributed to the hydrothermally stable framework

structure and well-preserved Cu^{2+}. For Cu-exchanged MFI, the deactivation of NH_3-SCR was induced by the degradation of isolated Cu^{2+} to both Cu^+ and Cu_xO_y nanoparticles after simulated aging. The spatial distribution of both Al and Cu species was explored by inspecting single-pixel spectra, revealing spatial correlations between species and information that is lost in bulk data. We observed zoning of extra-framework Al, Cu^+ and Cu_xO_y on the surface of every individual catalyst particle of the most deactivated zeolite, Cu-MFI-aged. Then, by investigating the main body of each catalyst particle, i.e., excluding the degraded surface regions, a plausible spatial correlation between tri-coordinated Al and Cu^+ was established. Overall, we can conclude that the loss of isolated Cu sites is detrimental to NH_3-SCR performance. Considering the interdependence between framework Al and isolated Cu species, further investigations of a more durable NH_3-SCR catalyst should emphasize the stabilization of isolated Cu active sites. In case of Cu-exchanged zeolites, preservation of isolated Cu relies on the stability of an Al-containing framework. Hence, a hydrothermally stable zeolite lattice is critical for the maintenance of NH_3-SCR activity.

Acknowledgements

REFERENCES

1   P. Granger and V. I. Parvulescu, *Chem. Rev.*, 2011, **111**, 3155–3207.

2   S. Brandenberger, O. Kröcher, A. Tissler and R. Althoff, *Catal. Rev.*, 2008, **50**, 492–531.

3   M. Iwamoto, H. Furukawa, Y. Mine, F. Uemura, S. Mikuriya and S. Kagawa, *J. Chem. Soc. Chem. Commun.*, 1986, 1272–1273.

4   J. H. Kwak, R. G. Tonkyn, D. H. Kim, J. Szanyi and C. H. F. Peden, *J. Catal.*, 2010, **275**, 187–190.

5   A. M. Beale, F. Gao, I. Lezcano-Gonzalez, C. H. F. Peden and J. Szanyi, *Chem. Soc. Rev.*, 2015, **44**, 7371–7405.

6   U. Deka, I. Lezcano-Gonzalez, B. M. Weckhuysen and A. M. Beale, *ACS Catal.*, 2013, **3**, 413–427.

7   C. Paolucci, I. Khurana, A. A. Parekh, S. Li, A. J. Shih, H. Li, J. R. Di Iorio, J. D. Albarracin-Caballero, A. Yezerets, J. T. Miller, W. N. Delgass, F. H. Ribeiro, W. F. Schneider and R. Gounder, *Science*, 2017, **357**, 898–903.

8   A. Marberger, A. W. Petrov, P. Steiger, M. Elsener, O. Kröcher, M. Nachtegaal and D. Ferri, *Nat. Catal.*, 2018, **1**, 221–227.

9   K. A. Lomachenko, E. Borfecchia, C. Negri, G. Berlier, C. Lamberti, P. Beato, H. Falsig and S. Bordiga, *J. Am. Chem. Soc.*, 2016, **138**, 12025–12028.

10   F. Gao, N. M. Washton, Y. Wang, M. Kollár, J. Szanyi and C. H. F. Peden, *J. Catal.*, 2015, **331**, 25–38.

11   C. W. Andersen, E. Borfecchia, M. Bremholm, M. R. V. Jørgensen, P. N. R. Vennestrøm, C. Lamberti, L. F. Lundegaard and B. B. Iversen, *Angew. Chem. Int. Ed.*, 2017, **56**, 10367–10372.

12   P. N. R. Vennestrøm, T. V. W. Janssens, A. Kustov, M. Grill, A. Puig-Molina, L. F. Lundegaard, R. R. Tiruvalam, P. Concepción and A. Corma, *J. Catal.*, 2014, **309**, 477–490.

13   F. Giordanino, E. Borfecchia, K. A. Lomachenko, A. Lazzarini, G. Agostini, E. Gallo, A. V. Soldatov, P. Beato, S. Bordiga and C. Lamberti, *J. Phys. Chem. Lett.*, 2014, **5**, 1552–1559.

14 R. Oord, I. C. ten Have, J. M. Arends,
F. C. Hendriks, J. Schmidt, I. Lezcano-Gonzalez
and B. M. Weckhuysen,
Catal. Sci. Technol., 2017, **7**, 3851–3862.

15 A. Godiksen, F. N. Stappen, P. N. R. Vennestrøm,
F. Giordanino, S. B. Rasmussen, L. F. Lundegaard
and S. Mossin, *J. Phys. Chem. C*, 2014, **118**,
23126–23138.

16 I. L. C. Buurmans and B. M. Weckhuysen,
Nat. Chem., 2012, **4**, 873–886.

17 J. E. Schmidt, R. Oord, W. Guo, J. D. Poplawsky
and B. M. Weckhuysen,
Nat. Commun., 2017, **8**, 1666.

18 F. Meirer and B. M. Weckhuysen,
Nat. Rev. Mater., 2018, **3**, 324–340.

19 J. E. Schmidt, X. Ye, I. K. van Ravenhorst, R. Oord,
D. A. Shapiro, Y. Yu, S. R. Bare, F. Meirer, J. D.
Poplawsky and B. M. Weckhuysen,
ChemCatChem, 2019, **11**, 488–494.

20 S. J. Schmieg, S. H. Oh, C. H. Kim, D. B. Brown,
J. H. Lee, C. H. F. Peden and D. H. Kim,
Catal. Today, 2012, **184**, 252–261.

21 S. Kalirai, P. P. Paalanen, J. Wang, F. Meirer and
B. M. Weckhuysen, *Angew.
Chem. Int. Ed.*, 2016, **55**, 11134–11138.

22 S. J. George, S. P. Cramer, M. D. Lowery and
E. I. Solomon, *J. Am. Chem. Soc.*, 1993, **115**,
2968–2969.

23 M. Grioni, J. B. Goedkoop, R. Schoorl,
F. M. F. de Groot, J. C. Fuggle, F. Schäfers,
E. E. Koch, G. Rossi, J.-M. Esteva and
R. C. Karnatak, *Phys. Rev. B*, 1989, **39**, 1541–1545.

24 R. Sarangi, N. Aboelella, K. Fujisawa,
W. B. Tolman, B. Hedman, K. O. Hodgson and E. I.
Solomon, *J. Am. Chem. Soc.*, 2006, **128**, 8286–
8296.

25 I. Garcia-Torregrosa, Y. G. Geertzema,
A. S. M. Ismail, T. Lee, F. M. F. Groot and
B. M. Weckhuysen,
ChemPhotoChem, 2019, **3**, 1238–1245.

26 A. Uldry, F. Vernay and B. Delley,
Phys. Rev. B, 2012, **85**, 125133.

27 D. W. Fickel, E. D'Addio, J. A. Lauterbach and R. F.
Lobo, *Appl. Catal. B Environ.*, 2011, **102**, 441–448.

28 J. H. Kwak, D. Tran, S. D. Burton, J. Szanyi,
J. H. Lee and C. H. F. Peden,
J. Catal., 2012, **287**, 203–209.

29 S. Malola, S. Svelle, F. L. Bleken and O. Swang,
Angew. Chem. Int. Ed., 2012, **51**, 652–655.

30 A. M. Beale, A. M. J. van der Eerden,
D. Grandjean, A. V Petukhov, A. D. Smith and
B. M. Weckhuysen, *Chem. Commun.*, 2006, 4410.

31 J. A. van Bokhoven, A. M. J. van der Eerden and
D. C. Koningsberger, *J. Am. Chem. Soc.*, 2003,
125, 7435–7442.

32 B. H. Wouters, T. H. Chen and P. J. Grobet,
J. Am. Chem. Soc., 1998, **120**, 11419–11425.

33 I. J. Drake, Y. Zhang, M. K. Gilles, C. N. Teris Liu, P.
Nachimuthu, R. C. C. Perera, H. Wakita and A. T.
Bell, *J. Phys. Chem. B*, 2006, **110**, 11665–11676.

34 J. A. van Bokhoven, D. C. Koningsberger,
P. Kunkeler and H. van Bekkum, *J. Catal.*, 2002,
211, 540–547.

35 F. Deng, Y. Du and C.-H. Ye,
Magn. Reson. Imaging, 1996, **14**, 945–946.

36 J. Brus, L. Kobera, W. Schoefberger,
M. Urbanová, P. Klein, P. Sazama, E. Tabor,
S. Sklenak, A. V. Fishchuk and J. Dědeček,
Angew. Chem. Int. Ed., 2015, **54**, 541–545.

37 R. M. Mihályi, M. Kollár, P. Király, Z. Karoly and
V. Mavrodinova, *Appl. Catal. A Gen.*, 2012,
417–**418**, 76–86.

38 X. Yi, K. Liu, W. Chen, J. Li, S. Xu, C. Li, Y. Xiao,
H. Liu, X. Guo, S.-B. Liu and A. Zheng,
J. Am. Chem. Soc., 2018, **140**, 10764–10774.

39 S. Xin, Q. Wang, J. Xu, Y. Chu, P. Wang, N. Feng,
G. Qi, J. Trébosc, O. Lafon, W. Fan and F. Deng,
Chem. Sci., 2019, **10**, 10159–10169.

40 L. A. Bugaev, J. A. van Bokhoven,
A. P. Sokolenko, Y. V. Latokha and L. A. Avakyan,
J. Phys. Chem. B, 2005, **109**, 10771–10778.

41 A. Martini, E. Borfecchia, K. A. Lomachenko,
I. A. Pankin, C. Negri, G. Berlier, P. Beato,
H. Falsig, S. Bordiga and C. Lamberti,
Chem. Sci., 2017, **8**, 6836–6851.

42 E. Borfecchia, K. A. Lomachenko, F. Giordanino,
H. Falsig, P. Beato, A. V. Soldatov, S. Bordiga and
C. Lamberti, *Chem. Sci.*, 2015, **6**, 548–563.

43 C. Paolucci, A. A. Parekh, I. Khurana,
J. R. Di Iorio, H. Li, J. D. Albarracin Caballero,
A. J. Shih, T. Anggara, W. N. Delgass, J. T. Miller, F.
H. Ribeiro, R. Gounder and W. F. Schneider,
J. Am. Chem. Soc., 2016, **138**, 6028–6048.

44 K. Shimizu, H. Maeshima, H. Yoshida, A. Satsuma
and T. Hattori,
Phys. Chem. Chem. Phys., 2001, **3**, 862–866.

45 P. N. R. Vennestrøm, T. V. W. Janssens, A. Kustov,
M. Grill, A. Puig-Molina, L. F. Lundegaard,
R. R. Tiruvalam, P. Concepción and A. Corma,
J. Catal., 2014, **309**, 477–490.

46 S. A. Bates, A. A. Verma, C. Paolucci, A. A. Parekh,
T. Anggara, A. Yezerets, W. F. Schneider, J. T.
Miller, W. N. Delgass and F. H. Ribeiro, *J. Catal.*,
2014, **312**, 87–97.

2

47 I. Lezcano-Gonzalez, U. Deka, B. Arstad,
    A. van Yperen-De Deyne, K. Hemelsoet,
    M. Waroquier, V. van Speybroeck,
    B. M. Weckhuysen and A. M. Beale,
    Phys. Chem. Chem. Phys., 2014, **16**, 1639–1650.

48 T. V. W. Janssens, H. Falsig, L. F. Lundegaard,
    P. N. R. Vennestrøm, S. B. Rasmussen,
    P. G. Moses, F. Giordanino, E. Borfecchia,
    K. A. Lomachenko, C. Lamberti, S. Bordiga,
    A. Godiksen, S. Mossin and P. Beato,
    ACS Catal., 2015, **5**, 2832–2845.

49 M. Moreno-González, R. Millán, P. Concepción,
    T. Blasco and M. Boronat,
    ACS Catal., 2019, **9**, 2725–2738.

50 C. Paolucci, A. A. Verma, S. A. Bates,
    V. F. Kispersky, J. T. Miller, R. Gounder,
    W. N. Delgass, F. H. Ribeiro and W. F. Schneider,
    Angew. Chem. Int. Ed., 2014, **53**, 11828–11833.

51 F. Gao, D. Mei, Y. Wang, J. Szanyi and
    C. H. F. Peden, *J. Am. Chem. Soc.*, 2017, **139**, 4935–
    4942.

52 J. B. Forsyth and S. Hull,
    J. Phys. Condens. Matter, 1991, **3**, 5257–5261.

53 A. Wang, Y. Chen, E. D. Walter, N. M. Washton,
    D. Mei, T. Varga, Y. Wang, J. Szanyi, Y. Wang,
    C. H. F. Peden and F. Gao,
    Nat. Commun., 2019, **10**, 1137.

54 J. Song, Y. Wang, E. D. Walter, N. M. Washton,
    D. Mei, L. Kovarik, M. H. Engelhard, S. Prodinger,
    Y. Wang, C. H. F. Peden and F. Gao,
    ACS Catal., 2017, **7**, 8214–8227.

55 P. A. Jacobs and H. K. Beyer,
    J. Phys. Chem., 1979, **83**, 1174–1177.

56 P. H. Kasai and R. J. Bishop,
    J. Phys. Chem., 1977, **81**, 1527–1529.

57 V. Bolis, S. Maggiorini, L. Meda, F. D'Acapito,
    G. T. Palomino, S. Bordiga and C. Lamberti,
    J. Chem. Phys., 2000, **113**, 9248–9261.

58 J. A. Moulijn, A. E. van Diepen and F. Kapteijn,
   *Appl. Catal. A Gen.*, 2001, **212**, 3–16.

Deactivation of Cu-exchanged Automotive Emissions NH$_3$-Selective Catalytic Reduction Catalysts Elucidated with Nanoscale Resolution using Scanning Transmission X-ray Microscopy

2

CHAPTER

3

Probing the Location and Speciation of Elements in Zeolites with Correlated Atom Probe Tomography and Scanning Transmission X-Ray Microscopy

*J. E. Schmidt, X. Ye, I. K. van Ravenhorst, R. Oord,
D. A. Shapiro, Y. -S. Yu, S. R. Bare, F. Meirer,
J. D. Poplawsky, B. M. Weckhuysen,*

ABSTRACT
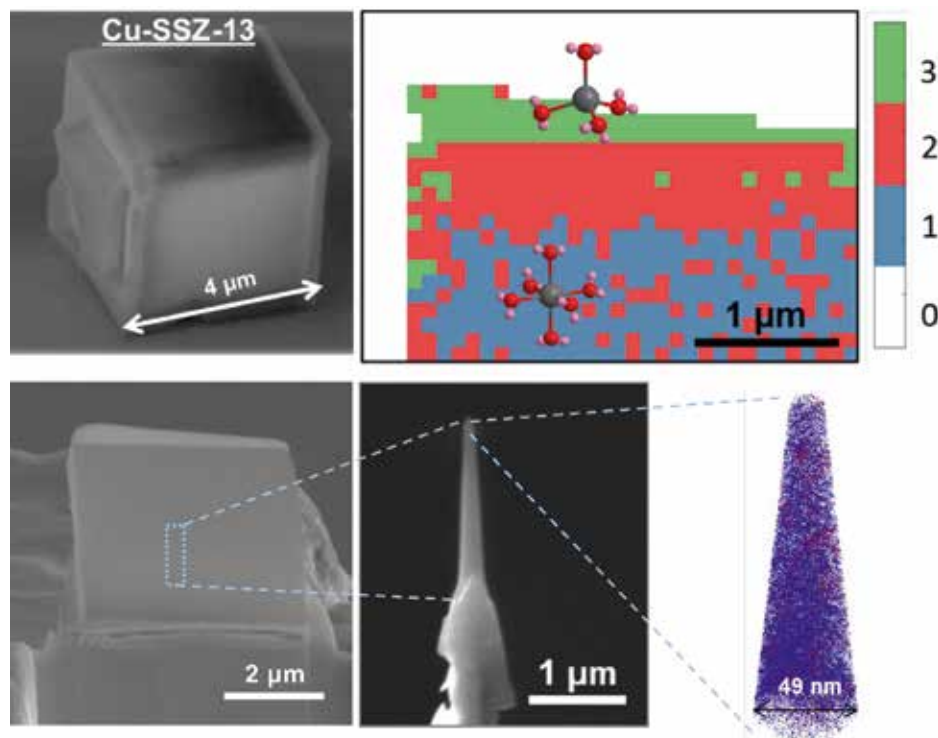
Characterizing materials at the nanoscale to provide insights into structure-property-performance relationships continues to be a challenging research target due to the inherently low signal from small sample volumes. This is even more difficult for nonconductive materials, such as zeolites. In this Chapter, the characterization of a single Cu-exchanged zeolite crystal, namely Cu-SSZ-13, used for NO_x reduction in automotive emissions, that was subject to a simulated 135,000-mile aging, is studied. By correlating Atom Probe Tomography (APT), a single atom microscopy method, and Scanning Transmission X-ray Microscopy (STXM), which produces high spatial resolution X-ray Absorption Near-Edge Structure (XANES) maps, we show that a spatially non-uniform portion of the Al was removed from the zeolite framework. The techniques reveal that this degradation process is heterogeneous at length scales from micrometers to tens of nanometers, providing complementary insights into the long-term deactivation of this catalyst system.

3.1   Introduction

Multiscale material complexity and heterogeneity is one of the key drivers for ever more advanced characterization research.[1–9] Zeolites are heterogeneous catalysts that exhibit such complexity, spanning several orders of magnitude, from their catalytic active sites (sub-nanometer) to large industrial reactors (tens of meters), and even within single crystals they contain compositional gradients and defects spanning sub-nanometer to micrometer length scales.[4] There are many characterization techniques that provide spatially resolved information, with varying degrees of chemical information content, but there are few characterization techniques that provide both the necessary high spatial resolution and chemical information content. Additionally, many methods provide only 2D or near-surface information.[4,5]

A range of well-developed techniques are available for obtaining chemical information from solid catalysts with length scales from micrometer to nanometer, however, chemical imaging of solids catalysts with nanometer scale resolution is still very challenging, especially for an individual catalyst particle.[4] Two characterization techniques that provide high spatial resolution information are Atom Probe Tomography (APT) and Scanning Transmission X-ray Microscopy (STXM).[10–19] APT is a single atom 3-D microscopy that is able to reconstruct the 3-D position and chemical identity of all atoms with sub-nm resolution from a needle shaped specimen with dimensions of tens to hundreds of nanometers, making it the highest resolution technique to provide 3-D elemental identification.[10–14] STXM relies on a Zone Plate (ZP) to focus soft X-rays emitted by a synchrotron onto a small spot on the sample, through which the sample is scanned. By measuring the total transmitted intensity of the beam as a function of energy, it can give information about local environment of the measured chemical element and its abundance. STXM (especially in combination with ptychography) is one of the highest resolution techniques capable of providing this information (possible resolution <50×50 nm^2 pixel size, and even in the range of 10 nm and below when using ptychography[19,20]) that is also non-destructive to zeolites as it uses soft X-rays.[15,16]

Both APT and STXM have been applied to zeolite-based catalysts by a number of research groups, resulting in a significant body of accumulated knowledge.[15,21,30,31,22–29] However, there is no report that correlates results of the two characterization techniques. In this Chapter, we have applied APT and STXM in an integrated fashion to study the same single crystal of a laboratory aged (135,000 mile simulation) sample of copper-exchanged zeolite SSZ-13

(Cu-SSZ-13, with the CHA framework topology), which is the same sample as we previously studied with APT alone.[24] We chose this sample as the ~4 µm crystal size makes spatially resolved characterization studies meaningful, and as the sample was previously studied any potential beam damage can be assessed, a known problem when probing zeolites with electron beams.[32] Furthermore, the ion exchange with Cu-ions makes this a difficult material to characterize with conventional ^{27}Al Magic Angle Spinning solid-state Nuclear Magnetic Resonance (MAS ssNMR) spectroscopy due to interference from paramagnetic Cu, motivating us to explore other characterization methods. The results described in this Chapter indicate that it is possible to correlate the results of these two high-resolution techniques, and thereby gain information on the location and local environment of the elements present to construct a more complete understanding of how the material resists deactivation under demanding tailpipe conditions.

3.2   Experimental Section

3.2.1   Catalyst Preparation

The aged zeolite Cu-SSZ-13 with a Si/Al ratio of ~20 (determined by Inductively Coupled Plasma - Optical Emission Spectrometry, ICP-OES) was prepared using the same method as reported in reference [24]. Hereto, N,N,N-trimethyl-1-adamantammonium (20 % in H_2O solution, Sachem) was added to a mixture of tetraethyl orthosilicate (TEOS, Aldrich, >99 %) and aluminum isopropoxide (Acros Organics 98 %+), followed by an aging procedure at room temperature for 4 days. A 51 % HF solution (Acros organics, 48–51 %) was added and the solution was stirred until it turned into homogeneous gel, which was then transferred into Teflon-lined autoclaves for hydrothermal treatment at 150 °C for 6 days. The white product was collected and washed thoroughly with a large excess of demineralized water and dried overnight at 60 °C. Calcination was required to remove organic compounds that remained in the zeolite pores. The as-synthesized zeolite SSZ-13 was dehydrated at 150 °C for 2 h and calcination was sequentially performed at 580 °C for 6 h and then cooled down to room temperature. The temperature ramping rate was 2 °C/min for the entire calcination process.

For the Cu ion exchange with zeolite SSZ-13, 1 g calcined SSZ-13 was dispersed in a 0.1 M $CuSO_4$ (Merck ACS, ISO, Reag. Ph Eur) solution at 80 °C for 2 h. The obtained Cu-SSZ-13 was thoroughly washed with demineralized water and dried overnight at 60 °C. The Cu-SSZ-13 was then dehydrated at 150 °C for 2 h followed

by calcination at 550 °C for 4 h in a muffle furnace with a temperature ramping rate of 2 °C/min.

The steaming process followed the industry standard simulation procedure for a 135,000-mile vehicle-aged catalyst, as described in Chapter 2. The 10 % steam in air flow was produced by using a H_2O bubbler at 47 °C and was introduced into the zeolite Cu-SSZ-13 placed in a porcelain boat-shaped crucible in a tube furnace at 120 °C to prevent H_2O condensation. The steaming procedure was conducted at 800 °C using a ramping rate of 2°C/min and held for 16 h. It was then cooled down to room temperature in dry air to obtain the aged zeolite Cu-SSZ-13.

3.2.2   Catalyst Characterization

Crystals of aged zeolite Cu-SSZ-13 were attached to Mo Omniprobe® Lift-Out Grids and thinned to 0.5 μm, as shown in Figure 3.2, using a Ga Focused Ion Beam (FIB) and Kleindiek nanomanipulator.[24]

The STXM measurements on the cross section were performed at the Advanced Light Source (ALS) beamline 11.0.2 of Lawrence Berkeley National Laboratory, Berkeley, California, USA.[33,34] For the STXM experiment the grid with the thinned Cu-SSZ-13 was attached to the sample holder using double sided tape. The sample chamber was evacuated and then backfilled with He to a pressure of 200 Torr. The soft X-ray beam focused on the sample with a 50 nm spot size after going through a 45 nm Zone Plate (ZP) and sequentially an Order Sorting Aperture (OSA) with a 90 μm pinhole. The focused X-ray beam reached the sample to form a point-by-point image by moving the sample plate step-by-step, resulting in an X-ray absorption spectrum at each pixel. A stack of transmission images with a 4×4 μm² Field of View (FOV) and 50×50 nm² pixel size, was obtained by varying the incident X-ray energy in the energy region of 1557-1585 eV for Al K-edge imaging. Because the Cu concentration was too low to detect, we did not perform STXM on Cu L-edge of the cross section.

After performing the STXM measurements, a needle shaped specimen was carefully removed from the cross section using Ga FIB milling and then studied with APT using the LEAP 4000XR local electrode atom probe equipped with laser pulsing capabilities and an energy compensating reflectron lens in the Center for Nanophase Materials Sciences (CNMS) at Oak Ridge National Laboratory (ORNL). The APT experiment was performed on a tungsten wire instead of a Si microtip array, which is the more historical method of conducting APT experiments.[35–37] The APT data analysis was performed using CAMECA's IVAS

software. We have previously reported in detail on these measurements and their analysis.[18,23,24,38] Briefly, atoms collected by an APT experiment is reconstructed into the three-dimensional space. Isoconcentration is created by connecting points in space with equal element concentration to show the heterogeneity at the scale of tens of nanometers. Smaller clusters and zonings of chemical elements are determined by Nearest Neighbor Distribution (NND) analysis where atom pair distance is plotted as a function of counts and is compared to the randomized pair distance. The variation within an identified cluster can be further examined by Radial Distribution Function (RDF) analysis that the local concentration of a selected atom is normalized by the bulk concentration.

STXM-XANES data of the cross section was analyzed using the aXis2000 (http://unicorn.mcmaster.ca/aXis2000.html) and TXM-Wizard[39] software packages. A stack of transmission images, recorded in energy sequences, was aligned in aXis2000 to ensure the position of cross section remained stable. The aligned transmission images were then converted to absorbance mode represented as Optical Density (OD), by defining the Absorbance (A) as $A = -\ln(I/I_o)$, where I_o and I are X-ray intensities before and after going through the sample.[16] The stack of OD images was subsequently loaded in the TXM-Wizard software to obtain detailed analysis on chemical composition and spatial distribution of Al. The stack of images was cropped and binned by combining 2×2 pixels into one to enhance the signal to noise ratio in XANES through lowering spatial resolution, resulting in images with a 3.4×2.4 μm^2 FOV and 100×100 nm^2 pixel size. To analyze the area without any interfering absorption from deposited Pt, a mask was created using Principal Component Analysis (PCA) and Cluster Analysis (CA) of the raw data, which clearly separated the zeolite contribution from the background and Pt. Subsequently, the mask was used to filter the background area and deposited Pt in the cross section; the absorption profiles of both Pt-deposit and background regions did not show an edge jump across the Al K-edge (Figure 3.1). Therefore, only pixels showing an edge jump at the Al K-edge (blue area in Figure 3.1) remained to conduct further analysis.

An edge jump filter was then employed to remove the pixels with an extremely low energy jump, i.e., pixels dominated by noise, followed by applying a normalization filter and removing pixels with a distorted pre-edge or post-edge. The bulk XANES spectrum was taken as the average spectrum of all remaining single pixel spectra in the image. Energy calibration of the Al K-edge XANES was carried out by shifting the white line maximum of the bulk spectrum to 1566.2 eV, referring to the Al K-edge XANES of zeolite ZSM-5 used as a standard and measured previously by our

group.[30] The local chemical environment of Al in the cross section was analyzed by Least-Square Linear Combination (LSLC) fitting of the bulk XANES, taking zeolite ZSM-5 and α-Al_2O_3 as references for tetrahedral Al and octahedral Al, respectively. The fitting range covered the edge region from 1563.20 eV to 1568.70 eV.
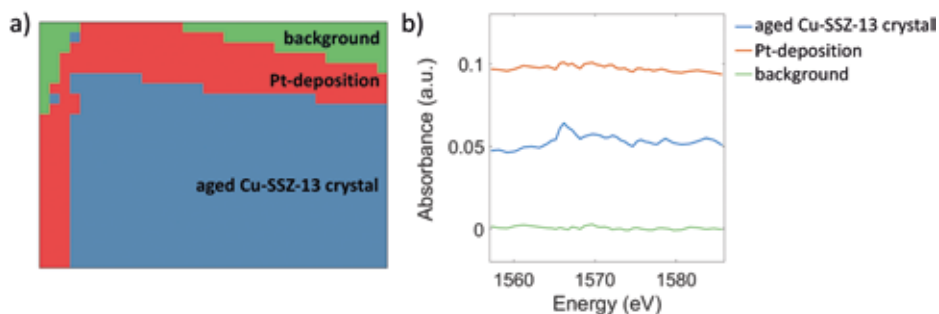

Figure 3.1 a) The background region, sample with and without Pt-deposition regions, were distinguished by Principal Component Analysis (PCA) and k-means Cluster Analysis (CA) on the raw data, i.e., the Optical Density (OD) map of the measured cross section. b) The corresponding Al K-edge X-ray Absorption Near-Edge Structure (XANES) spectra of the three regions under study.

PCA and k-means CA were then performed to group pixels into different clusters based on the similarity of their XANES spectra. According to the Eigenspectra and the scree plot, the first two Principal Components (PCs), which could explain more than 95% of data variance, were chosen. Next, the data was projected onto this 2-dimensional PC space and upon inspection of the resulting score plot classified into three clusters (k=3) via k-means clustering using the average solution of 10 k-means replicates. Using this result as an initial solution the clustering was further refined by an Expectation Maximization (EM) algorithm for Gaussian Mixture Modeling (GMM) to achieve a point density clustering in PC space, which often improves the clustering for noisy XANES data. Al species were determined by LSLC fitting of the XANES of the clusters using the same procedure as for the bulk XANES.

3.3   Results and Discussion

As was mentioned above, the STXM experiments were performed at the Advanced Light Source (ALS, Berkeley, California, USA) beamline 11.02 and the sample preparation and APT experiments were conducted at the Center for Nanophase Materials Sciences (CNMS) at Oak Ridge National Laboratory (ORNL, Oak Ridge, Tennessee, USA). Prior to the STXM experiment, a single crystal of aged zeolite Cu-SSZ-13 was attached to a Mo Omniprobe® Lift-Out Grid (Mo was used to prevent any contamination from a more typical Cu grid), and

thinned to ~0.5 μm using Focused Ion Beam (FIB) milling to allow for sufficient X-ray transmission through the material, as is shown in Figure 3.2.[40] The aged zeolite Cu-SSZ-13 is the same as the one reported in reference[24], with a bulk Si/Al ratio of ~20, and was aged using the industry standard simulation for a 135,000 mile vehicle-aged catalyst.[41] After being mounted on the grid and thinned, the zeolite crystal had an asymmetrical Pt coating deposited on the crystal surface (Figure 3.2e, FIB Pt was deposited on the crystal surface to protect the material during milling), which also served as a marker for the correlated APT-STXM experiments. Careful examination of Figure 3.2f shows that the crystal thickness is not uniform and it is thinner at the top near the Pt strip, which was a consequence of the FIB milling step with the Ga ion source, and the top was thinner as it was more exposed to the Ga ion beam. After the zeolite crystal was mounted at CNMS, it was transferred to ALS for the STXM experiment.
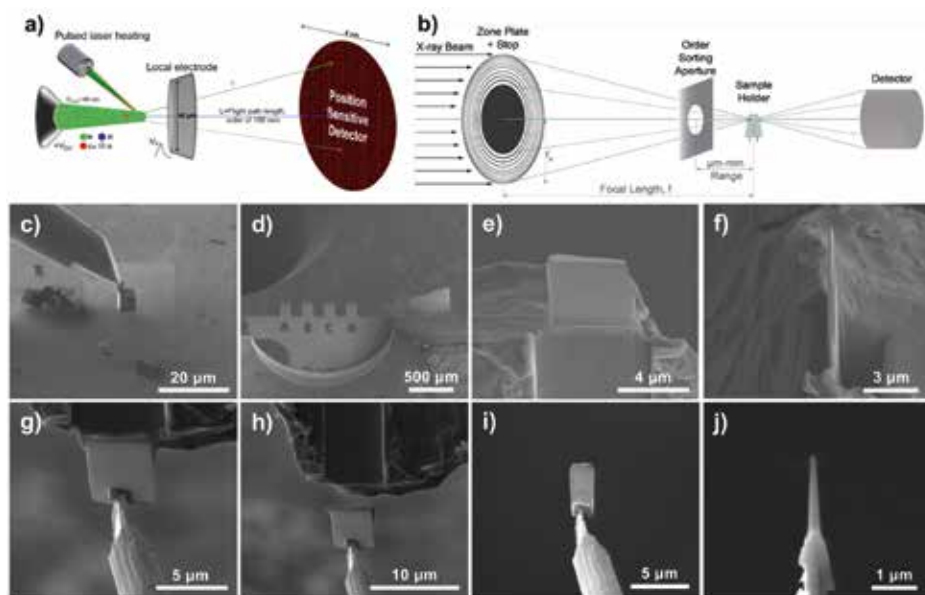
Figure 3.2 Overviews of characterization techniques and sample preparation for Atom Probe Tomography (APT) and Scanning Transmission X-ray Microscopy (STXM). a) Schematic of an APT instrument, including approximate sizes of the various components. b) Schematic of a STXM instrument with the following components: Soft X-ray beam, zone plate (ZP), Order Sorting Aperture (OSA), sample holder and detector. c-f) Picking up a single crystal of zeolite Cu-SSZ-13 using a Kleindiek nanomanipulator and then attaching the crystal to a Mo Omniprobe® Lift-Out Grid and subsequently thinning the crystal to ~0.5 μm using a Ga Focused Ion Beam (FIB) milling after applying a protective Pt layer shown in e. g-j) After the STXM measurements the cross section was attached to the tungsten needle on the Kleindiek nanomanipulator where it is shaped into a needle for the APT experiment.
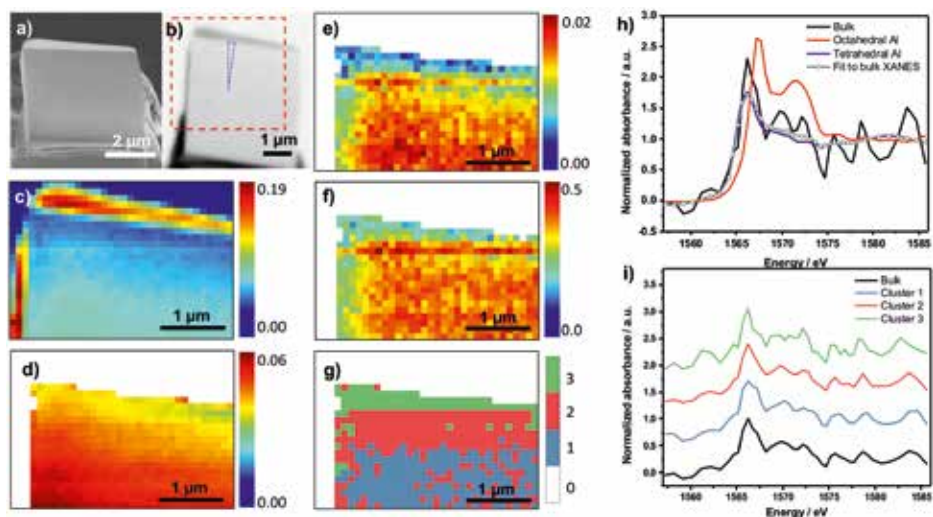
Figure 3.3 a) Scanning Electron Microscopy (SEM) image of the cross section mounted for the Scanning Transmission X-ray Microscopy (STXM) experiment. b) Transmission image of the entire cross section recorded at 1561.0 eV. The red rectangle indicates the scanning area in STXM, which was collected with a Field of View (FOV) of 4×4 μm^2 or 80×80 pixels (pixel size: 50×50 nm^2). The area shown in Figure c-g is part of the scanned region that was designated for STXM-XANES (X-ray Absorption Near-Edge Structure) analysis with a FOV of 3.4×2.4 μm^2 or 34×24 pixels (pixel size 100×100 nm^2, binning 0.5). The blue triangle indicates the approximate location of the Atom Probe Tomography (APT) needle. c) STXM optical density (OD) of the cross section at 1566.2 eV, which was converted from the as-recorded transmission image, showing the maximum absorption contrast. The scale bar indicates the X-ray absorption intensity. d) Average STXM OD of the cross section in pre-edge region after applying a mask to remove all data except those originating from the crystal, showing the thickness difference within the crystal. The scale bar indicates the absorption intensity of X-rays. e) Edge-jump map based on XANES representing Al amount. The scale bar reports the values of the absorption edge jump, defined as the difference between the average intensity value in the XANES post-edge region and the average intensity value in the XANES pre-edge region. f) Thickness-corrected edge jump map based on XANES representing Al concentration. The scale bar indicates the absorption intensity of X-ray. g) The result of segmentation based on PCA and CA of the cross section showing the spatial distribution of the three clusters, with XANES for each cluster in (i). h) Least-Square Linear Combination (LSLC) fitting of XANES spectrum of the bulk employing zeolite ZSM-5 and α-Al_2O_3 as reference materials for tetrahedral Al and octahedral Al, respectively. i) Bulk XANES for the entire cross section along with the XANES for the three clusters isolated by PCA.

The sample cross section was loaded into the STXM instrument, and a transmission image was first recorded at the Al pre-edge energy of 1561.0 eV and compared to the SEM image in Figure 3.3a-b. The STXM measurement was conducted with the soft X-ray beam going through a 45 nm ZP, resulting in a 50×50 nm^2 beam spot size. The Pt deposited to protect the sample during FIB milling is evident in the transmission image due to its stronger absorption

caused by its high density (Figure 3.3b), and the non-symmetrical Pt deposition then acted as a marker for the crystal edge. The bulk XANES from combining all data collected for the cross section is shown in Figure 3.3h along with the references for tetrahedral and octahedral Al, which were zeolite ZSM-5 and α-Al$_2$O$_3$, respectively. The LSLC fitting (Figure 3.3h) shows that the cross section contains ~90% tetrahedral Al (framework) and ~10% octahedral Al (extra-framework). This relatively small proportion of framework Al removal to form octahedral Al is consistent with the results of previous studies, and is also expected from our previous study of this material as described in Chapter 2 and is consistent with the catalyst retaining its activity after aging.[24,42–44]

In the transmission image at 1561.0 eV in Figure 3.3b a pixel size of 50×50 nm^2 was used. For further analysis the transmission image was first converted to display absorption (Figure 3.3c), i.e., the X-ray absorption coefficient. Then, the 52 images of the X-ray energy scans were spatially aligned followed by removal of the region which did not contain zeolite materials, resulting in a 3.4×2.4 µm^2 scan area. Once the XANES of each pixel were examined, it was evident that the absorption was not sufficient to give enough signal for the single pixel X-ray absorption spectra to be meaningfully analyzed. Therefore, the images were binned to combine 4 (2×2) pixels into one. Then there were 34×24 pixels remaining, and after filtering out the region that did not contain zeolite or had Pt deposition using a mask (details in experimental section), 538 pixels remained for analysis. After binning and applying the data mask, the absorption map based on the average absorption in the pre-edge region (1557-1563 eV) is shown in Figure 3.3d. This figure shows that the absorption increases from the top to the bottom of the sample as expected due to the increasing sample thickness; the X-ray absorption in the pre-edge region is a good measure for sample thickness as it is not (or very minimally) influenced by relative changes in Al concentration.

The amount of Al within the cross section was evaluated by studying the absorption edge jump map, as shown in Figure 3.3e. The data in the figure are consistent with a gradient in Al with the lowest amount near the top of the zeolite crystal. At first consideration, this would appear to indicate Al zoning across the cross section. However, closer examination of the side view of the cross section by SEM (Figure 3.2f) shows that the FIB milling used to thin the zeolite crystal left the cross section thinner at the top than the bottom, which is a common occurrence as the milling ion beam source was normal to the top of the zeolite crystal. To exclude the absorption difference due to varying thickness, the edge jump map is divided by the average pre-edge absorption in each pixel to obtain

the thickness-corrected edge jump map, which then shows the Al concentration in each pixel (Figure 3.3f). This figure shows that there is a higher thickness-corrected absorption in the center of crystal compared to both edges, which would mean the Al concentration is lower near the crystal edge (~100-300 nm) than the rest of the crystal. However, we want to further explore this result due to any possible influence of the protective Pt layer applied to the material. Though, it is certainly shown that the Al concentration is homogeneous within the central region of the crystal at the scale of 100×100 nm² pixels that were analyzed, though not in the first ~100-300 nm near the crystal surface.

Table 3.1. Least-Square Linear Combination (LSLC) fitting of Al K-edge X-ray Absorption Near-Edge Structure (XANES) spectra of the bulk and clusters employing zeolite ZSM-5 and α-Al$_2$O$_3$ as references for tetrahedral Al (Al$_{Td}$, framework) and octahedral Al (Al$_{Oh}$, extra-framework) respectively.

	Al$_{Oh}$	+/-	Al$_{Td}$	+/-	R-square	R-factor	Reduced chi-square
Bulk XANES	0.092	0.108	0.908	0.136	0.786	0.036	0.079
Cluster 1	0.159	0.225	0.841	0.284	3.408	0.102	0.341
Cluster 2	0.065	0.110	0.935	0.138	0.812	0.037	0.081
Cluster 3	0.000	0.160	1.000	0.202	1.727	0.147	0.173

As the single pixel XANES is too noisy to provide useful edge energy information, which could be used to distinguish tetrahedral versus octahedral Al, the data was further analyzed using PCA. The influence of sample thickness was excluded in the PCA by using normalized data (edge jump set to one). Furthermore, PCA is conducted without any *a priori* knowledge of the data, so it is an unbiased method of analysis. PCA of the XANES maps indicated two main components, and further *k*-means CA demonstrated three significantly different clusters in the cross section, as shown in Figure 3.3g, with the deconvolutions and resulting amounts of tetrahedral and octahedral Al in each cluster given in Table 3.1. The three clusters have an increasing amount of octahedral Al, from none in Cluster 3, which is near the edge of the crystal, to ~15% octahedral Al near the center. Based on the PCA of the Al it appears that zeolite steaming caused a more significant fraction of framework Al to be removed near the center of the crystal compared to the edge of the crystal. As the thickness corrected edge jump map showed a lower Al concentration near the edge, it may mean that in the Al rich central region the Al was more easily removed from the framework. This nanoscale identification of an increasing amount of framework Al removal with increasing Al concentration is consistent with the general macroscale trend

3

in zeolite catalysts, that materials are less stable to hydrothermal treatment when they have a higher amount of Al, that is, a lower Si/Al ratio.[45]
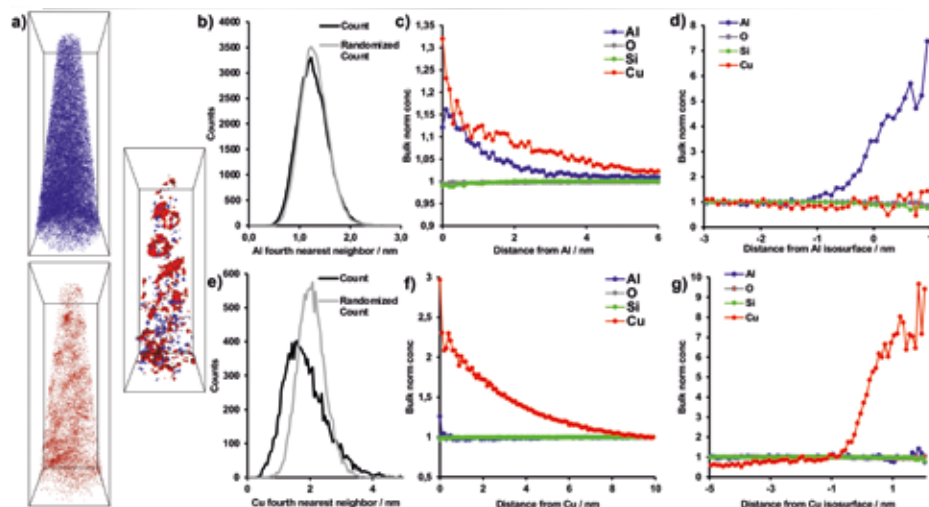
Figure 3.4 Results of the Atom Probe Tomography (APT) experiments and related data analysis. a) Distributions of all Al ions (blue) and all Cu ions (red) as well as 5.6% Al isosurfaces (blue) and 2% Cu isosurfaces (red), bounding box dimensions $143 \times 48 \times 49$ nm^3. b) Al fourth Nearest Neighbor Distribution (4NND). c) Al Radial Distribution Function (RDF). d) Proximity histogram across the 5.6% Al isoconcentration surface shown in (a), with bulk normalized concentrations shown. e) Cu 4NND. f) Cu RDF. g) Proximity histogram across the 2% Cu isoconcentration surface shown in (a), with bulk normalized concentrations shown.

After the successful STXM data collection the lift-out was returned to ORNL's CNMS for the APT experiment. As shown in Figure 3.2, a single needle could be extracted from the cross section, and instead of being attached to a standard, commercially produced Si microtip array, the APT experiment was performed on a tungsten wire that had been sharpened by electropolishing. This is the more traditional method of running APT experiments, and while it is more labor-intensive than using a Si microtip array, the small size of the cross section would have made it difficult to use a microtip array.[35–37] The APT experiment was successful, and 1.3 million ions were collected. This is a sufficient data set for a proper statistical analysis. Views of all Al and Cu atoms are shown in Figure 3.4a, and, as expected from the results described in Chapter 2 and a previous study, the Al distribution appears to be visually heterogeneous.[24] The distributions of Cu and Al were analyzed using the Nearest Neighbor Distributions (NNDs) and Radial Distribution Functions (RDFs), shown in Figure 3.4b-c and Figure 3.4e-f. For the NNDs, the 4th NND is shown as it led to a better separation between

the collected and randomized data, and for Cu there is clearly a non-random distribution, while for Al there appears to be a small difference between the collected and randomized data. The Al RDF (Figure 3.4c) indicates an Al-Al and Al-Cu affinity, consistent with previous findings. Interestingly, in the Cu RDF there is a clear Cu-Cu affinity, but no Cu-Al affinity, and this result contrasts with the two needles we previously studied from this sample. The heterogeneous distributions of both Al and Cu were then analyzed using isosurface analysis, and 2% Cu and 5.6% Al isoconcentration surfaces are shown in Figure 3.4 along with proximity histograms. The proximity histograms indicate Cu-Cu and Al-Al affinity, but not a significant affinity of Cu-Al or Al-Cu. This is similar to what we previously found and is in line with the robust stability of zeolite Cu-SSZ-13, as we have not been able to identify any regions with a composition similar to copper aluminate spinel (i.e., $CuAl_2O_4$), contrasting with what could be quantitatively identified in aged zeolite Cu-ZSM-5.[24] Overall, the APT analysis of this needle gave results consistent with our previous study, except for not finding a significant Cu-Al affinity in the Cu RDF. We do not know if this is due to damage to the material or variations in the material, though we believe the latter is more likely as beam damage generally causes aggregation of chemical elements, which is opposite to our findings here.

To attempt to correlate results of the two nanoscale chemical imaging techniques (i.e., STXM and APT), Figure 3.2h-j shows that the needle was removed from nearer the center of the region measured by STXM, as shown in Figure 3.3a-b. This is the portion of the needle that contained ~15% octahedral Al from the PCA-CA-XANES result. The APT analysis found heterogeneities in the Al distribution, which would be consistent with damage from the material due to steaming. This has been established in studies of pristine and steamed zeolite ZSM-5 crystals, where heterogeneities in the Al distribution were only found by APT after steaming.[21] In the present study the Al distribution is only slightly heterogeneous, consistent with the preserved catalytic activity after the 135,000 mile simulated aging procedure, and the relatively small fraction of octahedral Al identified using STXM.

3.4   Conclusions

The results described show that correlating APT and STXM measurements of zeolite-based catalysts is possible, though it should be clear that it remains technically very challenging. Some of the unique advantages of using this correlated characterization approach are: i) APT can resolve the 3-D location of all chemical elements, but gives no information about their local bonding

environment which can be gained from STXM. ii) Since STXM uses soft X-rays it has been estimated that radiation damage effects are two orders of magnitude lower than for Electron Energy Loss Spectroscopy (EELS) measured in a TEM, another technique capable of giving high spatial resolution spectral information.[15,46,47] As we previously studied this sample, we could compare the results, and did not find evidence of significant damage from the STXM experiment. Some of the disadvantages to this correlated approach are: i) The (current) spot size of STXM used (i.e., 50 nm) is similar to the diameter of the needle measured for APT, making it difficult to find any STXM spatial resolution within an APT needle, though the heterogeneities found using Cluster Analysis (CA) were larger regions, making some correlation possible. ii) Specific to this experiment, zeolite samples need to be > 0.5 μm thick for sufficient X-ray absorption, but this is much larger than the dimensions of a typical APT needle, making spatial correlations difficult because the STXM information gives 2-D maps, so it can be difficult to correlate the two characterization techniques. Therefore, it may be more practical to study a material with a smaller absorption length, which may enable a more meaningful, spatially resolved correlation to be made between the two techniques. This would likely be a dense metal, and it may allow for further results in correlating these techniques and further technical developments. In any case, we have clearly demonstrated that correlative STXM-APT is feasible, opening new directions in nanoscale chemical imaging of functional materials.

Acknowledgements

REFERENCES

1   K. Morgan, J. Touitou, J.-S. Choi, C. Coney, C. Hardacre, J. A. Pihl, C. E. Stere, M.-Y. Kim, C. Stewart, A. Goguet and W. P. Partridge, *ACS Catal.*, 2016, **6**, 1356–1381.

2   A. Urakawa and A. Baiker, *Top. Catal.*, 2009, **52**, 1312–1322.

3   B. M. Weckhuysen, *Angew. Chem. Int. Ed.*, 2009, **48**, 4910–4943.

4   I. L. C. Buurmans and B. M. Weckhuysen, *Nat. Chem.*, 2012, **4**, 873–886.

5   G. Möbus and B. J. Inkson, *Mater. Today*, 2007, **10**, 18–25.

6   E. Mahmoud and R. F. Lobo, *Microporous Mesoporous Mater.*, 2014, **189**, 97–106.

7   Z. Liu, N. Fujita, K. Miyasaka, L. Han, S. M. Stevens, M. Suga, S. Asahina, B. Slater, C. Xiao, Y. Sakamoto, M. W. Anderson, R. Ryoo and O. Terasaki, *Microscopy*, 2013, **62**, 109–146.

8   C. Chmelik and J. Kärger, *Chem. Soc. Rev.*, 2010, **39**, 4864–4884.

9   K. P. F. Janssen, G. de Cremer, R. K. Neely, A. V Kubarev, J. van Loon, J. A. Martens, D. E. de Vos, M. B. J. Roeffaers and J. Hofkens, *Chem. Soc. Rev.*, 2014, **43**, 990–1006.

10 A. Devaraj, D. E. Perea, J. Liu, L. M. Gordon, T. J. Prosa, P. Parikh, D. R. Diercks, S. Meher, R. P. Kolli, Y. S. Meng and S. Thevuthasan, *Int. Mater. Rev.*, 2018, **63**, 68–101.

11 Y. Amouyal and G. Schmitz, *MRS Bull.*, 2016, **41**, 13–18.

12 M. K. Miller, T. F. Kelly, K. Rajan and S. P. Ringer, *Mater. Today*, 2012, **15**, 158–165.

13 T. F. Kelly and D. J. Larson, *MRS Bull.*, 2012, **37**, 150–158.

14 M. K. Miller and R. G. Forbes, *Mater. Charact.*, 2009, **60**, 461–469.

15 F. M. F. de Groot, E. de Smit, M. M. van Schooneveld, L. R. Aramburo and B. M. Weckhuysen, *ChemPhysChem*, 2010, **11**, 951–962.

16 E. de Smit, I. Swart, J. F. Creemer, G. H. Hoveling, M. K. Gilles, T. Tyliszczak, P. J. Kooyman, H. W. Zandbergen, C. Morin, B. M. Weckhuysen and F. M. F. de Groot, *Nature*, 2008, **456**, 222–225.

17 F. Meirer and B. M. Weckhuysen, *Nat. Rev. Mater.*, 2018, **3**, 324–340.

18 J. E. Schmidt, L. Peng, J. D. Poplawsky and B. M. Weckhuysen, *Angew. Chem. Int. Ed.*, 2018, **57**, 10422–10435.

19 D. A. Shapiro, Y. S. Yu, T. Tyliszczak, J. Cabana, R. Celestre, W. Chao, K. Kaznatcheev, A. L. D. Kilcoyne, F. Maia, S. Marchesini, Y. S. Meng, T. Warwick, L. L. Yang and H. A. Padmore, *Nat. Photonics*, 2014, **8**, 765–769.

20 A. M. Wise, J. N. Weker, S. Kalirai, M. Farmand, D. A. Shapiro, F. Meirer and B. M. Weckhuysen, *ACS Catal.*, 2016, **6**, 2178–2181.

21 D. E. Perea, I. Arslan, J. Liu, Z. Ristanović, L. Kovarik, B. W. Arey, J. A. Lercher, S. R. Bare and B. M. Weckhuysen, *Nat. Commun.*, 2015, **6**, 7589.

22 A. Devaraj, M. Vijayakumar, J. Bao, M. F. Guo, M. A. Derewinski, Z. Xu, M. J. Gray, S. Prodinger and K. K. Ramasamy, *Sci. Rep.*, 2016, **6**, 37586.

23 J. E. Schmidt, J. D. Poplawsky, B. Mazumder, Ö. Attila, D. Fu, D. A. M. de Winter, F. Meirer, S. R. Bare and B. M. Weckhuysen, *Angew. Chem. Int. Ed.*, 2016, **55**, 11173–11177.

24 J. E. Schmidt, R. Oord, W. Guo, J. D. Poplawsky and B. M. Weckhuysen, *Nat. Commun.*, 2017, **8**, 1666.

25 L. Kovarik, N. M. Washton, R. Kukkadapu, A. Devaraj, A. Wang, Y. Wang, J. Szanyi, C. H. F. Peden and F. Gao, *ACS Catal.*, 2017, **7**, 2458–2470.

26 L. R. Aramburo, E. De Smit, B. Arstad, M. M. van Schooneveld, L. Sommer, A. Juhin, T. Yokosawa, H. W. Zandbergen, U. Olsbye, F. M. F. de Groot and B. M. Weckhuysen, *Angew. Chem. Int. Ed.*, 2012, **51**, 3616–3619.

27 H. E. van der Bij, L. R. Aramburo, B. Arstad, J. J. Dynes, J. Wang and B. M. Weckhuysen, *ChemPhysChem*, 2014, **15**, 283–292.

28 H. E. van der Bij, F. Meirer, S. Kalirai, J. Wang and B. M. Weckhuysen, *Chem. Eur. J.*, 2014, **20**, 16922–16932.

29 L. R. Aramburo, J. Ruiz-Martínez, L. Sommer, B. Arstad, R. Buitrago-Sierra, A. Sepúlveda-Escribano, H. W. Zandbergen, U. Olsbye, F. M. F. de Groot and B. M. Weckhuysen, *ChemCatChem*, 2013, **5**, 1386–1394.

30 S. Kalirai, P. P. Paalanen, J. Wang, F. Meirer and B. M. Weckhuysen, *Angew. Chem. Int. Ed.*, 2016, **55**, 11134–11138.

31 J. E. Schmidt, L. Peng, A. L. Paioni, H. L. Ehren, W. Guo, B. Mazumder, D. A. Matthijs de Winter, Ö. Attila, D. Fu, A. D. Chowdhury, K. Houben, M. Baldus, J. D. Poplawsky and B. M. Weckhuysen, *J. Am. Chem. Soc.*, 2018, **140**, 9154–9158.

32 N. Jiang, *Reports Prog. Phys.*, 2015, **79**, 16501.

33 H. Bluhm, K. Andersson, T. Araki, K. Benzerara, G. E. Brown, J. J. Dynes, S. Ghosal, M. K. Gilles, H. C. Hansen, J. C. Hemminger, A. P. Hitchcock, G. Ketteler, A. L. D. Kilcoyne, E. Kneedler, J. R. Lawrence, G. G. Leppard, J. Majzlam, B. S. Mun, S. C. B. Myneni, A. Nilsson, H. Ogasawara, D. F. Ogletree, K. Pecher, M. Salmeron, D. K. Shuh, B. Tonner, T. Tyliszczak, T. Warwick and T. H. Yoon, *J. Electron Spectros. Relat. Phenomena*, 2006, **150**, 86–104.

34 A. M. Beale, J. Ruiz-Martinez and B. M. Weckhuysen, in *In-situ Characterization of Heterogeneous Catalysts*, John Wiley & Sons, Hoboken, 2013, pp. 441–473.

35 M. K. Miller, K. F. Russell and G. B. Thompson, *Ultramicroscopy*, 2005, **102**, 287–298.

3

36 M. K. Miller and K. F. Russell,
    Ultramicroscopy, 2007, **107**, 761–766.

37 K. Thompson, D. Lawrence, D. J. Larson,
    J. D. Olson, T. F. Kelly and B. Gorman,
    Ultramicroscopy, 2007, **107**, 131–139.

38 J. D. Poplawsky, J. E. Schmidt, B. Mazumder,
    W. Guo, Ö. Attila, D. Fu, D. A. M. de Winter,
    F. Meirer, S. R. Bare and B. M. Weckhuysen,
    Microsc. Microanal., 2017, **23**, 674–675.

39 Y. Liu, F. Meirer, P. A. Williams, J. Wang,
    J. C. Andrews and P. Pianetta,
    J. Synchrotron Radiat., 2012, **19**, 281–287.

40 S. Calvin, *XAFS for everyone*, CRC Press, Boca
    Raton, 2013.

41 S. J. Schmieg, S. H. Oh, C. H. Kim, D. B. Brown,
    J. H. Lee, C. H. F. Peden and D. H. Kim,
    Catal. Today, 2012, **184**, 252–261.

42 J. H. Kwak, D. Tran, S. D. Burton, J. Szanyi,
    J. H. Lee and C. H. F. Peden,
    J. Catal., 2012, **287**, 203–209.

43 A. Wang, Y. Wang, E. D. Walter, N. M. Washton,
    Y. Guo, G. Lu, C. H. F. Peden and F. Gao,
    Catal. Today, 2019, **320**, 91–99.

44 Y. Zhang, H. Wang and R. Chen,
    RSC Adv., 2015, **5**, 67841–67848.

45 M. Guisnet and F. R. Ribeiro, *Deactivation and
    Regeneration of Zeolite Catalysts*, Imperial
    College Press, London, 2011.

46 T. Warwick, K. Franck, J. B. Kortright, G. Meigs,
    M. Moronne, S. Myneni, E. Rotenberg, S. Seal,
    W. F. Steele, H. Ade, A. Garcia, S. Cerasari,
    J. Denlinger, S. Hayakawa, A. P. Hitchcock,
    T. Tyliszczak, J. Kikuma, E. G. Rightor, H. J. Shin
    and B. P. Tonner, *Rev. Sci. Instrum.*, 1998, **69**,
    2964–2973.

47 E. G. Rightor, A. P. Hitchcock, H. Ade,
    R. D. Leapman, S. G. Urquhart, A. P. Smith,
    G. Mitchell, D. Fischer, H. J. Shin and T. Warwick,
    J. Phys. Chem. B, 1997, **101**, 1950–1960.

Probing the Location and Speciation of Elements in Zeolites
with Correlated Atom Probe Tomography and Scanning Transmission X-Ray Microscopy

3

4

New Insights into the NH$_3$-Selective Catalytic Reduction of NO over Zeolite Cu-ZSM-5 as Revealed by Operando Spectroscopy

*X. Ye, R. Oord, M. Monai, J. E. Schmidt,
T. Chen, F. Meirer, B. M. Weckhuysen,
Catal. Sci. Technol., 2022, **12**, 2589-2603.*

ABSTRACT
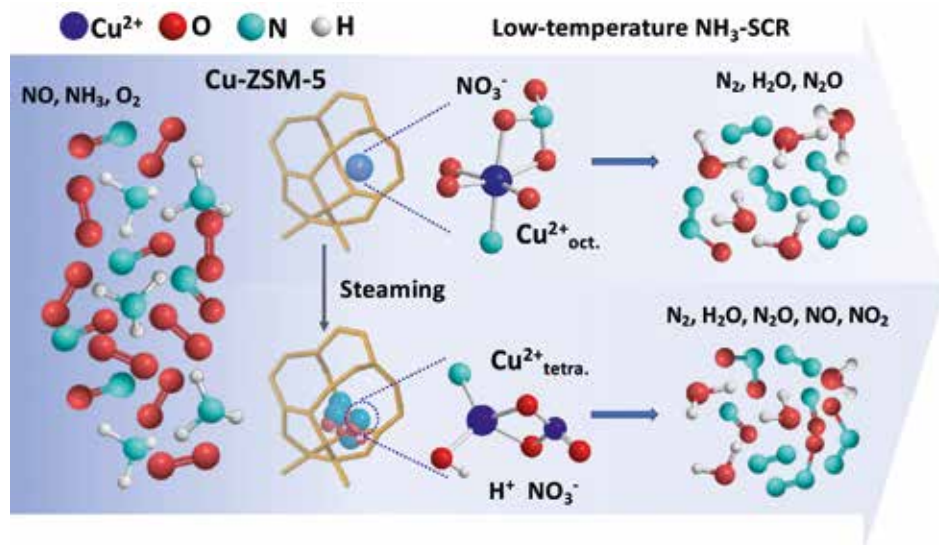
To control diesel vehicle NO_x emissions, Cu-exchanged zeolites have been applied in the Selective Catalytic Reduction (SCR) of NO using NH_3 as reductant. However, the harsh hydrothermal environment of tailpipe conditions causes irreversible catalyst deactivation. The aggregation of isolated Cu^{2+} brings about unselective ammonia oxidation along with the main NH_3-SCR reaction. An unusual 'dip' shaped NO conversion curve was observed in the steamed zeolite Cu-ZSM-5, resulting from the undesired NH_3 oxidation that produced NO. In this Chapter, we gain further insights into the NH_3-SCR reaction and its deactivation by employing operando UV-Vis Diffuse Reflectance Spectroscopy (DRS) and Diffuse Reflectance Infrared Fourier Transform Spectroscopy (DRIFTS) on fresh and steamed Cu-ZSM-5 zeolites. It was found that tetragonally distorted octahedral Cu^{2+} with associated NH_3 preferentially forms during low temperature NH_3-SCR (<250 °C) in fresh zeolite Cu-ZSM-5. The high coordination number of Cu^{2+} ensures the availability for high coverage of nitrate intermediates. Whilst in the steamed Cu-ZSM-5, $[Cu_x(OH)_{2x-1}]^+$ oligomer/clusters in pseudo-tetrahedral symmetry with coordinated NH_3 accumulated during the low-temperature NH_3-SCR reaction. These clusters presented a strong adsorption of surface NH_3 and nitrates/nitric acid at low temperatures and therefore limited the reaction between surface species in the steamed zeolite Cu-ZSM-5. Further release of NH_3 with increased reaction temperature favors unselective NH_3 oxidation that causes the drop of NO conversion at ~300 °C. The structural similarity under the

NH$_3$-SCR reaction and unselective NH$_3$ oxidation confirmed the entanglement of these two reactions above 250 °C. Moreover, competitive adsorption of NH$_3$ and nitrates/nitric acid occurs on shared Lewis-acidic adsorption sites. Prompt removal of surface nitrates/nitric acid by NO avoids the surface blockage and tunes the selectivity by alternating nitrate-nitrite equilibrium. The formation of adsorbed NO$_2$ and HNO$_x$ points to the necessity of an acid adsorbent in practical applications.

4.1   Introduction

Emission control of NO$_x$ (i.e., NO, N$_2$O and NO$_2$) has been mandated in applications such as stationary power plants and diesel engine vehicles. Vanadia-based NH$_3$-Selective Catalytic Reduction (NH$_3$-SCR) catalysts are rather efficient and economical in stationary NO$_x$ abatement, but failed to adapt to diesel vehicles because of the low activity at a high air/fuel-ratio and their high SO$_2$ oxidation activity.[1,2] Considering the dominant emission of NO compared to N$_2$O and NO$_2$ in NO$_x$-lean automotive exhausts, the standard NH$_3$-SCR reaction (4NH$_3$ + 4NO + O$_2$ = 4N$_2$ + 6H$_2$O), where stoichiometrically equal amounts of NH$_3$ as NO are employed, is the main focus in catalyst development.[3] Catalyzing such a redox reaction, involving electron transfer processes, requires a catalyst that can accept and donate electrons when encountering reactant molecules or bind with reaction intermediates. Transition metal-based catalysts are thus promising candidates for NH$_3$-SCR reaction, due to the modifiable electron configuration of their d orbitals.

Since the high NO decomposition activity of a zeolite Cu-ZSM-5 catalyst materials was discovered in 1980s, Cu-exchanged zeolites have been widely investigated for the NH$_3$-SCR reaction.[4] Although Cu-exchanged zeolites exhibit high NH$_3$-SCR activity over a wide temperature window, the automotive industry is still facing the dilemma of choosing a suitable catalyst for commercialization – medium/large pore zeolite structures, such as MFI and BEA, are limited by their low hydrothermal stability, while the more robust small pore zeolite CHA (i.e., SSZ-13 and SAPO-34) has a higher cost. The irreversible hydrothermal aging of zeolites is a subtle yet permanent process, during which the functional moieties in Cu-exchanged zeolites undergo a dynamic transformation starting from local distortion of the structural unit regardless of the type of zeolite framework. The deactivation of catalysts should be particularly considered for the rational design of emission control systems for vehicle tailpipes.

The ideal Cu species in Cu-exchanged zeolites are isolated Cu^{2+} balanced by an Al pair and $[CuOH]^+$ balance by a single Al site. When the Cu-exchanged zeolites undergo hydrothermal treatment or experience a deactivation process, the degradation of Cu increases the heterogeneity of Cu species. The Cu_xO_y clusters/nanoparticles, spinel phase $CuAl_2O_4$, as well as $Cu(OH)_2$ can form and are considered to be detrimental for the standard NH_3-SCR reaction.[5–9] Various Cu species in the zeolites provide multiple possible sites for catalytic reactions at NH_3-SCR reaction conditions. Undesired byproducts, for instance NO_2 and N_2O, can be selectively formed during the NH_3-SCR reaction.[10] Additionally, with multiple evolutionary Cu species in the Cu-exchanged zeolites, the unwanted side reactions such as NO oxidation ($2NO + O_2 = 2NO_2$) and unselective NH_3 oxidation to NO ($4NH_3 + 5O_2 = 4NO + 6H_2O$) can also take place under standard NH_3-SCR reaction conditions.[11–14]

In a previous study of steamed Cu-ZSM-5 zeolites we have observed an unusual NO conversion curve with a 'dip' shape at around 300 °C.[15] A similar drop of NO conversion was reported at ~270 °C with the hydrothermally treated zeolite Cu-SSZ-13 and was simply explained by the accelerated unselective NH_3 oxidation promoted by Cu_xO_y clusters/nanoparticles.[16,17] However, the detailed structural reasons for the low NH_3-SCR activity have not yet been well understood due to the interference of multiple Cu sites and side reactions.

In this Chapter, the catalytic performance and structural properties of a series of fresh and steamed Cu-ZSM-5 zeolites were investigated for a more complete understanding of NH_3-SCR catalysis. Cu-exchanged zeolites were treated by high temperature steam to mimic different aging severities. Operando UV-Vis Diffuse Reflectance Spectroscopy (DRS) and Diffuse Reflectance Infrared Fourier Transform Spectroscopy (DRIFTS) were conducted to gain mechanistic insight into the NH_3-SCR reaction and its deactivation, to gain a deeper understanding of the unusual catalytic behavior of the steamed zeolite Cu-ZSM-5 material. The dynamic of local structural changes of the Cu^{2+} site under reaction conditions were followed by operando UV-Vis DRS, specifically by interpretation of the ligand-to-metal charge transfer (LMCT) as well as the d-d transition bands based on crystal field theory. The behaviour of adsorbed species, including chemisorbed NH_3 and nitrates/nitric acid, were investigated utilizing their development and consumption under various reaction conditions. Finally, the 'dip'-shaped NO conversion curve (Figure 4.2a) could be explained by the side reaction of unselective NH_3 oxidation, which is structurally ascribed to the possible formation of $[Cu_x(OH)_{2x-1}]^+$ oligomers/clusters with a pseudo-tetrahedral

Cu^{2+} center coordinated with NH_3 in the steamed Cu-ZSM-5 material. The slow rate of surface reaction between adsorbed NH_3 and surface nitrites/nitrates or nitric/nitrous acid limits the low-temperature NH_3-SCR.

4.2   Experimental Section

4.2.1   Catalyst Preparation

The parent zeolite NH_4^+-ZSM-5 was purchased from Zeolyst (CBV 2314, Lot 2200-89), with a specified Si/Al ratio of 11.5. Zeolite ZSM-5 in its proton form was obtained by static calcination in air at 550 °C before ion-exchange with Cu(II) acetate. 1 g H-ZSM-5 was suspended in 250 mL 10 mM Cu(II) acetate (Sigma-Aldrich, ≥98%) solution and stirred at room temperature for 24 h, followed by washing with a large excess of demineralized water. After drying, the zeolite was then calcined in air at 550 °C to remove the residual salt and was labelled as Cu-ZSM-5-fresh. The above-mentioned calcination procedures are identical. The zeolites were dehydrated at 150 °C for 1 h before 550 °C calcination for 4 h with a ramping rate of 2 °C/min in both heating and cooling process. The steaming procedure was modified based on our previous research[15]. The 10 % steam in air flow was produced by using a H_2O bubbler at 47 °C and was directed to the fresh zeolite Cu-ZSM-5 in a porcelain boat-shaped crucible in a tube furnace at 120 °C to prevent H_2O condensation. The steaming procedure was conducted at different temperature (650, 700, 750 or 850 °C) using a ramping rate of 2°C/min and dwell time of 16 h. The steamed Cu-exchanged zeolites ZSM-5 were then cooled down to room temperature in dry air.

4.2.2   Catalyst Characterization

Inductively Coupled Plasma-Optical Emission Spectroscopy (ICP-OES) was measured using a PerkinElmer Avio® 500 ICP-OES instrument at GeoLab, Utrecht University. Fresh/steamed Cu-exchanged zeolites ZSM-5 were treated with lithium borate fusion. The lithium borate fusion bead was dissolved in a 2N HNO_3 solution for ICP-OES measurement. A comparable level of Cu content (2.4 wt %) was determined in the fresh and steamed zeolites Cu-ZSM-5.

X-ray Diffraction (XRD) patterns of the fresh/steamed Cu-exchanged ZSM-5 zeolite materials were collected by a Bruker D2 Phaser with a cobalt radiation X-ray source (Co k_α = 1.789 Å). Powdered samples were pressed on the sample holder and rotated at 15 revolutions/min during measurement.

Transmission Electron Microscopy (TEM) was performed in a JEM-2800 microscope (JEOL) and operated under 200 keV. Powder samples were dispersed in ethanol and then deposited on gold TEM grids with holey carbon film.

Ammonia Temperature-Programmed Desorption (NH_3-TPD) was taken on Micromeritics Autochem II 2920 equipped with a Thermal Conductivity Detector (TCD). Typically, 60 mg fresh/steamed zeolite Cu-ZSM-5 was first dehydrated in He flow for 1 h at 600 °C with a heating ramp of 10 °C/min. Ammonia then flowed pass the sample at 100 °C, followed by flushing with He at 100 °C for 2 h. The TCD signal of ammonia desorption was recorded starting from 150 °C under a temperature ramping rate of 5°C/min in a 25 mL min^{-1} He flow and staying at 600 °C for 30 min.

CO adsorbed Fourier Transform Infrared (FT-IR) spectroscopy was carried out on a Perkin Elmer 2000 FT-IR spectrometer equipped with a homemade transmission cell with CaF_2 window. A 10 mg sample was used to make the self-supported pellet for both catalysts. For each experiment, the self-supported pellet was dehydrated at 300 C for 2 h under vacuum of 10^{-6} mbar, followed by cooling down with liquid nitrogen. The reference spectrum was taken before dosing CO. The 10% CO/He (Linde, 99.998 %) was dosed in gradience to attain different surface coverage of CO. Spectra were recorded after CO dosage each time in a resolution of 4 cm^{-1} with 16 replications.

4.2.3   Catalytic Testing

Catalyst testing was performed in a fixed bed plug flow setup. All the required gases were provided by Linde and the flow rates of feed gases were controlled by Brooks flow meters. Typically, 50 mg sieved catalysts powders (0.125-0.425 mm) were closely packed in a quartz reactor. Prior to the NH_3-SCR reaction, NH_3 oxidation or NO oxidation reaction, the packed zeolite was activated in 5 % O_2/ He at 550 °C for 1 h and was cooled to 150 °C to start the reaction.

For the standard NH_3-SCR reaction, the catalyst was exposed to SCR feed composition of 1000 ppm NO, 1000 ppm NH_3 and 5% O_2 balanced by He with a Gas Hourly Space Velocity (GHSV) of 100,000 h^{-1}. The reaction was conducted in a desired temperature from 150 to 450 °C and was stabilized for 1 hour at each target temperature. The gas composition from outlet was determined by a FT-IR gas analyzer (Perkin–Elmer, Spectrum Two) that the real-time concentration of reactants (i.e., NO and NH_3) and products (NO_2 and N_2O) could be recorded. After the reaction reach the steady state, the average concentration of outlet

gas composition was used to determine conversion and yield at each reaction temperature. The production of N$_2$ was calculated based on N balance assuming that only gaseous products (NO$_2$, N$_2$O, N$_2$) were formed in the reaction.

$$NO\ conversion\ (\%) = \frac{[NO_{in}] - [NO_{out}]}{[NO_{in}]} \times 100\ \%$$ (Eq. 4.1)

$$NH_3\ conversion\ (\%) = \frac{[NH_{3\ in}] - [NH_{3\ out}]}{[NH_{3\ in}]} \times 100\ \%$$ (Eq. 4.2)

$$Yield\ (\%) = \frac{[Product]}{[NO_{in}]} \times 100\ \%$$ (Eq. 4.3)

For a better understanding of catalytic behavior of NH$_3$-SCR from the sense of side reactions, ammonia oxidation reaction and nitric oxide reaction were also performed over zeolite Cu-ZSM-5-fresh and Cu-ZSM-5-850stm. The reaction processes and the conversion calculations of NH$_3$ oxidation as well as NO oxidation were the same as the NH$_3$-SCR reaction except for the compositions of gas feed. The gas feed composition was 1000 ppm NH$_3$ and 5 % O$_2$ balanced by He for the NH$_3$ oxidation, and 1000 ppm NO and 5% O$_2$ balanced by He for the NO oxidation with a Gas Hourly Space Velocity (GHSV) of 100,000 h^{-1}.Operando UV-Vis Diffuse Reflectance Spectroscopy (DRS) was also performed during the catalyst testing and achieved by the specially designed quartz fixed-bed reactor with a UV-Vis transparent window. A high-temperature UV-vis optical fiber probe connected to an AvaSpec 2048L spectrometer was employed to collect the UV-Vis DRS spectra every 2 min.

The Principal Component Analysis (PCA) was conducted on the d-d transition band of operando UV-Vis diffuse reflectance spectra. The first three principal components separate well the low, medium, and high wavenumber bands, from where the band positions can be determined accurately for the subsequent Gaussian fitting of each spectrum of the series. (Figure 4.1a-b). Three Gaussian peaks were restrained to the regions 10200-10800 cm^{-1}, 13000-14000 cm^{-1} and 16000-18000 cm^{-1} respectively. Moreover, the peak width was confined based on the initial fitting result of reference spectrum (UV-Vis spectrum of fresh zeolite Cu-ZSM-5 in Helium at 150 °C). All the spectra were fitted using the same fitting parameters. The R square of fit reached the level of 0.9999 for every fitted spectrum. The fitting curves and individual fitted components of fresh and 850 °C steamed zeolites Cu-ZSM-5 shows the reliability of fitting (Figure AIII3-4).

4
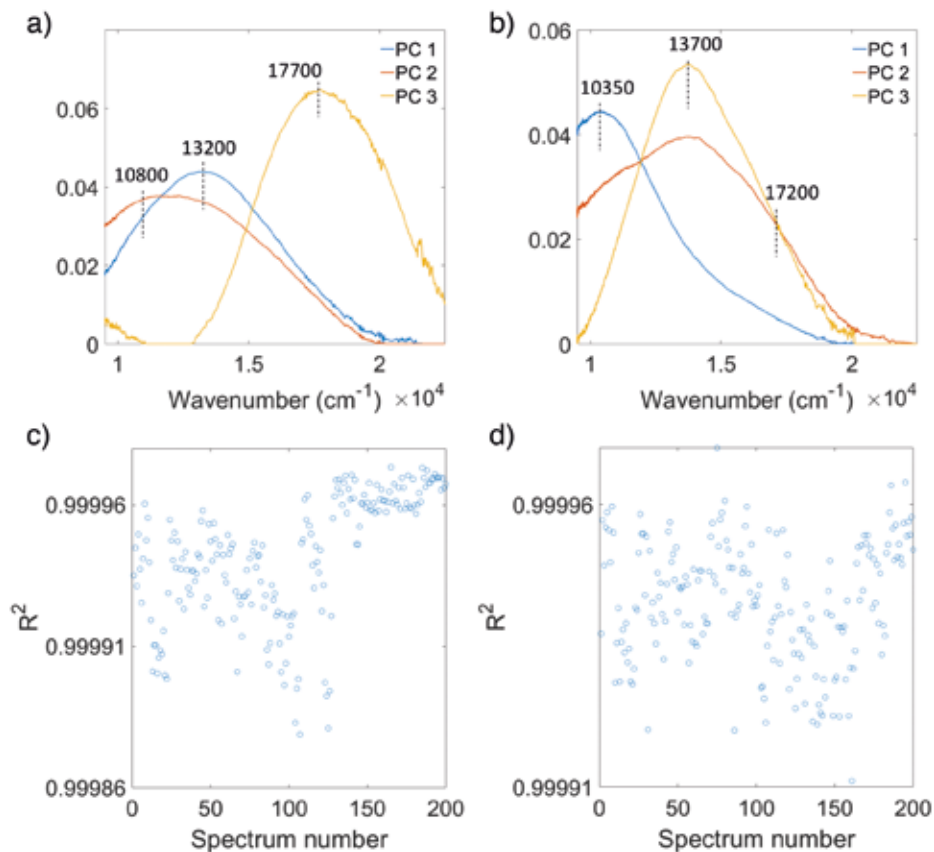
Figure 4.1 Principal Component Analysis (PCA) results of the operando UV-Vis Diffuse Reflectance Spectroscopy (DRS) data of a) fresh and b) 850 °C steamed Cu-ZSM-5. The goodness of fit in terms of R square of the fitted d-d transition band in all fitted spectra obtained during NH_3-Selective Catalytic Reduction (SCR) reaction performed on c) fresh and d) 850 °C steamed zeolite Cu-ZSM-5.

4.2.4 Operando Diffuse Reflectance Infrared Fourier Transform Spectroscopy

Operando Diffuse Reflectance Infrared Fourier Transform Spectroscopy (DRIFTS) was performed making use of 10-20 mg catalyst, which was loaded in a sample holder in a high temperature Harrick reaction chamber with ZnSe windows and was pressed into a pellet with flat surface. The reactant gases were flowed through the pellet from bottom to top. Samples were calcined in 5 % O_2/He at 550 °C before the reaction. The gas feed composition and reaction procedure were the same as the catalytic test on a fix bed reactor when performing the NH_3-SCR reaction. NO or NH_3 cutoff experiment was also performed at 250 °C. The DRIFTS experiment protocol is briefly illustrated in Figure 4.11a. The DRIFTS data were collected continuously by a Bruker Tensor II spectrometer

with a Mercury-Cadmium-Telluride (MCT) detector with 32 accumulation times and resolution of 4 cm^{-1}. The effluent gas composition was determined by a FT-IR gas analyzer (Perkin–Elmer, Spectrum Two).

4.3   Results and Discussion

4.3.1   Catalytic Performance
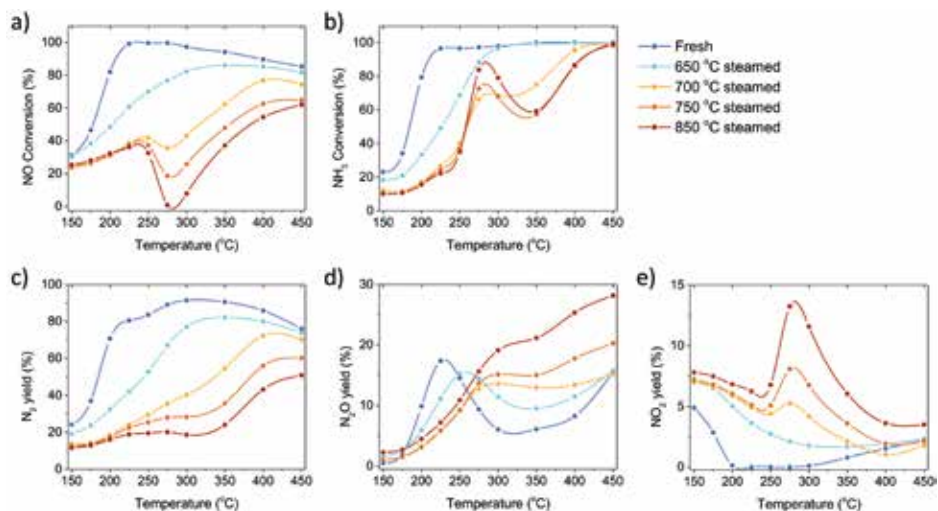
Figure 4.2 a) NO conversion, b) NH$_3$ conversion, c) N$_2$ yield, d) N$_2$O yield and e) NO$_2$ yield of the standard NH$_3$-Selective Catalytic Reduction (SCR) reaction performed on fresh and steamed Cu-ZSM-5 zeolites. The standard NH$_3$-SCR reaction was conducted with a Gas Hourly Space Velocity (GHSV) of 100,000 h^{-1} with 1000 ppm NO, 1000 ppm NH$_3$, 5% O$_2$ and balanced with He.

The fresh zeolite Cu-ZSM-5 underwent a steaming pre-treatment to simulate the working catalysts after various degrees of deactivation. The standard NH$_3$-SCR reaction was performed on fresh and steamed Cu-ZSM-5 catalysts in the temperature range from 150 to 450 °C (Figure 4.2). A varying extent of deactivation of NH$_3$-SCR activity was observed in the steamed zeolites Cu-ZSM-5. The fresh Cu-ZSM-5 showed the highest NO conversion and N$_2$ selectivity in the whole temperature range. The steaming process mainly caused the loss of NO conversion at low reaction temperature. It is notable that unusual catalytic behavior was observed over the zeolites that underwent the 700-850 °C steaming pre-treatment. The NO conversion had a drop starting at 250 °C followed by a continuous increase in conversion from 300 °C, exhibiting a distinct valley-shaped NO conversion curve. Meanwhile, a peak was observed in the NH$_3$ conversion curve at the exact temperature of the observed 'dip' in NO conversion.

This points to the non-equivalent consumption of NO and NH_3 in the reaction, which contradicts the identical stoichiometric ratio of NO and NH_3 in a standard NH_3-SCR reaction.
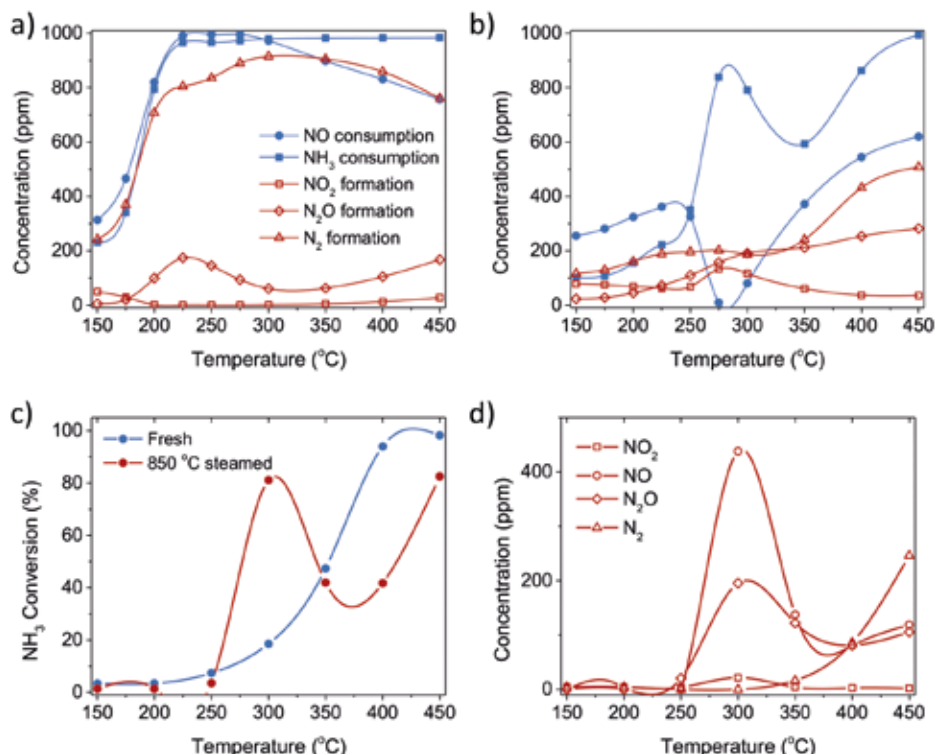
Figure 4.3 The reactants consumption and products formation in standard NH_3-Selective Catalytic Reaction (SCR) reaction over a) fresh and b) 850 °C steamed Cu-ZSM-5. c) The conversion of NH_3 during the NH_3 oxidation reaction over the fresh and steamed Cu-exchanged ZSM-5. d) Product concentration from the NH_3 oxidation reaction over 850 °C steamed Cu-ZSM-5. The standard NH_3-SCR reaction was conducted with a Gas Hourly Space Velocity (GHSV) of 100,000 h^{-1} with 1000 ppm NO, 1000 ppm NH_3, 5% O_2 and balanced with He. The NH_3 oxidation reaction was conducted with a GHSV of 100,000 h^{-1} with 1000 ppm NH_3, 5% O_2 and balanced with He.

The conversion and formation of nitrogen-containing compounds in the NH_3-SCR reaction over fresh and 850 °C steamed Cu-ZSM-5 zeolites are shown in Figure 4.3a-b. From the consumption difference between NO and NH_3, depicted by blue curves, the occurrence of side reactions such as NO or NH_3 oxidation in standard NH_3-SCR could be determined. In fresh Cu-ZSM-5, NH_3-SCR was the favored reaction, and was only slightly affected by NO oxidation below 200 °C and by NH_3 oxidation above 300 °C. In contrast, side reactions had more

significant impact on the steamed Cu-ZSM-5. This 'critical temperature' of 250 °C divides the temperature range into a low- and a high- temperature regime. When the reaction temperature was below 250 °C, the converted NO was overall higher than the converted NH$_3$, which implied the involvement of undesirable NO oxidation, confirmed by the additional production of NO$_2$. NH$_3$ oxidation hardly contributed to the low temperature regime, proven by no conversion of NH$_3$ in the NH$_3$ oxidation reaction (Figure 4.3c).

When the reaction temperature was higher than 250 °C, the consumption of NH$_3$ overtook NO consumption, suggesting the involvement of NH$_3$ oxidation along with the standard NH$_3$-SCR reaction, especially in the intermediate reaction temperature range of 250-300 °C. Interestingly, the performance of NH$_3$ oxidation over the steamed Cu-ZSM-5, in that NH$_3$ showed a peak-shape conversion curve with NO as the dominant product (Figure 4.3c-d), is explained as the apparent NO conversion dropped to near 0 % along with the soaring NH$_3$ conversion from 250-300 °C observed in the NH$_3$-SCR reaction. The produced NO from the NH$_3$ oxidation replenished the consumed NO from NH$_3$-SCR, and consequently led to the apparent drop in NO conversion from 250 °C in standard NH$_3$-SCR (Figure 4.2a). In return, the residual NH$_3$ was insufficient for the reduction of the surplus NO, deteriorating the catalytic activation. As for the N$_2$O byproduct, it is formed in the NH$_3$-SCR reaction as a partially reduced product of NO through the formation of HNO intermediate.[18] N$_2$O can also be the product of unselective oxidation of NH$_3$ ($2NH_3 + 2O_2 = N_2O + 3H_2O$). At low reaction temperature, the activity of NH$_3$-SCR reaction was high on fresh Cu-ZSM-5, resulting higher N$_2$O yield compared to the 850 °C steamed Cu-ZSM-5. With elevated reaction temperatures, the N$_2$O was generated from both NH$_3$-SCR and NH$_3$ oxidation reaction and kept increasing.

Although the side reaction of unselective NH$_3$ oxidation explained the 'dip' shape in the NO conversion curve during the NH$_3$-SCR reaction, it put forward another puzzle for NH$_3$ oxidation conducted over steamed zeolite Cu-ZSM-5, where a peak was observed in the NH$_3$ conversion curve at around 300 °C (Figure 4.3c). A possible interpretation can be found from a kinetic model of NH$_3$ oxidation over Cu-exchanged zeolite Cu-SSZ-13. The reaction at 250-400 °C occurs on Cu-exchanged sites but the NH$_3$ conversion decreases with the lower NH$_3$ coverage with increasing reaction temperature, while the high temperature reaction (> 400 °C) starts to take place on the over-exchanged sites, for instance the Cu$_x$O$_y$ species achieving high conversion at elevated temperature.[19]

4.3.2 Changes of Structure Properties upon Steaming

4.3.2.1 Local Damage of the Framework Structure

According to the above observed NH_3-SCR catalytic performance over the fresh and steamed Cu-ZSM-5 zeolites, multiple entangled side reactions present at standard NH_3-SCR reaction condition, in agreement with the results from previous studies.[8,20,21]
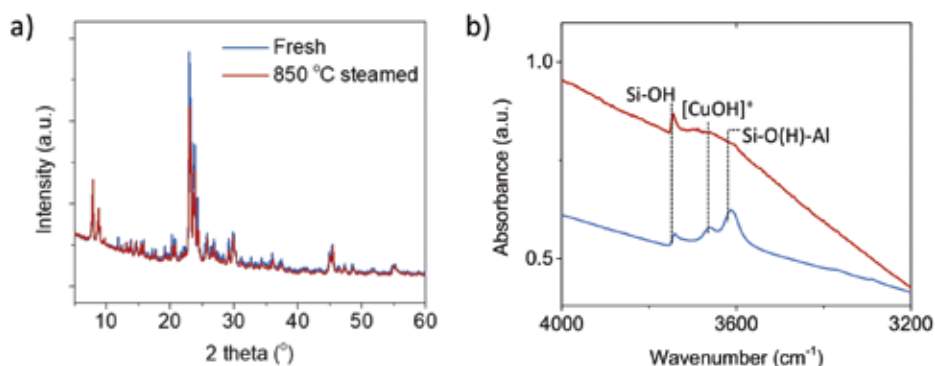
**Figure 4.4** a) X-Ray Diffraction (XRD) patterns and b) OH stretching region in the Fourier Transform Infrared (FT-IR) spectra of fresh and 850 °C steamed zeolite Cu-ZSM-5.

The fresh Cu-ZSM-5 achieved a more stable NO conversion over a wide temperature range, whilst the steamed Cu-ZSM-5 performance was significantly hindered by side reactions throughout the whole temperature range with particularly distinct catalytic performance below 300 °C. Finding the structural reasons behind this complex behavior was essential for a better understanding of the functions and deactivation of active moieties within Cu-ZSM-5. The zeolite framework is regarded as host for the guest cation through the interaction between the opposite charges of framework $[AlO_4]^-$ and isolated $Cu^{2+}/[CuOH]^+$. The steaming pretreatment led to loss of zeolite framework crystallinity, revealed by the lower intensity of the diffraction pattern of MFI zeolite (Figure 4.4a). This is consistent with the expected partial dealumination due to steaming. Although destruction of the long-range order in Cu-ZSM-5 was not observed, it is clearly shown in the FT-IR spectra in the range of the OH stretching vibration (Figure 4.4b) that the well-resolved $[CuOH]^+$ (3660 cm^{-1}) and Brønsted acid sites (3612 cm^{-1}) were replaced by a broad peak representing internal silanol groups in the severely steamed Cu-ZSM-5.[22] The loss of the Brønsted acid sites upon steaming was an indicator of the formation of local defects within the zeolites, resulting in the heterogeneity of hydroxyl groups, which is experimentally

evidenced by the transformation of geometric structure of Al from tetrahedral to octahedral via solid-state Nuclear Magnetic Resonance (ssNMR) and X-ray Absorption Spectroscopy (XAS).[22,23]

### 4.3.2.2 Loss of Isolated Cu^{2+} Sites

Another important functional moiety in fresh zeolite Cu-ZSM-5 is the isolated, exchanged Cu^{2+} sites located near framework Al for charge compensation. The most direct observation of structural changes upon steaming is the formation of Cu-based nanoparticles as shown in the TEM images (Figure 4.5). With increasing steaming temperature, the nanoparticles were more evident throughout the whole zeolite particles. In the 850 °C steamed Cu-ZSM-5, nanoparticles with particle sizes of 2-5 nm were prone to migrate and aggregate on the surface of zeolite particle, which is in agreement with a Scanning Transmission X-ray Microscopy (STXM) study that revealed Cu zoning on the edge of individual catalyst particles in steamed zeolites.[15]
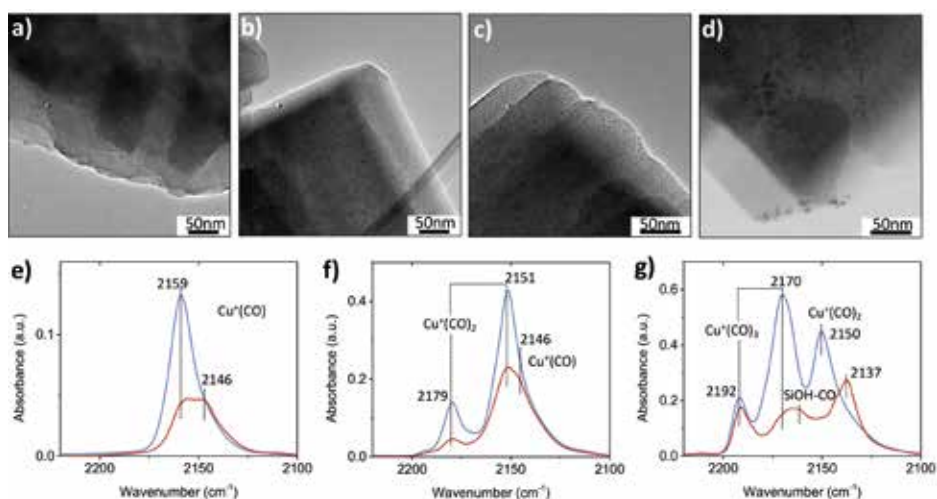
Figure 4.5 Transmission Electron Microscopy (TEM) images of a) fresh, b) 650 °C steamed and c-d) 850 °C steamed zeolite Cu-ZSM-5 in bright field. The CO-adsorbed Fourier Transform Infrared (FT-IR) spectra of fresh and 850 °C steamed zeolites Cu-ZSM-5 under CO pressure of e) 0.015 mBar, f) 0.1 mBar and g) 0.5 mBar at liquid N$_2$ temperature. Blue and red lines represent fresh and 850 °C steamed zeolite Cu-ZSM-5, respectively.

CO is a universal probe molecule in FT-IR spectroscopy experiments to detect the metal sites by charge donation/back-donation between metal center and CO molecule. The interaction of CO with Cu^{2+} is weak, and therefore only Cu$^+$ and the hydroxyl group could be probed by CO in Cu-zeolites.[24] Figure 4.5e-g

shows the FT-IR spectra with different CO coverages. One of the differences between fresh and steamed Cu-ZSM-5 in CO-adsorbed FT-IR spectra is the stronger peak intensities found in the fresh Cu-ZSM-5, indicating larger numbers of available sites for CO adsorption in the fresh catalyst. The adsorption band of cuprous mono-carbonyls adducts centered at 2159 cm^{-1} coordinated up to three CO molecules with increasing CO pressure, which is well-documented.[25] This probed Cu$^+$ originated from [CuOH]$^+$, which experienced auto-reduction during the dehydration pre-treatment under high vacuum.[26] The loss of [CuOH]$^+$ was confirmed in the steamed Cu-ZSM-5 in CO-adsorbed FT-IR spectroscopy, and it was accompanied by the co-existence of another cuprous site coordinated with CO with a lower C-O frequency of 2146 cm^{-1}, which was also reported in zeolite Cu-ZSM-5 with high Cu-exchanged level.[27] This cuprous site had less available coordination sites for ligands since only the mono-carbonyl was observed. When the CO dosage was high, the CO adsorption on the silanol became detectable only on the steamed catalyst,[28] consistent with the observation of abundant internal silanol groups in the 850 °C steamed zeolite Cu-ZSM-5.
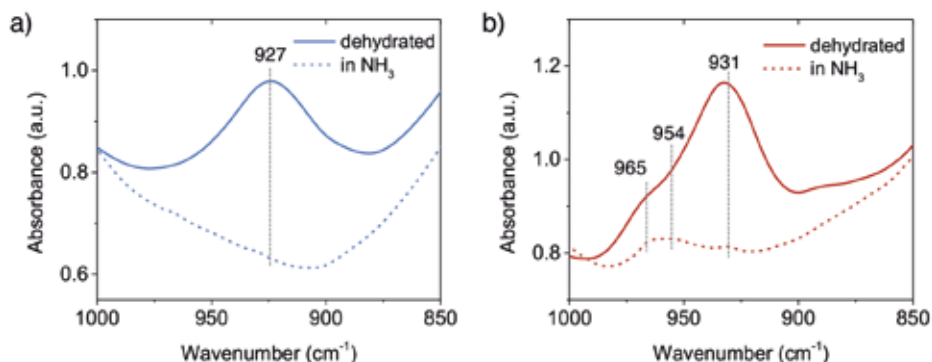
Figure 4.6 Diffuse Reflectance Infrared Fourier Transform Spectroscopy (DRIFTS) data of perturbed framework T-O-T vibration of a) fresh and b) 850 °C steamed Cu-ZSM-5 after dehydration and ammoniation.

The perturbed framework T-O-T vibration is directly influenced by the interaction between the Cu ions and the framework. Figure 4.6 shows the perturbed framework vibration of fresh and 850 °C steamed Cu-ZSM-5 after dehydration and subsequent NH$_3$ treatment. The background spectrum was recorded for the hydrated form of zeolites as fully hydrated Cu^{2+} is mobile.[29] Similarly, the ammoniated Cu^{2+} hardly interacts with the zeolite framework, showing no perturbed T-O-T band. Upon removal of H$_2$O or NH$_3$, the Cu^{2+} is stabilized by the framework oxygen and consequently perturbs framework T-O-T

vibration. The perturbance of the framework generally depends on the charge of the interacting cation such that the higher the net charge of the interacting cation, the lower is the value of the T-O-T vibration, because a stronger interaction between opposite charges weakens the original framework vibration to a greater extent.[30] The transformation from the framework stabilized Cu$^+$ to Cu^{2+} causes the band shift of the asymmetric T-O-T vibration from 970 to 910 cm^{-1} in Cu-ZSM-5.[31,32] The ~930 cm^{-1} and ~950 cm^{-1} bands have been assigned to bare Cu^{2+} and [CuO]$^+$/[CuOH]$^+$/O$_2$-associated Cu$^+$, respectively.[30,33] In the fresh zeolite Cu-ZSM-5, [CuOH]$^+$ was not shown in the perturbed framework vibration band, although its existence was clearly indicated by the CO-FTIR results and its OH stretching band at 3660 cm^{-1}. The signal from the [CuOH]$^+$ perturbance might be covered by the strong and broad band originating from bare Cu^{2+}. However, in addition to the Cu^{2+} and Cu$^+$ perturbed vibrations, the ammoniation process unveiled the 954 cm^{-1} band in the 850 °C steamed Cu-ZSM-5 although it lost the isolated [CuOH]$^+$. Only the isolated or clustered Cu ions can influence the perturbed framework vibration by ligand removal or addition, because interaction between large particles and zeolite framework could be hardly affected by replacement of ligands. The 954 cm^{-1} band is hereby supposed relative to the charged Cu oligomers/clusters [Cu$_x$(OH)$_{2x-1}$]$^+$ that could interfere with the framework vibrations. The adjacency of the hydroxyl group to the Cu^{2+} is later implied by operando DRIFTS results.

Both NO oxidation and NH$_3$ oxidation have been under investigation in Cu-exchanged zeolites suggesting the potential contribution of isolated sites, such as Cu^{2+} and [CuOH]$^+$, to the side reactions observed in the catalytic test.[14,21,34] However, with the steaming-induced local damage of the zeolite framework and the plausible formation of [Cu$_x$(OH)$_{2x-1}$]$^+$ oligomers/clusters, the NO conversion above 250 °C dropped due to the large contribution from unselective NH$_3$ oxidation. The detrimental effect of Cu$_x$O$_y$ clusters/nanoparticles on the NH$_3$-SCR reaction has been demonstrated to promote NH$_3$ oxidation reaction, and promising NH$_3$ conversion was even observed over a physical mixture of CuO and H-SAPO-34.[17,20,35]

4.3.3 Cu^{2+} Dynamics Unraveled by Operando UV-Vis Diffuse Reflectance Spectroscopy

The Cu aggregation in the steamed Cu-ZSM-5 zeolites was proposed to be responsible for the occurrence of the unselective NH$_3$ oxidation reaction that caused the unusual NO and NH$_3$ conversion in NH$_3$-SCR reaction. However, a more detailed structural correlation of the deactivated component contributions

to the loss of NH_3-SCR activity and the promotion of undesired unselective NH_3 oxidation has not yet been well-understood. This requires real-time monitoring of the catalysts in a reaction to establish the structure-activity relationships for further understanding of the key structure involved in the reaction. One of the most facile approaches to study transition metals under working conditions is UV-Vis DRS employing a high temperature UV-Vis optical fiber probe.[36]

4.3.3.1 Replacement of Ligands in Cu²⁺ Complex
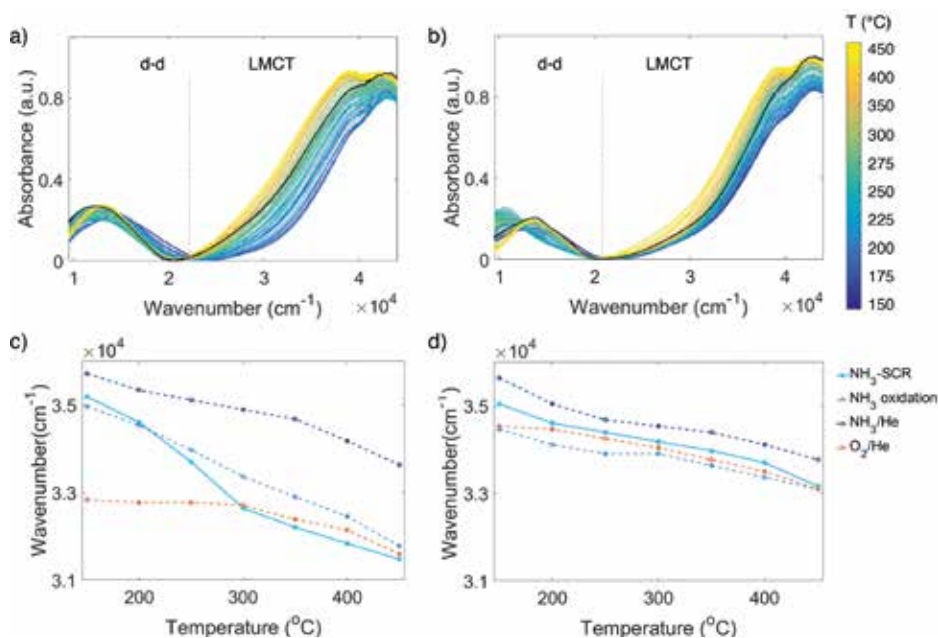
Figure 4.7 Operando UV-Vis Diffuse Reflectance Spectroscopy (DRS) data of the a) fresh and b) 850 °C steamed zeolites Cu-ZSM-5 during NH_3-Selective Catalytic Reduction (SCR) reaction of NO. The black solid line is the spectrum recorded at 150 °C in O_2/He before the reactants were fed. The wavenumber of half height of the LMCT (Ligand-Metal Charge Transfer) band at *ca.* 39000 cm⁻¹ in different reaction conditions was obtained at steady state for c) fresh and d) 850 °C steamed zeolite Cu-ZSM-5.

Generally, probing the transition metal Cu with UV-Vis DRS gives rise to ligand field induced d-d transitions determined by the number and position of atoms in the first coordination sphere, as well as a ligand-metal charge transfer (LMCT) band influenced by the optical electronegativity between the ligand and Cu.[37] UV-Vis diffuse reflectance spectra were recorded during the NH_3-SCR reaction on fresh and 850 °C steamed zeolite Cu-ZSM-5, and the results are shown in Figure 4.7a-b. The starting spectrum is the dehydrated Cu-ZSM-5 measured

before the NH$_3$-SCR reaction. A LMCT band with a lower wavenumber in the fresh Cu-ZSM-5 implies Cu^{2+} had an overall stronger interaction with its surrounding O^{2-} compared to the steamed zeolite. Upon reaction, the fresh and steamed zeolite Cu-ZSM-5 follow very similar trends in LMCT transition. The band position had a blue shift once the reactant gases were introduced, and the band position shifted to a lower wavenumber during the entire reaction process. In the NH$_3$-SCR reaction and its side reactions, N and O are the only two elements that need to be considered as the atom in the first coordination shell of Cu^{2+}. Substitution of O-oriented ligands to N-oriented NH$_3$ ligands drives the blue shift of LMCT band because NH$_3$ has a smaller optical electronegativity compared to oxygen-oriented ligands including H$_2$O, O^{2-}, OH$^-$ and NO$_x^-$, which generates a greater difference in energy level from Cu^{2+}.[37–39] The gradual red shift of the LMCT band with increasing reaction temperature is due to the removal of NH$_3$ and the stronger interaction with coordinated O^{2-}, i.e., the higher degree of covalency in the ligand-metal bond.[25]

To gain an intuitive look into the replacement of ligands in the reaction process, the wavenumber at half height of the LMCT maximum was followed in the NH$_3$-SCR reaction, by comparing to that of inflow of O$_2$/He, NH$_3$/He and NH$_3$ oxidation feeds (Figure 4.7c-d). In the fresh zeolite Cu-ZSM-5, the reaction could again be clearly divided into two regimes including the low-temperature (150-250 °C) and high temperature (300-450 °C) NH$_3$-SCR mechanism according to the position of the LMCT band half height. In the low temperature regime, the position of the LMCT band is shown at a high wavenumber, resembling that of the NH$_3$ oxidation condition and being close to the LMCT band position in NH$_3$/He, while at a temperature higher than 300 °C, the evolution of the LMCT band position is similar to that found in oxidative gases. This strongly suggests the predominant replacement of the first coordination shell atom to isolated Cu^{2+} from N to O during the reaction, in agreement with similar findings revealed by in-situ XAS and the proposed different reaction mechanism in low- and high-temperature NH$_3$-SCR.[40] In contrast, a less significant shift of the LMCT band during the reaction was observed in the steamed zeolite Cu-ZSM-5, suggesting a less notable change of the coordinated ligands because fewer Cu^{2+} sites were available to take part in the reaction on the surface of [Cu$_x$(OH)$_{2x-1}$]$^+$ oligomers/clusters. No clear demarcation line between the low and high temperature regime was found in the steamed sample, though it had been in the fresh Cu-ZSM-5 zeolite material. The LMCT band positions in NH$_3$-SCR reaction and O$_2$/He environments are similar, indicating the dominant coordinated ligand was O^{2-} probably originated from Cu^{2+}-OH in [Cu$_x$(OH)$_{2x-1}$]$^+$ oligomers/clusters in the

steamed Cu-ZSM-5. However, the LMCT band position under NH_3-SCR reaction conditions lies between its position in the NH_3/O_2 environment and NH_3/He environment, and thereby, the coordination with NH_3 cannot be ruled out.

4.3.3.2 Appearance of Pseudo-Tetrahedral Cu^{2+} in Low Temperature NH_3-Selective Catalytic Reduction of NO
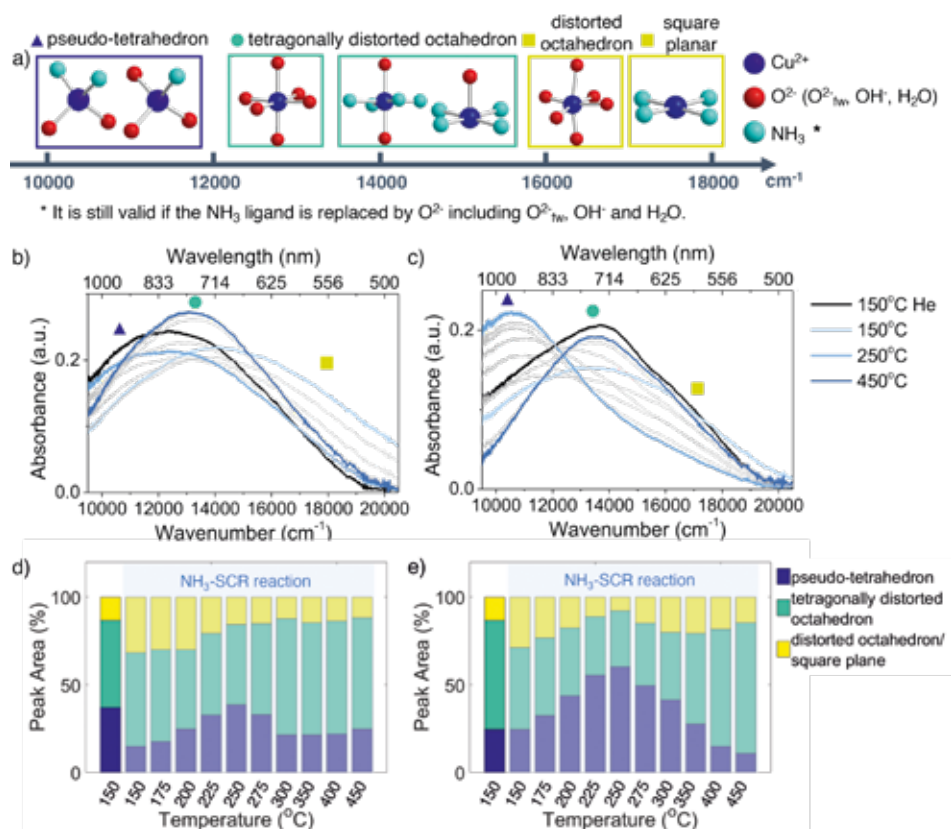
**Figure 4.8** a) Schematic of possible Cu^{2+}-complexes in zeolite Cu-ZSM-5 in the NH_3-Selective Catalytic Reduction (SCR) reaction and the corresponding approximate positions in wavenumbers of their corresponding bands, estimated based on ligand-field imposed d-d splitting of Cu^{2+}. The O^{2-}_{fw} represents framework oxygen. The d-d transition band and the peak fitting results of the (b, d) fresh and (c, e) 850 °C steamed zeolite Cu-ZSM-5 collected at steady-state at each temperature during the NH_3-SCR reaction catalytic test. The bands in grey color were collected in intermediate reaction temperatures between 150-450 °C. The positions of both main peak and shoulder are indicated in (a) by a solid triangle (Prussian blue), a circle (cyan) and a square (yellow), respectively.

The d-d transition region from the UV-Vis diffuse reflectance spectrum provides information on the geometric structure of Cu^{2+}. Incorporation of ligands in

different spatial locations has a significant impact on the extent of the splitting of d orbital, which is affected by the extent of interaction between the d orbital and the ligand. Figure 4.8b-c show the d-d transition band of fresh and 850 °C steamed zeolite Cu-ZSM-5 at steady-state from 150-450 °C in the NH_3-SCR reaction. In both data sets, three main absorption bands could be identified in the d-d transition region: below 12000 cm^{-1}, 12000-16000 cm^{-1} and above 16000 cm^{-1}. Despite the band broadening and overlapping resulting from the variety of ligand combinations and heterogeneity of Cu^{2+} symmetry, the appearance of two spectroscopic signatures at 10350 cm^{-1} and 13700 cm^{-1} are clearly identified in the UV-Vis spectra of 850 °C steamed Cu-ZSM-5. The change of Cu^{2+} symmetry was followed using ligand-field theory as well as previous experimental/theoretical studies on the Cu^{2+} UV-Vis diffuse reflectance spectrum.

As indicated by Figure 4.8b-c, low, medium, and high wavenumber bands could be identified in the d-d transition region. The adsorption band at ~12500 cm^{-1} is the typical band that arises from isolated Cu^{2+} in an octahedral crystal field generated by oxide ligands.[41] The $[Cu(H_2O)_6]^{2+}$ is the tetragonally distorted complex in the fully hydrated Cu-exchanged zeolites due to framework confinement. The dehydration process generates the axial elongation of Cu^{2+} tetragonal bipyramidal geometry upon water removal and framework attachment, which causes further splitting of octahedral ligand field and therefore the slight blue shift of the band maximum of the d-d transition.[25] The Cu^{2+} complex in a square-planar environment has a larger splitting of the d orbital compared to octahedral, according to crystal-field theory. The simulated d-d transition band energy for the near square planar complex $[Cu(NH_3)_4]^{2+}$ with optimized structure presented its maximum absorption at 19800 cm^{-1} ,which was in agreement with experimental observation.[42,43] The high wavenumber shoulder appeared in the low temperature NH_3-SCR reaction shown in Figure 4.8b-c centered at ca. 17000 cm^{-1}, suggesting the likely incorporation of a weaker field ligand O^{2-} that might cause the redshift of the peak, i.e., the formation of $[Cu(NH_3)_4(H_2O)_x]^{2+}$ (x=1,2). The high wavenumber band could also stem from the Cu^{2+} complex with low symmetry that enlarges the splitting of the d orbital. At a reaction temperature between 175-300 °C, the 10350 cm^{-1} band became apparent especially in the steamed zeolite Cu-ZSM-5. The lower wavenumber feature of such a band implicated the smaller splitting of d orbital compared to octahedral symmetry, probably due to the tetrahedral crystal field environment ($\Delta_T \approx 4/9$ Δ_O).[44] The 10350 cm^{-1} band was related to the coordinated NH_3 since it was also present in NH_3/O_2 and NH_3/He environments (Figure AIII5).

4

Partial de-ammoniation of Cu^{2+} caused a transition to square planar geometry, an extreme case of tetragonal distortion from octahedral symmetry, which is high in energy and is prone to relax to tetrahedral symmetry. In fact, the pseudo-tetrahedral Cu^{2+}-complex could be expected in zeolite Cu-ZSM-5. The Cu^{2+} lying in a defect site or on the surface of $[Cu_x(OH)_{2x-1}]^+$ oligomers/clusters probably had then required steric hindrance for the coordinating ligand to reach octahedral symmetry; instead, the more stable tetrahedron is favored. Indeed, the contribution of this low-wavenumber band increases with the steaming severity (Figure 4.9). A similar band maximum at 11000 cm^{-1} has been reported in ammoniated Cu-exchanged zeolite Y with a low coordination number.[45] This low-frequency band has been hypothesized as the O_3-Cu^{2+}-NH_3 structure in de-ammoniated Cu-zeolite, which was proven by multiconfigurational perturbation theory based simulation and an Electron Paramagnetic Resonance (EPR) study.[42,46] Hence, the low frequency feature is also proposed to be the pseudo-tetrahedral Cu^{2+} with a mix of NH_3 and O^{2-}-oriented ligands (O_3-Cu^{2+}-NH_3 or O_2-Cu^{2+}-$(NH_3)_2$).
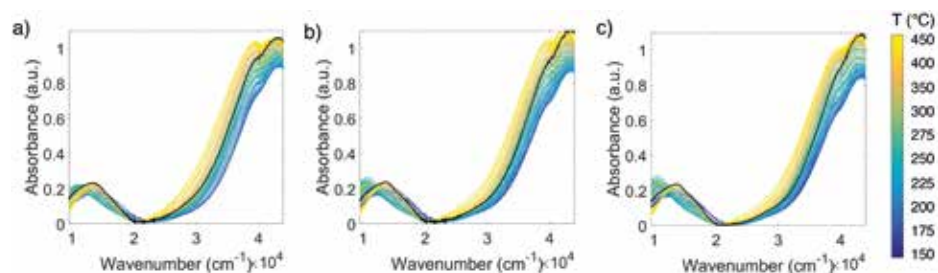
Figure 4.9 Operando UV-Vis diffuse reflectance spectra of the a) 650 °C, b) 700 °C and c) 750 °C steamed zeolite Cu-ZSM-5 during NH_3-SCR reaction.

To follow the evolution of Cu-complexes throughout the NH_3-SCR reaction, the d-d transition bands were fitted with three Gaussian functions by restricting fitting model parameters such as their wavenumber position based on the inspection of the eigenspectra from PCA (Figure 4.1). The such established fitting model was then applied to the entire dataset, and the fitting results can be found in Figure AIII3-4. Evolution of pseudo-tetrahedral Cu^{2+}, tetragonally distorted Cu^{2+} and low symmetrical Cu^{2+} in fresh and 850 °C steamed zeolite Cu-ZSM-5 at steady-state during the NH_3-SCR reaction are given in Figure 4.8d-e. Both Cu-ZSM-5 samples behaved in a similar manner during the reaction when following the peak contributions of pseudo-tetrahedral and distorted octahedron/square planar Cu^{2+} during the reaction. Upon the exposure to the reactant gases, ammoniated Cu^{2+} developed along with the coordination with

H$_2$O. This feature gradually diminished with increasing reaction temperature (150-250 °C) because of the detachment of NH$_3$ from Cu^{2+}. At the same time, the contribution of a pseudo-tetrahedral Cu^{2+}-complex with mixed NH$_3$ and O^{2-}-oriented ligands increased sharply. When the NH$_3$-SCR reaction took place above 250 °C, the amount of pseudo-tetrahedral Cu^{2+}-complex with mixed ligands started to decrease due to the continuous freeing of coordinated NH$_3$. In this scenario, the d-d transition band of UV-Vis diffuse reflectance spectrum in the NH$_3$-SCR reaction feed were eventually identical to that under O$_2$/He flow (Figure AIII6), suggesting complete removal of coordinated NH$_3$ and the presence of tetragonally distorted octahedral Cu^{2+} with O^{2-} ligands.
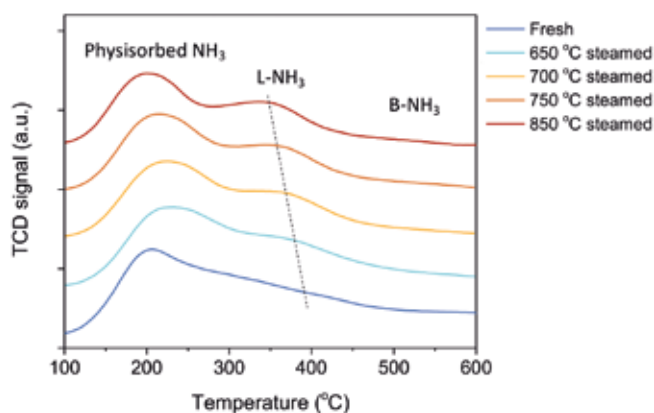
Figure 4.10 Ammonia-Temperature Programmed Desorption (NH$_3$-TPD) profiles of the fresh and steamed zeolites Cu-ZSM-5.

It is important to note that the change of Cu^{2+} geometry was due to the reaction-related dynamic but not the irreversible change of Cu^{2+} structure since the NO/NH$_3$ conversion as well as the geometry were unchanged when the NH$_3$-SCR reaction was conducted in a cyclic manner (Figure AIII7). In the low temperature regime (<250 °C), the NH$_3$-SCR reaction was the preferential reaction according to the catalytic results. The mobile [Cu(NH$_3$)$_4$]$^{2+}$ complex is the proposed catalytic active site that is ready to react with NO at a reaction temperature under 250 °C.[40,47,48] A higher portion of NH$_3$-solvated Cu^{2+} observed in the fresh zeolite Cu-ZSM-5 was attributed to the higher NO conversion at a low reaction temperature compared to the steamed Cu-ZSM-5. At a reaction temperature of 150-250 °C, the adsorbed NH$_3$ either desorbed or reacted with intermediates, resulting in partially de-ammoniated Cu^{2+} with pseudo-tetrahedral symmetry, which was simultaneously coordinated with O^{2-} or with the intermediate NO$_x^-$.[49,50] The accumulation of Cu^{2+} in pseudo-tetrahedral symmetry with

coordinated NH_3, which was stable below 250 °C, limited the NO and NH_3 conversion to a great extent particularly in steamed Cu-ZSM-5.

As the reaction temperature increased from 250 °C, the coordinated NH_3 in pseudo-tetrahedral Cu^{2+} started to disassociate, which could be proven by the desorption of NH_3 adsorbed on Cu^{2+} with Lewis acidity (Figure 4.10). However, such desorption of NH_3 from pseudo-tetrahedral Cu^{2+} provoked unselective NH_3 oxidation rather than the NH_3-SCR reaction, which is clear in the steamed Cu-ZSM-5 from the rapid increase of NH_3 conversion and a dramatic drop of NO conversion between 250-300 °C. Finally, in high-temperature NH_3-SCR above 300 °C, the adsorption of NH_3 weakened, rather, the fully de-ammoniated Cu^{2+} tended to anchor on the framework O^{2-} with coordination of four,[42,51] resulting in the identical geometric structure as it has in O_2/He flow. The Cu^{2+} complex with an O^{2-}-directing ligand is the key species for the high temperature NH_3-SCR reaction in fresh and steamed Cu-ZSM-5, allowing the maximum Cu^{2+} coordination number to be a distorted octahedron by interaction with external ligands, for example the possible reaction intermediates NO_2 or NO_x^-.

Particularly for 850 °C steamed Cu-ZSM-5, the Cu^{2+} geometry is identical in the NH_3-SCR reaction and unselective NH_3 oxidation reactions (Figure AIII5), which is strong proof of the great impact of unselective NH_3 oxidation in the NH_3-SCR reaction. It also points out the similarity of the Cu^{2+} local structure that is responsible for NH_3-SCR and unselective NH_3 oxidation. In the intermediate reaction temperature of 250-300 °C, desorption of NH_3 mainly took place on the surface of $[Cu_x(OH)_{2x-1}]^+$ oligomers/clusters and was followed by the rapid oxidation into NO, resulting in the sudden increase of NH_3 conversion.

4.3.4 Adsorption Competition Revealed by Operando Diffuse Reflectance Infrared Fourier Transform Spectroscopy

The low-temperature standard NH_3-SCR reaction (< 250 °C) attracts extra attention because improved NO conversion is needed in this temperature range. The NH_3-SCR catalysts inevitably deactivate from steam produced by fuel combustion. As indicated in the catalytic tests results, 250 °C is a critical point, from which the low-temperature NH_3-SCR starts to transit to the high-temperature reaction. At this temperature, no apparent side reaction takes place in the NH_3-SCR reaction even in the 850 °C steamed Cu-ZSM-5, as NH_3 and NO have the same conversion (Figure 4.3b), which is beneficial for investigating the behavior in NH_3-SCR without interference of side reactions. Adsorbed surface species are potentially useful to gain insight into the reaction and deactivation pathways. The

experimental protocol for the DRIFTS experiment is described in Figure 4.11a. The experiment was conducted at 250 °C after a calcination step in O$_2$/He. The reaction started with NH$_3$ oxidation, followed by NO addition and subsequent NH$_3$ removal to achieve NH$_3$-SCR and NO oxidation reaction conditions, respectively.

4.3.4.1 Observed Surface Species
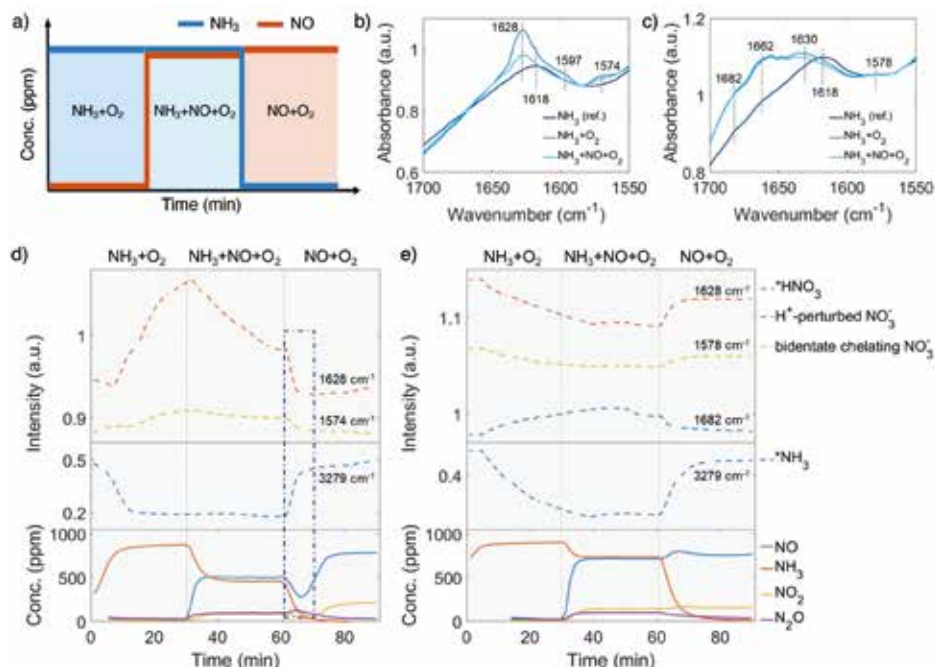
Figure 4.11 a) Procedure of the operando Diffuse Reflectance Fourier Transform Spectroscopy (DRIFTS) experiment. The experiment was conducted after O$_2$ calcination at 550 °C followed by NH$_3$+O$_2$, NH$_3$+NO+O$_2$ and NO+O$_2$ reaction at 250 °C with 1000 ppm of NH$_3$ and/or 1000 ppm NO balanced by 5% O$_2$/He. The obtained operando DRIFTS data of surface nitrates in b) fresh and c) 850 °C steamed zeolite ZSM-5. The evolution of selective bands representing surface nitrates (upper panel) and adsorbed NH$_3$ (middle panel) were followed, and the concentrations of effluent gas composition in the d) fresh and e) 850 °C steamed zeolite Cu-ZSM-5 were recorded (bottom panel). Missing datapoints at the beginning of the experiment (Fig. 4.11d-e, bottom panel) are due to values below the limit of detection.

Figure 4.11b-c shows the DRIFTS data recorded on fresh and 850 °C steamed Cu-ZSM-5 after exposure to NH$_3$, NH$_3$+NO+O$_2$ or NO+O$_2$ flow for 30 min at 250 °C. Surface nitrates produced in the operando DRIFTS experiments attract the most attention as they have been proposed as an important reaction intermediate. The vibration originating from adsorbed NO$_3^-$ species on zeolite Cu-ZSM-5 is in the range of 1570-1700 cm^{-1}, and the bridging nitrate is found at 1618 cm^{-1}

while the bidentate chelating nitrate is identified by 1597, 1578/1574 cm^{-1} bands in former FT-IR spectroscopy studies under NO_2 or $NO+O_2$ atmosphere.[11,52–54] The formation of a bidentate nitrate during NH_3-SCR has been validated in a Density Functional Theory (DFT) study.[50] And it should be noted that Lewis acid-adsorbed NH_3 (L-NH_3) has its N-H bending frequency at ~1620 cm^{-1}, therefore care should be taken to the assignment of the 1618 cm^{-1} band. However, the assignment of the 1628 cm^{-1} band is less conclusive. It is often attributed to the $v_{N=O}$ of a bridging nitrate where two vicinal Cu atoms are required to anchor two nitrate O^{2-}.[55] With this postulation, a stronger 1628 cm^{-1} band should be found in the steamed zeolite Cu-ZSM-5 as more adjacent Cu atoms are available when Cu aggregation has happened. However, this is contradicted by the fact that the 1628 cm^{-1} band is a shoulder in the steamed Cu-ZSM-5, while it is an intense peak in its fresh counterpart (Figure 4.11b-c). Alternatively, the 1628 cm^{-1} feature has been proposed to be the proton-perturbed chelating nitrate whose N=O vibration is affected by the nearby Brønsted acid site; this assignment was shown by a systematic FT-IR spectroscopy study of surface Cu^{2+}(N,O) species on Cu-CHA,[56] which could explain why the pronounced 1628 cm^{-1} band was more intense on the fresh Cu-ZSM-5 with well-defined Brønsted acid sites. The 1662 cm^{-1} and 1682 cm^{-1} band related to the adsorbed NO_2 are unique in the 850 °C steamed zeolite Cu-ZSM-5, where the former one can be attributed to adsorbed NO_2 while the latter one is from the protonated NO_2.[57,58] It is not surprising to observe NO_x adsorption on the surface of steamed Cu-ZSM-5 zeolites with abundant hydroxyl groups, which can lead to the formation of nitrous acid and/or nitric acid during the NH_3-SCR, NH_3 oxidation, or NO oxidation reactions in the operando DRIFTS experiments. The conversion between nitrous acid and nitric acid was kept in balance depending on the local concentrations of NO and NO_2. Finally, the 1682 cm^{-1} band was tentatively attributed to the adsorbed HNO_3, considering that HNO_2 is easily oxidized to HNO_3 at reaction conditions with excessive O_2.

4.3.4.2 Competitive Adsorption of Surface Species

Ammonia with a lone pair of electrons on the N side is one of the main surface species observed during the operando DRIFTS experiment. The typical symmetric and asymmetric stretching modes of adsorbed NH_3 are in the region of 3400-3000 cm^{-1} with strong absorbance. The band at ~3180 cm^{-1} together with a 1617 cm^{-1} band are characteristic of the L-NH_3,[53] which could be observed in fresh and steamed Cu-ZSM-5 zeolites once the catalysts were exposed to NH_3/O_2 (Figure 4.12). The evolution of important surface species including adsorbed HNO_3, H^+-perturbed nitrate, chelating bidentate nitrate, as well as adsorbed NH_3 are shown in Figure 4.11d-e, together with the real-time concentration of reactants and products.

In the first step of the operando DRIFTS experiment on the fresh Cu-ZSM-5 zeolite, nitrates developed in NH$_3$/O$_2$ flow (NH$_3$ oxidation reaction), suggesting the full oxidation of surface NH$_3$, which was also observed in in-situ FT-IR studies on the NH$_3$ oxidation reaction.[59,60] The formed nitrates replaced the pre-adsorbed NH$_3$ on Cu^{2+} and weakened the adsorbed NH$_3$ signal (Figure 4.11d and 4.12a). The re-appearance of the Brønsted acid sites at the steady state in NH$_3$ oxidation reaction (Figure 4.12a) might be due to the reaction between the Brønsted acid adsorbed NH$_3$ (B-NH$_3$) and L-NO$_3^-$ followed by restoration of the proton from H-cleavage of NH$_3$.[61] The NH$_3$ oxidation reaction was followed by the NH$_3$-SCR reaction where NO participated and reacted with surface nitrates, resulting in the formation of NO$_2$ and NO$_2^-$ (Reaction 2, Figure 4.13) that avoid the surface blockage by nitrates.[3] Unfortunately, we cannot confirm the formation of surface nitrites as the O-N-O stretching frequency was covered by the signal from symmetric stretching of N-H as well as the intense signal from the zeolite structure.[62,63] In the last step of NH$_3$ removal, consumption of surface nitrate species accelerated. The involvement of NO in nitrate depletion is now strongly supported by the simultaneous drop of effluent NO concentration as surface nitrates were decreasing, which is indicated by the blue rectangle in Figure 4.11d. Interestingly, once the nitrates were depleted, the Cu^{2+} site was re-occupied by the residual NH$_3$ (Figure 4.11d, middle and bottom panel). In fact, a similar phenomenon of NH$_3$-nitrates competitive adsorption has been reported in Cu-exchanged zeolites, where adsorbed nitrates and NH$_3$ on Lewis acid sites could be replaced by each other depending on reaction conditions.[10,64,65] The Lewis acid, which is isolated Cu^{2+} in our case of fresh Cu-ZSM-5, is thus the suggested main site for NH$_3$ adsorption and nitrate formation/adsorption according to the changes of perturbed framework vibration with surface species (Figure 4.12a).

The causes of deactivation were revealed from the operando DRIFTS data collected on the 850 °C steamed Cu-ZSM-5 zeolite (Figure 4.11e). In NH$_3$/O$_2$ flow, adsorbed NH$_3$ and nitrates developed in the initial stage, followed by the disappearance of both surface species along with the increased adsorbed nitric acid (Figure 4.11e, 4.12b). No significant change of surface species was observed upon the subsequent addition of NO in the second step. Similarly, the NH$_3$ desorption in NH$_3$/O$_2$ flow could be explained by the competitive adsorption between NH$_3$ and nitric acid, because these two species exhibited opposite trends throughout the whole DRIFTS experiment (Figure 4.11e). The production of nitric acid is related to the attenuation of surface nitrates (Figure 4.11e), which can react with the adjacent proton H$^+$/hydronium or surface hydroxyl group to from nitric acid (Reaction 4, Figure 4.13).[53] The observed adsorbed NO$_2$ was the precursor for nitric acid

formation, showing good agreement with an in-situ FT-IR study conducted on hydroxyl-rich or hydrated silica, γ-Al$_2$O$_3$ and TiO$_2$.[58,66,67] In the final step in NO/O$_2$, analogous to the nitrate depletion in the fresh sample, nitric acid was reduced by NO as indicated in Figure 4.11e (Reaction 5, Figure 4.13), producing NO$_2$ that could turn into nitrate by disproportionation reaction (Reaction 1, Figure 4.13).[58,68] The surface coverage of nitrates and nitric acid results from the competition between formation and consumption (Reaction 1 and 4-6, Figure 4.13).
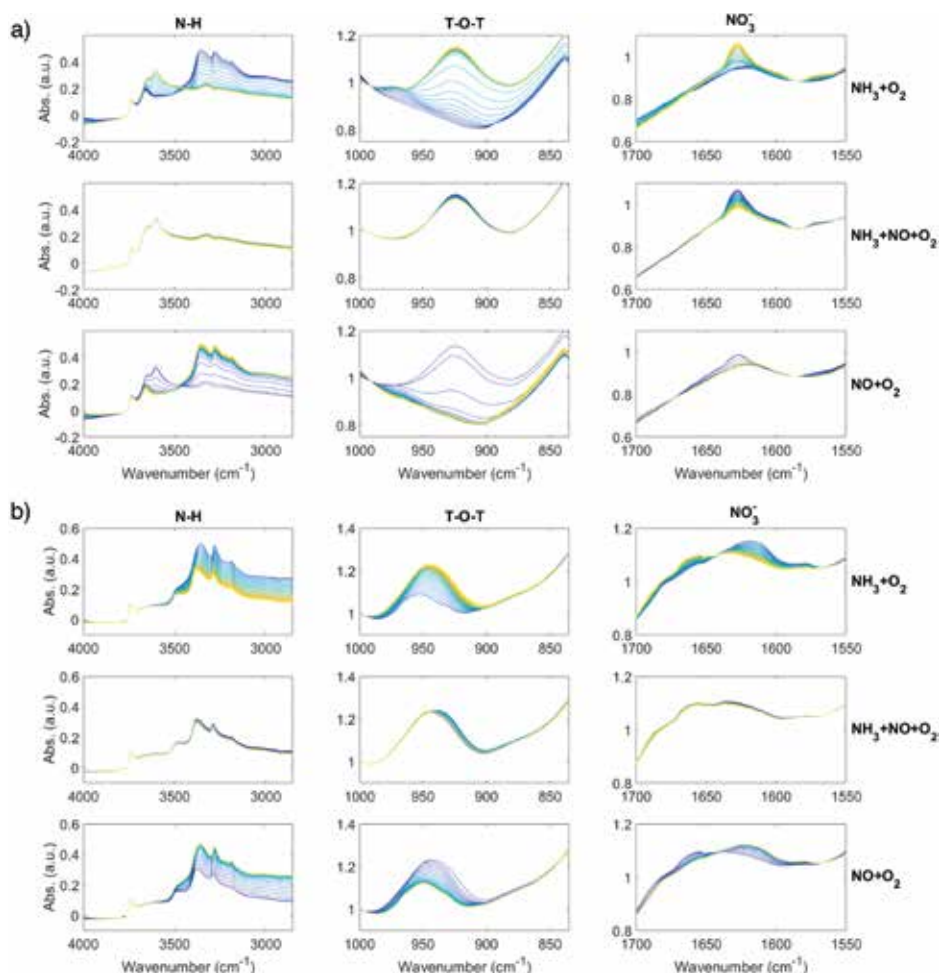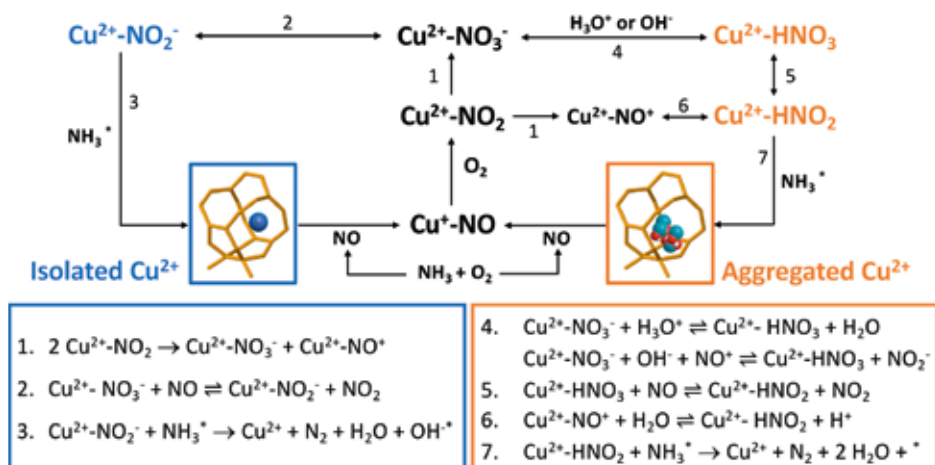

Figure 4.12 Operando Diffuse Reflectance Infrared Fourier Transform Spectroscopy (DRIFTS) data of a) fresh and b) 850 °C steamed Cu-ZSM-5 recorded during a flow of NH$_3$+O$_2$ (the first row), NH$_3$+NO+O$_2$ (the second row) and NO+O$_2$ (the third row) at 250 °C for 30min. The vibrational regions of O-H/N-H stretching (the first column), perturbed framework T-O-T vibration (the second column) and N=O stretching (the third column) are shown. The color indicated in spectral changes from blue to yellow following the reaction time in each subfigure.

The competitive adsorption of NH$_3$ and surface nitrates/nitric acid occurred on both fresh and 850 °C steamed Cu-ZSM-5 zeolites. With the replacement of adsorbed NH$_3$, framework stabilized Cu^{2+} with associated nitrate/nitric acid was generated, which was evidenced by the appearance of perturbed framework vibration by Cu^{2+} (in the fresh Cu-ZSM-5) and [Cu$_x$(OH)$_{2x-1}$]$^+$ oligomers/clusters (in the 850 °C steamed Cu-ZSM-5) as demonstrated in Figure 4.12. Not all the [CuOH]$^+$ sites were involved in the reaction since they were partially preserved in NH$_3$-rich flow and were not perturbed by surface nitrates, indicated by the O-H stretching region in Figure 4.12a. Nitric acid rather than nitrates was the more stable intermediate that was more ready to react with adsorbed NH$_3$ in the 850 °C steamed Cu-ZSM-5.

4.3.4.3 Nitrate Mediated Reaction Network

The main reaction discussed here is the standard NH$_3$-SCR reaction, which has competition from side reactions that bring about an intricate reaction system. Adsorbed neutral and ionic NO$_x$ were the most common spectator species in the operando DRIFTS experiment, and the plausible interconversion between adsorbates is summarized in Figure 4.13.[3,53,68,69] It is noted that all reactions in Figure 4.13 can happen in fresh and steamed Cu-ZSM-5 zeolites, but reaction routes involving HNO$_x$ are more privileged in the steamed Cu-ZSM-5 due to the presence of more aggregated Cu sites.

Figure 4.13 Possible reactions that take place in the low-temperature NH$_3$-Selective Catalytic Reduction (SCR) reaction over Cu-ZSM-5 zeolites based on the operando Diffuse Reflectance Infrared Fourier Transform Spectroscopy (DRIFTS) data. The blue color indicates dominant reactions that can take place on isolated Cu^{2+}, while the orange color stands for possible reactions over aggregated Cu^{2+} species, such as [Cu$_x$(OH)$_{2x-1}$]$^+$ oligomers/clusters.

The coupling of NO oxidation and NH_3 oxidation with the standard NH_3-SCR reaction is through surface nitrates, which are formed from adsorbed NO_2. NO_2 can be formed through several reaction pathways at NH_3-SCR reaction conditions according to the catalytic results (Figure 4.2 and 4.3). NO_2 is one of the byproducts generated from the participation of either NO oxidation reaction below 250 °C or unselective NH_3 oxidation reaction above 250 °C. The NO oxidation reaction produces NO_2, which is formed via reaction between dissociated O_2 and loosely adsorbed NO according to a detailed kinetic model of NO oxidation.[70] For NH_3 oxidation, although its reaction mechanism is still under debate, a two-step reaction pathway named 'the internal SCR mechanism' has been proposed where NH_3 is first oxidized to NO_x followed by the NH_3-SCR reaction.[1,61]

In the NH_3-SCR reaction, the NO oxidation with molecule O_2 into nitrates through the formation of NO_2 has been stressed as it is suggested as a rate-determined step.[50] The formation of NO_2 promotes the formation of surface nitrates and meanwhile boosts the reoxidation of Cu^+ to Cu^{2+} in the oxidation half cycle.[71–74] A Cu monomer in Cu-exchanged zeolites has been reported as the NO_2 adsorption site, enabling NH_3-SCR reaction to proceed with NO_2 intermediate.[75] Nevertheless, NO_2 could be also detected as an undesired side product. Upon encountering the hydroxylated or hydrated surface, nitrates could be protonated to form surface nitric acid, which happened in the 850 °C steamed Cu-ZSM-5. However, the surface nitrite rather than nitrate is the key intermediate for the desired N_2 production, demonstrating the importance of nitrate-nitrite equilibrium (Reaction 2 and 5, Figure 4.13) which greatly influences the reaction selectivity. Shifting the equilibrium towards nitrite formation witnessed in both fresh and steamed Cu-ZSM-5 zeolites, deduced by the nitrate depletion with the introduction of NO in NH_3/O_2 feed in the *operando* DRIFTS experiments. A similar founding was also described a combined FTIR-XAS study on zeolite Cu-SSZ-13.[76] Successive reaction of nitrites/nitrous acid with L-NH_3 lead to products formation (Reaction 3 and 7, Figure 4.13). Participation of B-NH_3 was not observed based on the *operando* DRIFTS data because of the observation of well-preserved of Brønsted acid sites. In contrast, some previous studies suggested the surface NH_4NO_3/NH_4NO_2 is reaction intermediate that decompose to N_2O/N_2 at reaction temperatures.[53,72,77]

4.3.4.4 Important Mechanistic Implications
Several mechanistic implications related to the low temperature NH_3-SCR reaction could be obtained from the operando DRIFTS data. Firstly, adsorbed

NH$_3$ reacts with NO$_x$ via a Langmuir-Hinshelwood mechanism that surface reaction takes place between two adsorbed species.[1] It is concluded based on the fact that the adsorbed NH$_3$ did not directly react with gaseous NO/O$_2$ indicated in the third step in the DRIFTS experiment, but react with surface nitrates, as inferred from the restoration of the Brønsted acid site and [CuOH]$^+$ after the NO$_3^-$ developed in the NH$_3$/O$_2$ step (Figure 4.11d and 4.12a). Secondly, the participation of NO in the NH$_3$-SCR reaction can happen via the reaction with surface nitrates as explained by the nitrates depletion after NO addition to the NH$_3$/O$_2$ feed in operando DRIFTS experiment (Figure 4.11d). Surface nitrates are more likely to form from NO/O$_2$ in the steamed Cu-ZSM-5 with [Cu$_x$(OH)$_{2x-1}$]$^+$ oligomers/clusters proven by the observation of nitrate development in NO/O$_2$ feed shown in Figure 4.12b. Finally, no direct participation of a Brønsted acid was found during NH$_3$-SCR reaction at steady state, since the OH stretching signal of Brønsted acid sites was well preserved at NH$_3$-SCR reaction condition (Figure 4.12a). However, the proton from Al-O(H)-Si perturbed the surface nitrates, weakened the OH stretching and caused the redshift of its original vibration of 3610 cm^{-1} after calcination (Figure 4.4b) to 3602 cm^{-1} when surface nitrates were formed (Figure 4.12a). In this way, with the perturbance from the Brønsted acid, the structure of surface nitrates resembles nitric acid, which probably facilitates the reaction with NH$_3$. However, if surface nitrates/nitrites and B-NH$_3$ coexist in proximity, ammonium nitrate or ammonium nitrite could be formed, followed by thermal decomposition at reaction temperature.[53,77]

4.3.5   Structure-Intermediate-Performance Relationship

A structure-intermediate-performance relationship can be established to elucidate the reasons behind the high activity at low temperature for the NH$_3$-SCR reaction in fresh Cu-ZSM-5 and the undesirable side reactions in the steamed Cu-ZSM-5 by correlating the results from the operando UV-Vis DRS and DRIFTS experiments. NH$_3$ did not completely desorb from Lewis sites according to NH$_3$-TPD and operando UV-Vis diffuse reflectance spectra at a low reaction temperature.

Adsorbed NH$_3$ is prerequisite for the low temperature reaction (<250 °C), which is ready to react with the surface nitrites/nitrates intermediates. The higher coordination number of Cu^{2+} in tetragonally-distorted octahedral symmetry in the fresh Cu-ZSM-5 ensures that enough empty orbitals are available for stabilizing nitrites/nitrates, together with prevalent NH$_3$ ligands judged by the evolution of the LMCT band. It is noted that the complete desorption of L-NH$_3$ happened at ~400 °C in NH$_3$-TPD. Therefore, low surface coverage of L-NH$_3$ at

250 °C during the NH_3-SCR reaction observed in operando DRIFTS experiment (Figure 4.12a) implied the highly active nature of adsorbed NH_3 on isolated Cu^{2+} for the formation of nitrites/nitrates intermediates.

As for the 850 °C steamed Cu-ZSM-5 zeolite, NO and NH_3 conversion was low at 150-250 °C during which the pseudo-tetrahedral Cu^{2+} (O_3-Cu^{2+}-NH_3 or O_2-Cu^{2+}-$(NH_3)_2$) accumulated, which was likely due to the co-adsorption of NH_3 and nitrates/nitric acid on $[Cu_x(OH)_{2x-1}]^+$ oligomers/clusters. A slower reaction rate between adsorbed NH_3 and nitrates/nitric acid was found on $[Cu_x(OH)_{2x-1}]^+$ oligomers/clusters because of the co-existence of these surface species. And the surface coverage of nitrites/nitrates intermediates was also lower in the steamed Cu-ZSM-5 zeolite compared to that of in its fresh counterpart (Figure 4.11d-e). When the L-NH_3 desorption started from 250 °C, the Cu^{2+} in pseudo-tetrahedral symmetry also began to disappear due to NH_3 removal indicated by Figure 4.8c and 4.8e. In the steamed Cu-ZSM-5, the freed NH_3 was expeditiously oxidized and released NO from the surface of $[Cu_x(OH)_{2x-1}]^+$ oligomers/clusters because of its weaker coordinating ability to stabilize reaction intermediates. This caused the peaked conversion of NH_3 and the undesired NO production at 250-300 °C. Additionally, in the 850 °C steamed Cu-ZSM-5, the same active unit and the same intermediate resulted in the same pseudo-tetrahedral Cu^{2+} structure with mixed NH_3 and nitrates/nitric acid in the NH_3-SCR and NH_3 oxidation reaction process. The $[Cu_x(OH)_{2x-1}]^+$ oligomers/clusters could be further aggregated into $Cu(OH)_2$, which was recently proposed as the precursor of the inactive $CuAl_2O_4$ species.[9]

4.3.6   Practical Implication of Detected Acidic Products

Understanding the relationship between the NH_3-SCR reaction and its side reactions including NH_3 oxidation and NO oxidation is required to address the practical problems. The NH_3-SCR catalysts, which are Cu-based zeolites, inevitably experience hydrothermal aging in the exhaust pipe of a vehicle. This causes irreversible structural damage that starts from local degradation of framework Al or Cu migration/aggregation. Changes in the structural properties tune the reaction direction and consequently the reaction activity and selectivity. Protonated NO_2 was identified as a significant spectator based on the operando DRIFTS experiment over the steamed zeolite Cu-ZSM-5, suggesting a hydroxylated environment around the NO_2 adsorption site, for example the $[Cu_x(OH)_{2x-1}]^+$ oligomers/clusters found in this study. Moreover, the effects of abundant internal silanol groups generated from the steaming process cannot be ruled out, which is facilitated for H_2O adsorption via hydrogen bonding. Hydroxyl groups and H_2O should be considered in the nitrate-mediated reaction

network, resulting in the formation of HNO$_3$ and HNO$_2$ according to Reactions 4-6 in Figure 4.13. The acid-base reaction between HNO$_x$ and NH$_3$ can occur to form NH$_4$NO$_x$ which is capable of decomposing into N$_2$ or N$_2$O.[53,78,79] It should be stressed that the HNO$_3$/HNO$_2$ formation is not exclusive to the steamed zeolite since it has also been reported to be involved in elementary steps in the NH$_3$-SCR reaction in a microkinetic model over Cu-ZSM-5.[78]

Although NO$_2$ incorporates in the reaction through fast NH$_3$-SCR or is converted into surface NO$_x^-$ or HNO$_x$, excessive NO$_2$ was still detected from the outlet even from the fresh zeolite Cu-ZSM-5. Considering the practical reaction conditions after a vehicle engine, the limited amount of acidic NO$_2$ byproduct can convert to nitric acid in H$_2$O vapor (4NO$_2$ + 2H$_2$O + O$_2$ $\rightleftharpoons$ 4HNO$_3$) produced by diesel combustion, while the nitric acid can also be reversely decomposed to NO$_2$ at relatively high operational temperatures. Therefore, another adsorbent/catalyst to trap or further remove of possible undesired acidic components is still necessary after the NH$_3$-SCR unit in an automotive emission control system. Alkali or alkaline earth metal oxide based materials are promising Lean NO$_x$ Trap (LNT) catalysts,[80] which can be placed at the exist of the NH$_3$-SCR unit to limit the emission of acidic byproducts.

4.4 Conclusions

Side reactions in the NH$_3$-SCR reaction, such as NO oxidation and NH$_3$ oxidation, should not be neglected, especially when considering the practical application of the Cu-zeolite-based catalysts in the tailpipe exhaust treatment of diesel vehicles. The contribution of NO oxidation was found at low reaction temperatures (<250 °C), which is considered an essential temperature range for Cu$^+$ reoxidation in the redox cycle. When the reaction temperature is higher than 250 °C, the contribution from unselective NH$_3$ oxidation accelerated and produced NO, resulting in a 'dip' shape of the NO conversion curve in the NH$_3$-SCR reaction in steamed Cu-ZSM-5 zeolites. The occurrence of unselective NH$_3$ oxidation was found to be more significant in the more severely steamed Cu-ZSM-5 samples, which was ascribed to the aggregation of Cu whose structure is postulated to be [Cu$_x$(OH)$_{2x-1}$]$^+$ oligomers/clusters.

Combining the results from the operando UV-Vis DRS and DRIFTS experiments, we propose that Cu^{2+} probably degraded into [Cu$_x$(OH)$_{2x-1}$]$^+$ oligomers/clusters, which can further grow into Cu(OH)$_2$ nanoparticles in the steamed zeolite Cu-ZSM-5. The dynamic changes in the symmetry of the Cu^{2+} complex revealed via operando UV-Vis DRS show the structural reasons for the high NH$_3$-SCR

reaction activity of the fresh Cu-ZSM-5 and the deactivation of steamed Cu-ZSM-5. Octahedral Cu^{2+} with a coordination number of six can be formed during the NH_3-SCR reaction in the fresh Cu-ZSM-5, facilitating the reaction with a high surface coverage of intermediates. The low temperature reaction showed the preference for NH_3 coordination, which is replaced by O^{2-}-oriented ligands at elevated reaction temperature, confirming different reaction mechanisms in low- and high-temperature NH_3-SCR reaction. There was a more pronounced formation of pseudo-tetrahedral Cu^{2+} in the steamed Cu-ZSM-5 during the low temperature reaction. The pseudo-tetrahedral symmetry is closely related to partially de-ammoniated Cu^{2+} and its adsorption of reaction intermediates on the surface of $[Cu_x(OH)_{2x-1}]^+$ oligomers/clusters. The relaxation of this distorted structure by further removal of NH_3 ligand brings about the undesired NH_3 oxidation reaction. It should be noted that the same geometric structure of a Cu^{2+} center is shared with low-temperature NH_3-SCR and NH_3 oxidation, but higher NH_3 conversion was found in the NH_3-SCR reaction, stressing the important role of NO in NH_3-SCR reaction.

The performed operando DRIFTS experiments suggest that isolated Cu^{2+} in the fresh Cu-ZSM-5 and the $[Cu_x(OH)_{2x-1}]^+$ oligomers/clusters in the steamed Cu-ZSM-5 are the main sites participating in the NH_3-SCR reaction up to 250 °C. This can be concluded from the competitive adsorption between NH_3 and surface nitrates/nitric acid at 250 °C, because they share the same adsorption sites on Lewis acid sites. Surface nitrates are the key surface species to bridge the NH_3-SCR, NH_3 oxidation and NO oxidation reactions. However, surface nitric acid was more prevalent in the steamed Cu-ZSM-5 because of the high density of hydroxyl groups. The high surface coverage of nitrates/nitric acid was reconciled by the reaction with NO to avoid the surface blockage; this reaction governs the nitrate-nitrite equilibrium that determines the selectivity of the reaction. Additionally, no direct involvement of Brønsted acid sites in the NH_3-SCR reaction was observed at the steady state, instead, the surface nitrates were perturbed by the nearby proton, probably from the Brønsted acid sites. Finally, a structure-intermediate-performance relationship could be established to elucidate the low NH_3-SCR activity and the 'dip' shape of NO conversion curve in the steamed Cu-ZSM-5: the associated NH_3 and nitrate/nitric acid on pseudo-tetrahedral Cu^{2+} complex of $[Cu_x(OH)_{2x-1}]^+$ oligomers/clusters exhibited low reactivity below 250 °C; further increase in temperature (above 250 °C) released the NH_3 and directed the unselective NH_3 oxidation. For practical implications, the formation of adsorbed NO_2 and surface nitric acid should be considered for a better design of vehicle exhaust control systems to meet the requirement of future stringent regulations.

Acknowledgements

REFERENCES

1 A. M. Beale, F. Gao, I. Lezcano-Gonzalez, C. H. F. Peden and J. Szanyi, *Chem. Soc. Rev.*, 2015, **44**, 7371–7405.

2 J. Wang, H. Zhao, G. Haller and Y. Li, *Appl. Catal. B Environ.*, 2017, **202**, 346–354.

3 F. Gao, J. H. Kwak, J. Szanyi and C. H. F. Peden, *Top. Catal.*, 2013, **56**, 1441–1459.

4 M. Iwamoto, H. Furukawa, Y. Mine, F. Uemura, S. Mikuriya and S. Kagawa, *J. Chem. Soc. Chem. Commun.*, 1986, 1272–1273.

5 D. Wang, Y. Jangjou, Y. Liu, M. K. Sharma, J. Luo, J. Li, K. Kamasamudram and W. S. Epling, *Appl. Catal. B Environ.*, 2015, **165**, 438–445.

6 W. Su, Z. Li, Y. Peng and J. Li, *Phys. Chem. Chem. Phys.*, 2015, **17**, 29142–29149.

7 A. Wang, Y. Chen, E. D. Walter, N. M. Washton, D. Mei, T. Varga, Y. Wang, J. Szanyi, Y. Wang, C. H. F. Peden and F. Gao, *Nat. Commun.*, 2019, **10**, 1137.

8 J. Song, Y. Wang, E. D. Walter, N. M. Washton, D. Mei, L. Kovarik, M. H. Engelhard, S. Prodinger, Y. Wang, C. H. F. Peden and F. Gao, *ACS Catal.*, 2017, **7**, 8214–8227.

9 Y. Ma, X. Wu, L. Liu, L. Cao, R. Ran, Z. Si, F. Gao and D. Weng, *Appl. Catal. B Environ.*, 2020, **278**, 119306.

10 H. Sjövall, L. Olsson, E. Fridell and R. J. Blint, *Appl. Catal. B Environ.*, 2006, **64**, 180–188.

11 M. P. Ruggeri, I. Nova, E. Tronconi, J. A. Pihl, T. J. Toops and W. P. Partridge, *Appl. Catal. B Environ.*, 2015, **166**–**167**, 181–192.

12 F. Gao, E. D. Walter, M. Kollar, Y. Wang, J. Szanyi and C. H. F. Peden, *J. Catal.*, 2014, **319**, 1–14.

13 T. Yu, J. Wang, Y. Huang, M. Shen, W. Li and J. Wang, *ChemCatChem*, 2014, **6**, 2074–2083.

14 P. S. Metkar, V. Balakotaiah and M. P. Harold, *Catal. Today*, 2012, **184**, 115–128.

15 X. Ye, J. E. Schmidt, R. Wang, I. K. Ravenhorst, R. Oord, T. Chen, F. Groot, F. Meirer and B. M. Weckhuysen, *Angew. Chem. Int. Ed.*, 2020, **59**, 15610–15617.

16 F. Gao, Y. Wang, N. M. Washton, M. Kollár, J. Szanyi and C. H. F. Peden, *ACS Catal.*, 2015, **5**, 6780–6791.

17 D. Wang, L. Zhang, J. Li, K. Kamasamudram and W. S. Epling, *Catal. Today*, 2014, **231**, 64–74.

18 W. B. Williamson and J. H. Lunsford, *J. Phys. Chem.*, 1976, **80**, 2664–2671.

19 L. Olsson, K. Wijayanti, K. Leistner, A. Kumar, S. Y. Joshi, K. Kamasamudram, N. W. Currier and A. Yezerets, *Appl. Catal. B Environ.*, 2015, **174**–**175**, 212–224.

20 Y. J. Kim, P. S. Kim and C. H. Kim, *Appl. Catal. A Gen.*, 2019, **569**, 175–180.

21 F. Gao, E. D. Walter, E. M. Karp, J. Luo, R. G. Tonkyn, J. H. Kwak, J. Szanyi and C. H. F. Peden, *J. Catal.*, 2013, **300**, 20–29.

22 J. Holzinger, P. Beato, L. F. Lundegaard and J. Skibsted, *J. Phys. Chem. C*, 2018, **122**, 15595–15613.

23 J. A. van Bokhoven, D. C. Koningsberger, P. Kunkeler and H. van Bekkum, *J. Catal.*, 2002, **211**, 540–547.

24 S. Bordiga, C. Lamberti, F. Bonino, A. Travert and F. Thibault-Starzyk, *Chem. Soc. Rev.*, 2015, **44**, 7262–7341.

25 F. Giordanino, P. N. R. Vennestrøm, L. F. Lundegaard, F. N. Stappen, S. Mossin, P. Beato, S. Bordiga and C. Lamberti, *Dalt. Trans.*, 2013, **42**, 12741–12761.

26 M. Ravi, V. L. Sushkevich and J. A. van Bokhoven, *J. Phys. Chem. C*, 2019, **123**, 15139–15144.

27 G. J. Millar, A. Canning, G. Rose, B. Wood, L. Trewartha and I. D. R. Mackinnon, *J. Catal.*, 1999, **183**, 169–181.

28 P. N. R. Vennestrøm, T. V. W. Janssens, A. Kustov, M. Grill, A. Puig-Molina, L. F. Lundegaard, R. R. Tiruvalam, P. Concepción and A. Corma, *J. Catal.*, 2014, **309**, 477–490.

29 C. W. Andersen, E. Borfecchia, M. Bremholm, M. R. V. Jørgensen, P. N. R. Vennestrøm, C. Lamberti, L. F. Lundegaard and B. B. Iversen, *Angew. Chem. Int. Ed.*, 2017, **56**, 10367–10372.

4

30 J. Sárkány,
    Appl. Catal. A Gen., 1999, **188**, 369–379.

31 H. Y. Chen, L. Chen, J. Lin, K. L. Tan and J. Li,
    Inorg. Chem., 1997, **36**, 1417–1423.

32 E. Broclawik, J. Datka, B. Gil and P. Kozyra,
    Phys. Chem. Chem. Phys., 2000, **2**, 401–405.

33 P. E. Fanning and M. A. Vannice,
    J. Catal., 2002, **207**, 166–182.

34 H.-Y. Chen, Z. Wei, M. Kollar, F. Gao, Y. Wang,
    J. Szanyi and C. H. F. Peden,
    Catal. Today, 2016, **267**, 17–27.

35 F. Gao and C. Peden, *Catalysts*, 2018, **8**, 140.

36 M. H. Groothaert, K. Lievens, H. Leeman,
    B. M. Weckhuysen and R. A. Schoonheydt,
    J. Catal., 2003, **220**, 500–512.

37 R. A. Schoonheydt,
    Chem. Soc. Rev., 2010, **39**, 5051–5066.

38 E. Borfecchia, C. Negri, K. A. Lomachenko,
    C. Lamberti, T. V. W. Janssens and G. Berlier,
    React. Chem. Eng., 2019, **4**, 1067–1080.

39 C. Negri, M. Signorile, N. G. Porcaro,
    E. Borfecchia, G. Berlier, T. V. W. Janssens and
    S. Bordiga, *Appl. Catal. A Gen.*, 2019, **578**, 1–9.

40 K. A. Lomachenko, E. Borfecchia, C. Negri,
    G. Berlier, C. Lamberti, P. Beato, H. Falsig and
    S. Bordiga, *J. Am. Chem. Soc.*, 2016, **138**, 12025–
    12028.

41 S. A. Yashnik, Z. R. Ismagilov and V. F. Anufrienko,
    Catal. Today, 2005, **110**, 310–322.

42 A. Delabie, K. Pierloot, M. H. Groothaert,
    B. M. Weckhuysen and R. A. Schoonheydt,
    Microporous Mesoporous Mater., 2000, **37**,
    209–222.

43 V. F. Anufrienko, R. A. Shutilov, G. A. Zenkovets,
    V. Y. Gavrilov, N. T. Vasenin, A. A. Shubin,
    T. V Larina, A. V Zhuzhgov, Z. R. Ismagilov and
    V. N. Parmon, *Russ. J. Inorg. Chem.*, 2012, **57**,
    1285–1290.

44 P. Atkins, T. Overton, J. Rourker and M. Weller,
    *Shriver and Atkin's Inorganic Chemistry, Fifth
    Edition*, Oxford University Press, Oxford, 2010.

45 W. de Wilde, R. A. Schoonheydt and
    J. B. Uytterhoeven, in *ACS Symposium Series*,
    Washington, 1977, pp. 132–143.

46 E. F. Vansant and J. H. Lunsford,
    J. Phys. Chem., 1972, **76**, 2860–2865.

47 C. Paolucci, I. Khurana, A. A. Parekh, S. Li,
    A. J. Shih, H. Li, J. R. Di Iorio, J. D. Albarracin-
    Caballero, A. Yezerets, J. T. Miller, W. N. Delgass,
    F. H. Ribeiro, W. F. Schneider and R. Gounder,
    Science, 2017, **357**, 898–903.

48 A. Marberger, A. W. Petrov, P. Steiger, M. Elsener,
    O. Kröcher, M. Nachtegaal and D. Ferri,
    Nat. Catal., 2018, **1**, 221–227.

49 C. Negri, E. Borfecchia, M. Cutini,
    K. A. Lomachenko, T. V. W. Janssens, G. Berlier
    and S. Bordiga,
    ChemCatChem, 2019, **11**, 3828–3838.

50 T. V. W. Janssens, H. Falsig, L. F. Lundegaard,
    P. N. R. Vennestrøm, S. B. Rasmussen,
    P. G. Moses, F. Giordanino, E. Borfecchia,
    K. A. Lomachenko, C. Lamberti, S. Bordiga,
    A. Godiksen, S. Mossin and P. Beato,
    ACS Catal., 2015, **5**, 2832–2845.

51 D. Nachtigallová, P. Nachtigall and J. Sauer,
    Phys. Chem. Chem. Phys., 2001, **3**, 1552–1559.

52 J. Szanyi, J. H. Kwak, R. J. Chimentao and
    C. H. F. Peden, *J. Phys. Chem. C*, 2007, **111**,
    2661–2669.

53 D. Wang, L. Zhang, K. Kamasamudram and
    W. S. Epling, *ACS Catal.*, 2013, **3**, 871–881.

54 G. M. Underwood, T. M. Miller and V. H. Grassian,
    J. Phys. Chem. A, 1999, **103**, 6184–6190.

55 K. I. Hadjiivanov, *Catal. Rev.*, 2000, **42**, 71–144.

56 C. Negri, P. S. Hammershøi, T. V. W. Janssens,
    P. Beato, G. Berlier and S. Bordiga,
    Chem. Eur. J., 2018, **24**, 12044–12053.

57 A. Penkova, K. Hadjiivanov, M. Mihaylov,
    M. Daturi, J. Saussey and J. C. Lavalley,
    Langmuir, 2004, **20**, 5425–5431.

58 A. Davydov, *Molecular Spectroscopy of Oxide
    Catalyst Surfaces*, Wiley, Chichester, 2003.

59 X. Zhang, H. Wang, L. Meng, X. Nie and Z. Qu,
    ACS Appl. Energy Mater., 2020, **3**, 3465–3476.

60 E. K. Dann, E. K. Gibson, R. H. Blackmore,
    C. R. A. Catlow, P. Collier, A. Chutia, T. E. Erden,
    C. Hardacre, A. Kroner, M. Nachtegaal, A. Raj,
    S. M. Rogers, S. F. R. Taylor, P. Thompson,
    G. F. Tierney, C. D. Zeinalipour-Yazdi, A. Goguet
    and P. P. Wells, *Nat. Catal.*, 2019, **2**, 157–163.

61 M. Jabłońska,
    ChemCatChem, 2020, **12**, 4490–4500.

62 R. E. Weston and T. F. Brodasky,
    J. Chem. Phys., 1957, **27**, 683–689.

63 F. Giordanino, E. Borfecchia, K. A. Lomachenko,
    A. Lazzarini, G. Agostini, E. Gallo, A. V. Soldatov,
    P. Beato, S. Bordiga and C. Lamberti, *J. Phys.
    Chem. Lett.*, 2014, **5**, 1552–1559.

64 H. Zhu, J. H. Kwak, C. H. F. Peden and J. Szanyi,
    Catal. Today, 2013, **205**, 16–23.

65 H. Sjövall, E. Fridell, R. J. Blint and L. Olsson,
    Top. Catal., 2007, **42**–**43**, 113–117.

66 A. L. Goodman, G. M. Underwood and
    V. H. Grassian,
    J. Phys. Chem. A, 1999, **103**, 7217–7223.

67 J. Baltrusaitis, J. Schuttlefield, J. H. Jensen and
    V. H. Grassian, *Phys. Chem. Chem. Phys.*, 2007, **9**,
    4970–4980.

68 T. Yu, T. Hao, D. Fan, J. Wang, M. Shen and W. Li,
    J. Phys. Chem. C, 2014, **118**, 6565–6575.

69 M. Moreno-González, R. Millán, P. Concepción,
    T. Blasco and M. Boronat,
    ACS Catal., 2019, **9**, 2725–2738.

70 L. Olsson, H. Sjövall and R. J. Blint, *Appl. Catal. B
    Environ.*, 2009, **87**, 200–210.

71 C. Paolucci, A. A. Parekh, I. Khurana,
    J. R. Di Iorio, H. Li, J. D. Albarracin Caballero,
    A. J. Shih, T. Anggara, W. N. Delgass, J. T. Miller,
    F. H. Ribeiro, R. Gounder and W. F. Schneider,
    J. Am. Chem. Soc., 2016, **138**, 6028–6048.

72 Y. Zhang, Y. Peng, K. Li, S. Liu, J. Chen, J. Li,
    F. Gao and C. H. F. Peden,
    ACS Catal., 2019, **9**, 6137–6145.

73 C. Paolucci, A. A. Verma, S. A. Bates,
    V. F. Kispersky, J. T. Miller, R. Gounder,
    W. N. Delgass, F. H. Ribeiro and W. F. Schneider,
    Angew. Chem. Int. Ed., 2014, **53**, 11828–11833.

74 M. P. Ruggeri, I. Nova and E. Tronconi,
    Top. Catal., 2013, **56**, 109–113.

75 L. Chen, T. V. W. Janssens, P. N. R. Vennestrøm,
    J. Jansson, M. Skoglundh and H. Grönbeck,
    ACS Catal., 2020, **10**, 5646–5656.

76 C. Tyrsted, E. Borfecchia, G. Berlier,
    K. A. Lomachenko, C. Lamberti, S. Bordiga,
    P. N. R. Vennestrøm, T. V. W. Janssens, H. Falsig,
    P. Beato and A. Puig-Molina,
    Catal. Sci. Technol., 2016, **6**, 8314–8324.

77 L. Ma, Y. Cheng, G. Cavataio, R. W. McCabe, L. Fu
    and J. Li, *Appl. Catal. B Environ.*, 2014, **156**–**157**,
    428–437.

78 H. Sjövall, R. J. Blint and L. Olsson,
    Appl. Catal. B Environ., 2009, **92**, 138–153.

79 M. Bendrich, A. Scheuer, R. E. Hayes and
    M. Votsmeier, *Appl. Catal. B Environ.*, 2018, **222**,
    76–87.

80 H. Mahzoul, J. F. Brilhac and P. Gilot,
    Appl. Catal. B Environ., 1999, **20**, 47–55.

4

CHAPTER

5

A

Summary and Outlook

Summary

Combustion of diesel fuel at high temperatures in an automotive engine leads to the formation of NO_x which is harmful to the environment. To meet environmental regulations, an efficient emission control system is necessary to control and prevent tailpipe NO_x emissions in cars and trucks. The Selective Catalytic Reduction (SCR) reaction is a promising technique to eliminate these NO_x emissions, where NH_3 is used to reduce NO_x into N_2 and H_2O. In practice, hydrothermally robust catalysts are needed since the catalysts must survive the harsh hydrothermal tailpipe environment during the vehicle lifetime. Cu-exchanged zeolites show a relatively high NH_3-SCR activity over a wide temperature range of 150 to 550 °C. Due to its superior hydrothermal stability, the small pore zeolite Cu-SSZ-13 has been commercially implemented in the NH_3-SCR unit of diesel vehicle emission control systems. However, higher activities at lower temperatures (~150 °C) are now required to meet increasingly strict regulations. To optimize state-of-the-art catalysts, fundamental insights into the reaction mechanism and deactivation pathways are required. Although the reaction mechanism of NH_3-SCR has been studied for vanadium oxide-based catalysts, applied in stationary power plants for NO elimination, recent studies indicate alternative reaction pathways on Cu-exchanged zeolites. The diversity and dynamics of Cu speciation brings about a more complex reaction system in Cu-exchanged zeolites, such that the functions of different structural moieties are more difficult to identify. Under real world operational conditions, catalysts work in a harsh hydrothermal environment leading to catalyst deterioration. Loss of activity and the occurrence of undesired side reactions take place on the aged catalysts.

In this PhD Thesis, the structural properties of the fresh and hydrothermally aged Cu-exchanged zeolites as NH_3-SCR catalysts are investigated in detail using ex-situ/operando spectroscopic, microscopic, and microspectroscopic methods including Scanning Transmission X-ray Microscopy (STXM), Atom Probe Tomography (APT), UV-Visible Diffuse Reflectance Spectroscopy (UV-Vis DRS) and Diffuse Reflectance Infrared Fourier-Transform Spectroscopy (DRIFTS). Combined with other conventional lab-based techniques, structure-performance relationships are established, and the mechanistic implications of structural changes of the catalyst on NH_3-SCR are revealed as well.

In **Chapter 1**, an introduction of the NH_3-SCR reaction is provided, explaining the basic concept of the reaction and the catalytic process when using Cu-

exchanged zeolites as catalysts. This Chapter starts with a general introduction of heterogeneous catalysis and zeolites catalysts, followed by the description of commercial NO_x elimination system in vehicle tailpipes. The functions of structure moieties, reaction mechanisms and deactivation pathways of Cu-exchanged zeolites are the main focuses in this Chapter, because further improving catalytic activity and durability requires fundamental understanding of the catalytic process at the molecular level. Currently, although intensive research has been performed on this topic, no consensus has been made on the structure of active sites and reaction pathways due to the variation of Cu species in the catalysts. Therefore, characterization techniques with high spatial resolutions, such as STXM and APT, are necessary to be employed to extend our insights of the working principals of the Cu-exchanged zeolites. A brief introduction of STXM and APT techniques is also given.

In **Chapter 2**, fresh and aged Cu-exchanged zeolites with framework structures of CHA and MFI were studied to elucidate the key deactivation mechanisms for the NH_3-SCR reaction. STXM was employed to obtain two-dimensional chemical maps of Al and Cu, where abundant local information about the Al coordination environment and Cu formal oxidation state is provided by Al K-edge and Cu L-edge X-ray Absorption Near-Edge Structure (XANES) spectra. The same steaming condition induced a comparable level of dealumination in both Cu-CHA and Cu-MFI such that around 10% of framework Al degraded into octahedral and tri-coordinated Al. However, the NH_3-SCR activity was largely maintained in the steamed Cu-CHA, stressing the importance of preserving Cu^{2+} active sites. Multiple Cu species were detected in the aged zeolite Cu-MFI, where Cu^+ and Cu_xO_y were formed, with little remaining isolated Cu^{2+}. Spatial heterogeneity was only observed in the aged zeolite Cu-MFI from the Al and Cu chemical maps containing single-pixel XANES spectra. A spatial correlation was found between the extra-framework Al, Cu^+ and Cu_xO_y zoned on the surface (~250 nm) of individual particles of aged Cu-MFI. While in the main body of each catalyst particle, tri-coordinated Al and Cu^+ were correlated, indicating a change in the interaction between Al and Cu species during the simulated aging process. The NH_3-SCR active catalysts including Cu-CHA-fresh, Cu-CHA-aged and Cu-MFI-fresh showed a homogenous distribution of both Al and Cu species. However, because the spatial resolution of the STXM experiments performed in this Chapter is 50 nm, a detailed spatial analysis of the Cu-CHA zeolites was limited by the small single particle size of ~250 nm. In this Chapter, it is concluded that the loss of isolated Cu^{2+} is detrimental to the NH_3-SCR reaction and Cu species tend to agglomerate and migrate during the simulated aging process.

5

In **Chapter 3**, the distribution and location of Al and Cu were investigated in a simulated 135,000-mile vehicle aged NH_3-SCR catalyst zeolite Cu-SSZ-13 by a correlated APT-STXM experiment. A single Cu-SSZ-13 cubic crystal of ~4 μm was thinned to ~0.5 μm using Focused Ion Beam (FIB) milling to allow for sufficient X-ray transmission through the material. After performing the STXM experiment, the sample was milled into a needle for the subsequent APT experiment with sub-nanometer resolution. Analysis of STXM-XANES spectra showed a more severe dealumination in the center of the zeolite crystal where Al concentration was higher. Meanwhile, the analyzed APT needle, coming from the severely dealuminated area revealed by STXM-XANES results, showed a significant Al-Al affinity. The combined APT-STMX results indicated that the dealumination of zeolite Cu-SSZ-13 lead to Al zoning at a sub-nanometer scale. The biggest challenge of correlating APT and STXM is the disconnection in resolution between these two techniques. The STXM analyzed area in this Chapter is ~30 times larger than that of the APT experiment, while the resolution is at least 50 times lower in STXM. Therefore, it is difficult to have STXM spatial resolution within an APT needle, as the STXM pixel size is approximately the size of an APT needle diameter. But overall, the heterogeneity of Al can be found at length scales of a micrometer to tens of nanometers in the correlated APT-STXM study.

In **Chapter 4**, an operando spectroscopic study was performed on a series of fresh and steamed Cu-ZSM-5 zeolites. An unusual catalytic behavior was observed in the steamed Cu-ZSM-5, such that a 'dip' at around 275 °C was observed in the NO conversion curve. A maximum in the NH_3 conversion was also found at the same reaction temperature. The unbalanced consumption of NO and NH_3 at the standard NH_3-SCR condition clearly indicated the occurrence of undesired side reactions, most importantly the unselective NH_3 oxidation at a reaction temperature higher than 250 °C. This observation reinforces that side reactions and the formation of undesired reaction products are inevitable with aging catalysts at operational conditions in the automotive emission control system. The main structural reason for the promotion of unselective NH_3 oxidation reaction is usually ascribed to the aggregation of Cu, and specifically in this Chapter, a $[Cu_x(OH)_{2x-1}]^+$ oligomer/cluster is postulated to be the structure that participated in the undesired NH_3 oxidation reaction in the steamed Cu-ZSM-5. Structure-intermediate-performance relationships were elucidated by operando UV-Vis DRS and DRIFTS. In fresh Cu-ZSM-5, NH_3 was found to preferentially associate with Cu^{2+} at a low reaction temperature (<250 °C) while framework O^{2-} was more favorable for the high temperature (>300 °C) reaction. Isolated Cu^{2+}

was the active site for the NH$_3$-SCR reaction where competitive adsorption of NH$_3$ and nitrates took place. Octahedral Cu^{2+} with a coordination number of six was found throughout the NH$_3$-SCR reaction process, maintaining the high surface coverage of nitrate intermediates. However, pseudo-tetrahedral Cu^{2+} with associated NH$_3$ and nitric acid on the surface of [Cu$_x$(OH)$_{2x-1}$]$^+$ oligomers/ clusters was more prevalent in the most severely steamed Cu-ZSM-5 zeolites, but this structure limited the low-temperature NH$_3$-SCR reaction. With increasing reaction temperature, the relaxation of this distorted structure by the removal of coordinated NH$_3$ and the fast oxidation of NH$_3$ led to the undesired NH$_3$ oxidation reaction. In both fresh and steamed Cu-ZSM-5 zeolites, reaction between surface NO$_3^-$ and NO governed the nitrate-nitrite equilibrium and avoided surface blockage.

Future Perspectives

As diesel vehicles are still dominant in the market and expected to remain so due to shortcomings of electric vehicles to replace heavy duty applications, regulations of the NO$_x$ emissions from vehicle engines will remain paramount in the near future for air quality protection.[1] To meet ever stricter regulations, the NH$_3$-SCR module in automotive emission control system must have high activity and durability. Although the Cu-exchanged zeolite CHA has been practically implemented, its low-temperature activity and durability need to be improved to meet the '150 °C challenge' that 90 % of pollutants must be reduced at 150 °C, which is practically important at cold start conditions.[2]

Heterogeneity is the distinct feature of Cu-exchanged zeolites according to **Chapter 2-4** in this PhD Thesis, where zoning of Cu could be found at nano- and sub-nano scale. Multiple Cu species, including isolated Cu^{2+} and [CuOH]$^+$, were detected in the fresh Cu-exchanged zeolites, while upon simulated aging, Cu$^+$ and aggregation of Cu into Cu$_x$O$_y$, CuAl$_x$O$_y$ and [Cu$_{2x}$(OH)$_{2x-1}$]$^+$ oligomers/ clusters/nanoparticles were also found. Even in the fresh Cu-exchanged zeolites, the industrial production can also generate heterogeneity, for instance local Al zoning originating from defects in zeolite crystals, and Cu agglomeration in zeolites with a high Cu loading. The isolated Cu^{2+} as an active redox center attracts most of the attention in studies of the NH$_3$-SCR reaction. However, the heterogeneity of Cu^{2+} speciation makes it challenging to study this complex redox system to elucidate the reaction mechanism and deactivation pathways due to the entangling of multiple reactions under operational reaction conditions.

5

Uniform Cu speciation is beneficial to understand the reaction mechanism of NH_3-SCR. Cu-exchanged zeolites with a single Cu species could be obtained by controlling the concentration and location of Al in zeolites, which determines the type and location of isolated Cu^{2+}. The distribution of Al has been successfully controlled in various types of zeolites such as CHA and MFI by tuning the types and ratio of organic/inorganic Structure Directing Agents (SDA).[3,4] When N,N,N-trimethyl-1-admantylammonium cations (TMAda$^+$) are the only SDA in the precursor solution, zeolite chabazite with only isolated Al sites is synthesized, whose charge cannot be balanced by the divalent Cu^{2+}, but instead the monovalent $[CuOH]^+$.[3] Tuning the TMAda$^+$/Na$^+$ ratio in the crystallization medium changes the density of Al pairs where the Cu^{2+} is exchanged. The Al location can also be controlled by the types of SDAs used, for example Al atoms preferentially sit in the sinusoidal channels when using the branched-chain alcohol trimethylolethane as the SDA in zeolite ZSM-5 synthesis.[4] Cu species in structurally well-defined zeolites have a more understandable structure that simplifies reaction mechanism studies.

The heterogeneities found in the Cu-exchanged zeolites in this PhD Thesis also reflect potential practical problems. Therefore, possible suggestions are provided here for further improvements of the automotive emission control system. First of all, catalysts with higher hydrothermal stability must be pursued to match the long lifetime of vehicles. Although Cu-ZSM-5 and Cu-Beta were discovered earlier due to their outstanding performance in the low temperature NH_3-SCR reaction, they are not promising catalysts for practical use because of their relatively poor hydrothermal stability. The more hydrothermally robust zeolite Cu-SSZ-13 with the CHA framework structure was more recently adapted for the automotive emission control system since it was discovered to be NH_3-SCR active.[5] The hydrothermal stability of the small pore zeolite Cu-SSZ-13 can be further enhanced by tuning Si/Al ratio and Cu loading. As indicated in **Chapter 2**, the aggregation of Cu is more detrimental to the NH_3-SCR reaction compared to local destruction of the zeolite framework. Therefore, Cu loading should be carefully optimized to avoid the agglomeration of Cu. Over exchange of Cu^{2+} is not advised due to its higher probability to form Cu_xO_y nanoparticles. Instead, ion exchange levels of ~40-70% have been suggested.[6,7] Besides, bare Cu^{2+} is favored to maintain the framework structure compared to $[CuOH]^+$ with a lower hydrothermal stability. For this reason, Al pairs in the zeolite framework are required, which can be achieved by controlled synthesis of zeolites or lowing the Si/Al ratio. However, it should be noted that compared to the bare Cu^{2+}, the redox-active $[CuOH]^+$ is more beneficial for the low temperature NH_3-SCR

reaction. Therefore, the amount of Cu^{2+}, $[CuOH]^+$ and Brønsted acid sites should be optimized to maximize the hydrothermal stability without sacrificing NH_3-SCR activity.
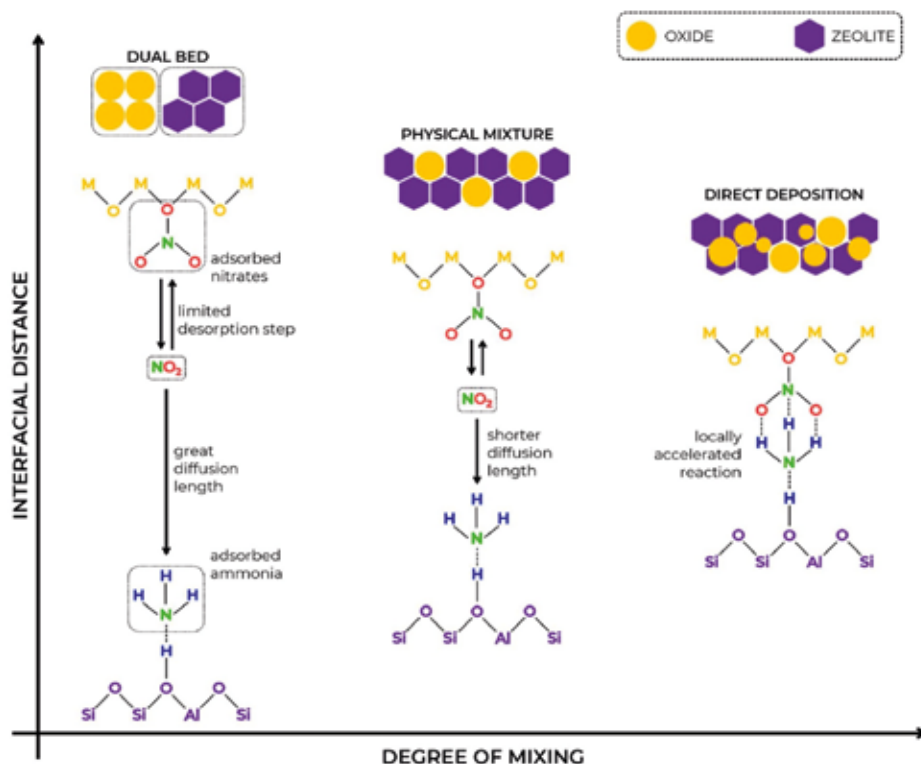
Figure 5.1 Schematic of NO_2 diffusion distance as a function of the degree of mixing of metal oxide-based Selective Catalytic Oxidation (SCO) catalysts and zeolite-based NH_3-Selective Catalytic Reduction (SCR) reaction catalysts.[2] Copyright 2021 Elsevier.

Aging of the Cu-exchanged zeolites is a permanent process that is inevitable in the automotive emission control system because of the frequent exposure to high temperature steam. According to **Chapter 4**, NO_2 and HNO_3 were observed at a reaction temperature of 250 °C, and an unselective NH_3 oxidation reaction occurred during the high temperature NH_3-SCR reaction over the steamed zeolites. It suggested that NO cannot be completely removed at a low reaction temperature (<250 °C), and other undesired byproducts including NO_2 and HNO_3 can also come from the NH_3-SCR unit if the catalyst is not resistant to aging. Therefore, a trace amount of NO_x and HNO_x need to be treated after the NH_3-SCR unit. Alkaline metal oxide based Lean NO_x Trap (LNT) catalysts that can trap

NO/NO$_2$ and react with HNO$_3$ could be coupled after the NH$_3$-SCR unit for the further removal of residual, undesired NO$_x$. However, considering the high cost and bulky size of the emission control system, suitable amounts of LNT catalysts could coat the ceramic monolith together with NH$_3$-SCR catalysts, and be placed close to the outlet of the NH$_3$-SCR unit.

Improvement of the low-temperature NH$_3$-SCR performance must also be emphasized. The exhaust temperature of a lean-burn engine is estimated to be 150 °C lower with increasing fuel efficiency.[8] However, the NO cannot be completely removed at the low temperature of 150 °C using fresh Cu-exchanged zeolites as indicated in **Chapter 2**. One of the promising strategies to overcome this is to promote the occurrence of the fast SCR reaction which requires an equimolar ratio of NO/NO$_2$. The state-of-the-art Diesel Oxidation Catalysts (DOC) in the upstream of the NH$_3$-SCR unit can oxidize NO to NO$_2$ in order to promote the reaction rate of the NH$_3$-SCR reaction. Another possible approach aims to improve the low temperature activity by coupling metal oxide-based Selective Catalytic Oxidation (SCO) catalysts and zeolite-based NH$_3$-SCR catalysts.[2] The NO oxidation reaction takes place on SCO catalysts, providing NO$_2$ for the subsequent fast NH$_3$-SCR reaction. However, the conversion of NO on the SCO catalysts must be well controlled because an excessive amount of NO$_2$ can decrease the reaction rate by following the slow NH$_3$-SCR reaction. Therefore, the types and ratio of SCO and NH$_3$-SCR catalysts need to be carefully selected. In addition, the proximity of oxides and zeolites can be tuned by the catalyst packing as indicated in Figure 5.1, i.e., dual bed packing, physical mixtures or direct deposition. Each method changes the diffusion distance of NO$_2$ and thus the overall reaction rate. Currently, commercial application of this oxide-zeolite coupling concept still requires further investigations.

Conclusions

Isolated Cu^{2+} in the Cu-exchanged zeolites has been demonstrated to be responsible for the NH$_3$-SCR reaction. The simulating aging (steaming) of the catalysts in the automotive emission control system results in heterogeneity of both Al and Cu species in the Cu-exchanged zeolites. It is common to find the degradation of tetrahedral framework Al into octahedral and tri-coordinated Al and the loss of isolated Cu^{2+} in the aged catalysts, and the latter is most detrimental to the NH$_3$-SCR reaction. Upon steaming, Cu$^+$, Cu$_x$O$_y$, CuAl$_x$O$_y$ nanoparticles and probably [Cu$_x$(OH)$_{2x-1}$]$^+$ oligomers/clusters can be formed, accompanied by the migration of Cu species to the surface of catalyst particles due to changes of the interaction between Al and Cu. With the aggregation of

Cu, the undesired, unselective NH_3 oxidation reaction occurs in the steamed zeolites, causing the dramatic decrease of NO conversion and the formation of byproducts such as NO_2 and HNO_3. Changes of Cu speciation from the simulated aging procedure also change the coordination of Cu^{2+} with reactants and intermediates. The accumulation of the more distorted pseudo-tetrahedral Cu^{2+} coordinating with NH_3 and surface nitric acid might limit the low temperature NH_3-SCR reaction. Practical suggestions can be made from the studies in this PhD Thesis. A more hydrothermally robust zeolite structure is needed to stabilize the isolated Cu^{2+}, and a post NH_3-SCR treatment might be needed as well to treat the trace amount of undesired harmful byproducts generated from the aged NH_3-SCR catalysts.

REFERENCES

1   E. Borfecchia, P. Beato, S. Svelle, U. Olsbye, C. Lamberti and S. Bordiga, *Chem. Soc. Rev.*, 2018, **47**, 8097–8133.

2   T. Andana, K. G. Rappé, F. Gao, J. Szanyi, X. Pereira-Hernandez and Y. Wang, *Appl. Catal. B Environ.*, 2021, **291**, 120054.

3   J. R. Di Iorio and R. Gounder, *Chem. Mater.*, 2016, **28**, 2236–2247.

4   T. Biligetu, Y. Wang, T. Nishitoba, R. Otomo, S. Park, H. Mochizuki, J. N. Kondo, T. Tatsumi and T. Yokoi, *J. Catal.*, 2017, **353**, 1–10.

5   F. Gao and C. Peden, *Catalysts*, 2018, **8**, 140.

6   F. Gao and J. Szanyi, *Appl. Catal. A Gen.*, 2018, **560**, 185–194.

7   J. H. Kwak, D. Tran, J. Szanyi, C. H. F. Peden and J. H. Lee, *Catal. Letters*, 2012, **142**, 295–301.

8   F. Gao, Y. Wang, N. M. Washton, M. Kollár, J. Szanyi and C. H. F. Peden, *ACS Catal.*, 2015, **5**, 6780–6791.

5

CHAPTER 5 **B**

Samenvatting

Samenvatting

De ontbranding van diesel in automotoren vindt plaats bij hoge temperatuur wat leidt tot de vorming van schadelijke NO_x gassen (NO en NO_2). Om te voorkomen dat deze gassen worden uitgestoten wordt er bij moderne autos en vrachtwagens gebruik gemaakt van een emissiecontrole systeem, waarin NO_x wordt omgezet naar minder schadelijke gassen. De Selectieve Katalytische Reductie (SKR) reactie is een veelbelovende reactie waarbij NH_3 wordt gebruikt om NO_x te reduceren naar N_2 en H_2O. Voor toepassing van deze techniek in de praktijk zijn robuuste katalysatoren nodig, bestand tegen hoge temperaturen en aanwezigheid van stoom tijdens de gehele levensduur van de auto. Koperhoudende zeolieten zijn interessante katalysatoren en hebben een relatief hoge NH_3-SKR activiteit over een breed temperatuurbereik van 150 °C tot 550 °C. De Cu-SSZ-13 katalysator is gebaseerd op zeoliet met kleine poriën (kleiner dan 0.4 nm) en wordt dankzij een goede stabiliteit tegen hoge temperaturen en stoom, succesvol toegepast in commerciële emissie controle systemen. Echter, om tegemoet te komen aan toekomstige strengere emissie eisen is, onder andere, een verdere verbetering van de SKR activiteit bij lage temperaturen noodzakelijk.

Voor de ontwikkeling van huidige en toekomstige generaties NH_3-SKR katalysatoren zijn fundamentele inzichten in het reactie- en deactivatiemechanisme nodig. Hoewel het reactiemechanisme van NH_3-SKR reeds bekend is voor vanadiumoxide katalysatoren die - bijvoorbeeld - toegepast worden in schoorstenen van energiecentrales, suggereren recente studies alternatieve reactiemechanismes voor koperhoudende zeolieten. De diversiteit en dynamiek van de koperspeciatie in koperhoudende zeolieten leiden tot een complex katalytisch systeem, waarin de verschillende structurele eigenschappen lastig te identificeren zijn. Daarnaast werken NH_3-SKR katalysatoren bij hoge temperatuur en in aanwezigheid van stoom, zogenaamde 'hydrothermische' condities, wat de koperspeciatie verder beïnvloedt. Veroudering van de NH_3-SKR katalyator leidt tot verlies van de katalytische activiteit en ongewenste nevenreacties.

In deze PhD dissertatie worden relaties gelegd tussen de structuur en prestatie van nieuwe en verouderde katalysatoren, door gebruik te maken van ex-situ/operando spectroscopische, microscopische en microspectroscopische methoden. Technieken die gebruikt worden zijn, transmissie Röntgenmicroscopie (Scanning Transmission X-ray Microscopy, STXM), Atoomprobe tomografie (Atom Probe Tomography, APT), Ultraviolet en zichtbaar licht diffuse reflectie spectroscopie (UV-Visible Diffuse Reflectance Spectroscopy, UV-Vis DRS)

en Diffuse reflectie infrarood spectroscopie (Diffuse Reflectance Infrared Fourier-Transform Spectroscopy, DRIFTS). Gecombineerd met resultaten van conventionele lab technieken, worden relaties gelegd tussen de structuur en de prestatie van de onderzochte katalysatoren. Daarnaast worden ook de implicaties van veroudering van de katalysator op het reactiemechanisme bestudeerd.

In **Hoofdstuk 1** wordt een algemene inleiding gegeven over katalyse, zeolieten en wordt de NH_3-SKR reactie geïntroduceerd voor koperhoudende zeolieten als katalysator. Verschillende soorten commerciële NH_3-SKR systemen, die toegepast worden in auto's en vrachtwagens, worden beschreven. Het belangrijkste onderdeel van de inleiding is de functie van de verschillende onderdelen van de structuur van de katalysatoren, en hun rol in reactie-en deactivatiemechanisme. Om de activiteit en stabiliteit van de huidige generatie katalysatoren te verbeteren is fundamentele kennis nodig van de katalytische reacties op moleculair niveau. Op dit moment zijn de toekenning van de actieve sites en reactie mechanisms voor NH_3-SKR met koperhoudende zeolieten niet algemeen geaccepteerd. Dit wordt voornamelijk veroorzaakt door de verschillende verschijningsvormen van koper onder reactiecondities. Om die reden zijn geavanceerde karakterisatietechnieken nodig - zoals STXM en APT – waarmee nieuwe inzichten verkregen kunnen worden over de structuur van de katalysator op de nanoschaal en sub-nanoschaal. Een korte inleiding van de STXM en APT technieken maakt ook deel uit van dit hoofdstuk.

In **Hoofdstuk 2** worden nieuwe en verouderde koperhoudende zeolieten met CHA en MFI structuren bestudeerd om deactivatiemechanismes te bestuderen. STXM werd gebruikt om twee dimensionale visualisaties te maken van de elementen Al en Cu. Lokale informatie over de Al coordinatie en Cu oxidatie toestand werd verkregen door Al K-edge en Cu L-edge X-ray Absorption Near-Edge Structure (XANES) spectra. Stoombehandelingen veroorzaakten een vergelijkbaar niveau van dealuminatie in zowel Cu-CHA als Cu-MFI. Ongeveer 10 % van het voormalig intrakristallijn Al was octaëdrisch en tri-gecoordineerd na de stoombehandeling. Echter, de NH_3-SKR activiteit was stabiel in de gestoomde Cu/CHA katalysator, wat het belang van het behouden van Cu^{2+} als actieve component bevestigd. Meerdere Cu soorten werden vastgesteld in de verouderde Cu/MFI katalysatoren, onder andere Cu^+ en Cu_xO_y en slechts weinig geisoleerd Cu^{2+}. Ruimtelijke heterogeniteit van de verschillende Cu soorten werd alleen vastgesteld in de verouderde zeoliet Cu/MFI. Een ruimtelijke correlatie werd gevonden tussen extra-framework Al, Cu^+, and Cu_xO_y die selectief aanwezig

5

waren aan het oppervlak (~250 nm) van individuele deeltjes van verouderd Cu/MFI. Terwijl in het midden van elk katalysatordeeltje, tri-gecoordineerd Al en Cu$^+$ konden worden gecorreleerd, indicatief voor een verandering in de interactie tussen Al en Cu soorten tijdens het gesimuleerde verouderings proces. Nieuw en verouderd Cu/CHA en nieuw Cu/MFI vertoonden een homogene verdeling van zowel Al als Cu soorten. Echter, omdat de ruimtelijke resolutie van de STXM experimenten uitgevoerd in dit hoofdstuk 50 nm is, werd een gedetaileerde analyse van de Cu-CHA zeolieten beperkt bij de kleine deeltjes grootte van ~250 nm. In dit hoofdstuk werd het geconcludeerd dat het verlies van geisoleerd Cu^{2+} schadelijk is voor de NH$_3$-SCR reactie en Cu soorten de neiging hebben om te agglomereren en migreren tijdens het gesimuleerde verouderings proces.

In **Hoofdstuk 3** werden de verdeling en locatie van Al en Cu onderzocht in een gecorreleerd APT-STXM experiment voor een verouderde Cu-SSZ-13 katalysator. Deze katalysator was verouderd in een simulatie experiment en was overeenkomstig met een katalysator die voor 217.000 km gebruikt is in een emissie controle systeem. Een enkel kubisch kristal van Cu-SSZ-13 van ~4 μm werd verdund tot ~0.5 μm met behulp van etsing door een gefocuste ionenbundel (Focused Ion Beam, FIB) zodat voldoende Röntgen transmissie door het materiaal werd bewerkstelligd. Na het uitvoeren van het STXM experiment werd het sample gemalen tot een naald voor het daaropvolgende APT experiment. Analyse van de STXM-XANES spectra vertoonden meer vergaande dealuminatie in het centrum van het zeoliet kristal waar de Al concentratie hoger was. Bij analyse van de APT naald werd een significante Al-Al affiniteit aangetoond, komend van de vergaande dealuminatie. De gecombineerde APT-STXM resultaten toonden aan dat de dealuminatie van het zeoliet Cu-SSZ-13 leidde tot lokaal verhoogde concentraties van Al. De grootste uitdaging van het correleren van APT en STXM is het in acht nemen van de verschillen in resolutie van deze twee technieken. De STXM oppervlak in dit hoofdstuk is ~30 keer groter dan die van het APT experiment terwijl de resolutie in STXM minstens 50 keer lager is. Daarom is het lastig om een STXM ruimtelijke resolutie in een APT naald te hebben, aangezien de STXM pixel grootte ongeveer de grootte heeft van de diameter van een APT naald. Concluderend kan worden gesteld dat de heterogeniteit van Al gevonden kan worden op lengteschalen van micrometers tot tienden van nanometers in de gecorreleerde APT-STXM studie.

In **Hoofdstuk 4** werd een operando spectroscopische studie uitgevoerd op een serie nieuwe en gestoomde Cu-ZSM-5 zeolieten. Bij 275 °C werd een ongebruikelijk katalytisch gedrag geobserveerd in gestoomd Cu-ZSM-5. Er

was een dip zichtbaar in de NO conversie, terwijl er een maximum was in de NH_3 conversie. Deze ongebalanceerde conversie van NO en NH_3 duidde op het bestaan van ongewenste neven reacties, waarvan NH_3 oxidatie de meest cruciale nevenreactie was. Deze reactie vindt plaats bij reactie temperaturen hoger dan 250 °C. Deze observatie bevestigd dat nevenreacties en de vorming van ongewenste reactieproducten onontkoombaar zijn bij verouderde en gestoomde katalysatoren. De reden voor het voorkomen van de NH_3 oxidatie reactie is gewoonlijk toegeschreven aan de aggregatie van Cu. In dit hoofdstuk is een $(Cu_x(OH)_{2x-1})^+$ oligomeer/cluster gepostuleerd als structuur die verantwoordelijk is voor het katalyseren van de NH_3 oxidatie reactie. Structuur-tussenproduct-prestatie relaties werden onderzocht met behulp van operando UV-VIS DRS en DRIFTS. In nieuwe Cu-ZSM-5 katalysatoren bleek NH_3 preferentieel te associëren met Cu^{2+} bij lage reactie temperaturen (<250 °C) terwijl intra-kristallijn O_2^- gunstiger bleek voor de hogere reactie temperaturen (>300 °C). Geïsoleerd Cu^{2+} was de katalytisch actieve site voor de NH_3-SKR reactie waar de NH_3 en nitraten competitief adsorberen. Octaedrisch Cu^{2+}, met een coordinatie nummer van zes werd tijdens de gehele duur van het NH_3-SKR proces gevonden en in alle gevallen met een hoge concentratie van nitraat tussenproducten. Echter, pseudo-tetraedrisch Cu^{2+} met geassocieerd NH_3 en salperterzuur op het oppervlak van $[Cu_x(OH)_{2x-1}]^+$ oligomeren/clusters was meervoorkomend in de meer gestoomde Cu/ZSM-5 zeolieten. Echter, deze structuur was niet actief voor de lage temperatuur NH_3-SKR reacties. Toenemende reactie temperatuur leidde tot een verwijdering van gecoördineerd NH_3 en snelle oxidatie van NH_3. In zowel de nieuwe als de gestoomde Cu/ZSM-5 zeolieten, bepaalden reacties tussen NO_3^- en NO aanwezig op het oppervlak het nitraat-nitraat evenwicht en voorkwamen daardoor blokkage van het oppervlak.

5

A

Appendix

APPENDIX I

List of Publications and Presentations

A. Scientific Publications

New Insights into the NH_3-Selective Catalytic Reduction of NO over Zeolite Cu-ZSM-5 as Revealed by Operando Spectroscopy, X. Ye, R. Oord, M. Monai, J. E. Schmidt, T. Chen, F. Meirer, B. M. Weckhuysen, Catal. Sci. Technol., 2022, 12, 2589-2603.

Deactivation of Cu-Exchanged Automotive-Emission NH_3-SCR Catalysts Elucidated with Nanoscale Resolution Using Scanning Transmission X-ray Microscopy, X. Ye, J. E. Schmidt, R. -P. Wang, I. K. van Ravenhorst, R. Oord, T. Chen, F. M. F. de Groot, F. Meirer, B. M. Weckhuysen, Angew. Chem. Int. Ed., 2020, 59, 15610-15617.

Probing the Location and Speciation of Elements in Zeolites with Correlated Atom Probe Tomography and Scanning Transmission X-Ray Microscopy, J. E. Schmidt, X. Ye, I. K. van Ravenhorst, R. Oord, D. A. Shapiro, Y. -S. Yu, S. R. Bare, F. Meirer, J. D. Poplawsky, B. M. Weckhuysen, ChemCatChem, 2019, 11, 488-494.

Uniformly Oriented Zeolite ZSM-5 Membranes with Tunable Wettability on a Porous Ceramic, D. Fu, J. E. Schmidt, P. Pletcher, P. Karakiliç, X. Ye, C. M. Vis, P. C. A. Bruijnincx, M. Filez, L. D. B. Mandemaker, L. Winnubst, B. M. Weckhuysen, Angew. Chem. Int. Ed., 2018, 57, 12458-12462.

B. Oral Presentations

Nano-resolved X-ray Spectro-microscopic Study on Deactivation of Cu-exchanged Automotive Emissions NH_3-SCR Catalysts, X. Ye, J. E. Schmidt, R. -P. Wang, I. K. van Ravenhorst, R. Oord, T. Chen, F. M. F. de Groot, F. Meirer, B. M. Weckhuysen, International Conference on Environmental Catalysis (ICEC), online, September 2020.

Deactivation of Cu-exchanged Automotive Emissions NH_3-SCR Catalysts Elucidated with X-ray Nano-Spectroscopy, X. Ye, J. E. Schmidt, R. -P. Wang, I. K. van Ravenhorst, R. Oord, T. Chen, F. M. F. de Groot, F. Meirer, B. M. Weckhuysen, 21st Netherlands' Catalysis and Chemistry Conference (NCCC), Noordwijkerhout, The Netherlands, March 2020.

C. Poster Presentations

Insight into Deactivation of NH_3-SCR Catalysts with Nanoscale Resolved X-ray Microscopy, X. Ye, J. E. Schmidt, R. -P. Wang, I. K. van Ravenhorst, R. Oord, T. Chen, F. M. F. de Groot, F. Meirer, B. M. Weckhuysen, 17th International Congress on Catalysis (ICC), online, June 2020.

Probing the Location and Speciation of Elements in Zeolites with Correlated Atom Probe Tomography and Scanning Transmission X-Ray Microscopy, X. Ye, J. E. Schmidt, I. K. van Ravenhorst, R. Oord, D. A. Shapiro, Y. -S Yu, S. R. Bare, F. Meirer, J. D. Poplawsky, B. M. Weckhuysen, 20th Netherlands' Catalysis and Chemistry Conference (NCCC), Noordwijkerhout, The Netherlands, March 2019.

Synthesis of *b*-Oriented Zeolite ZSM-5 Films by *In-situ* Crystallization, X. Ye, D. Fu, J. E. Schmidt, B. M. Weckhuysen, 19th Netherlands' Catalysis and Chemistry Conference (NCCC), Noordwijkerhout, The Netherlands, March 2018.

A

APPENDIX II

List of Abbreviations

AIMD	Ab Initio Molecular Dynamics
APT	Atom Probe Tomography
APFIM	Atom Probe Field Ion Microscopy
ASC	Ammonia Slip Catalyst
DPF	Diesel Particulate Filter
DOC	Diesel Oxidation Catalyst
DOS	Density of States
DRIFTS	Diffuse Reflectance Infrared Fourier Transform Spectroscopy
DRS	Diffuse Reflectance Spectroscopy
EELS	Electron Energy Loss Spectroscopy
EM	Expectation Maximization
EXAFS	Extended X-ray Absorption Fine Structure
FIB	Focused Ion Beam
FIM	Field Ion Microscopy
FOV	Field of View
FT-IR	Fourier Transform Infrared
FTS	Fischer-Tropsch Synthesis
GHSV	Gas Hourly Space Velocity
GMM	Gaussian Mixture Modeling
H_2-TPR	Hydrogen Temperature Programmed Reduction
ICP-OES	Inductively Coupled Plasma Optical Emission Spectroscopy
LEAP	Local Electrode Atom Probe
LNT	Lean NO_x Trap
LSLC	Least-Square Linear Combination

MAS ssNMR	Magic Angle Spinning Solid-state Nuclear Magnetic Resonance
MR	Membered Ring
MCT	Mercury-Cadmium-Telluride
MTH	Methanol to Hydrocarbons
NH_3-SCR	Selective Catalytic Reduction with Ammonia
NH_3-TPD	Ammonia Temperature Programmed Desorption
NND	Nearest Neighbor Distribution
NO_x	Nitrogen Oxides
OD	Optical Density
OSA	Order Sorting Aperture
PCA	Principal Component Analysis
PXRD	Powder X-Ray Diffraction
rR	resonance Raman
RDF	Radical Distribution Function
SCO	Selective Catalytic Oxidation
SDA	Structure Directing Agent
SEM	Scanning Electron Microscopy
STXM	Scanning Transmission X-ray Microscopy
TCD	Thermal Conductivity Detector
TEM	Transmission Electron Microscopy
UV-Vis DRS	Ultra Violet-Visible Diffuse Reflectance Spectroscopy
XANES	X-ray Absorption Near-Edge Structure
XAS	X-ray Absorption Spectroscopy
ZP	Zone Plate

A

APPENDIX III

A. Additional Figures and Tables of Chapter 2
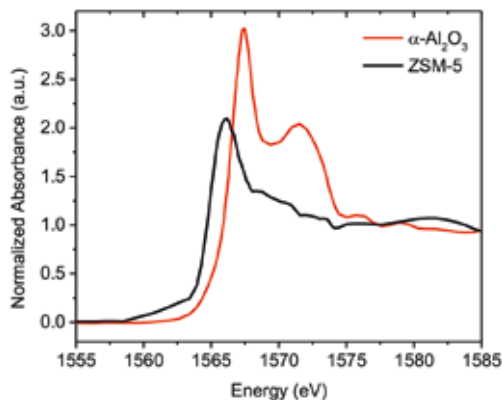
Figure AIII1. Al K-edge X-ray Absorption Near-Edge Structure (XANES) spectra of references (zeolite ZSM-5: tetrahedral Al, α-Al$_2$O$_3$: octahedral Al). Data was previously collected by our group. The edge positions of the Al K-edge XANES of tetrahedral and octahedral Al exhibit a shift of ~1.3 eV between each other. Furthermore, because of the higher geometric symmetry of the octahedral structure, the XANES of octahedral Al, represented by α-Al$_2$O$_3$, also shows stronger absorption in the near-edge region accompanied by a double peak structure with a peak separation of about 4 eV. These distinct spectral features are therefore commonly used to distinguish tetrahedral Al and octahedral Al.
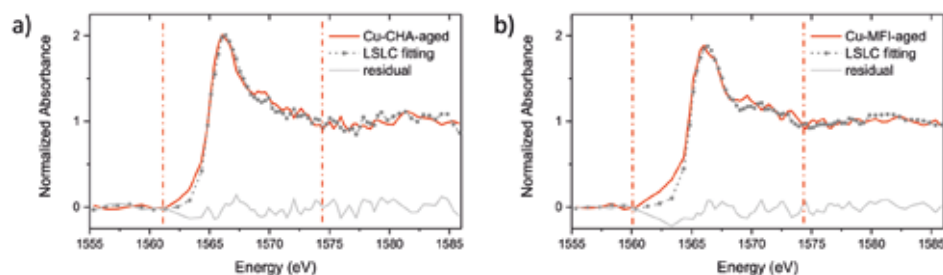
Figure AIII2. Least-Square Linear Combination (LSLC) fitting of Al K-edge Absorption Near-Edge Structure (XANES) spectra of a) Cu-CHA-aged and b) Cu-MFI-aged. Zeolite ZSM-5 and α-Al$_2$O$_3$ were used as references. Fitting range: 1560.35 to 1574.35 eV indicated by red dot-dash lines. Results showed that the Cu-CHA-aged and Cu-MFI-aged had a comparable amount of octahedral Al.

Table AIII1. Quantitative analysis of Al species in fresh and aged Cu-exchanged zeolites.

	$(Al_{Td} + 3\text{-fold Al})/\%$[a]	$Al_{Oh}/\%$[a]	Integral pre-edge area[b]
Cu-CHA-fresh	100	0	N.D.
Cu-MFI-fresh	100	0	N.D.
Cu-CHA-aged	87.3±1.2	12.7±1.2	0.36
Cu-MFI-aged	90.2±1.4	9.8±1.4	0.56

[a] Determined by Least-Square Linear Combination (LSLC) fitting of Al K-edge X-ray Absorption Near-Edge Structure (XANES) spectra using zeolite ZSM-5 and $\alpha\text{-Al}_2O_3$ as tetrahedral and octahedral Al references, respectively, and a fitting range from 1560.35 to 1574.35 eV.
[b] Integral of the pre-edge region of 1560.35-1565.15 eV, representing tri-coordinated (3-fold) Al.

Table AIII2. Cu L_3-edge peak information of Cu-exchanged zeolites CHA and MFI.

	Cu^{2+} L_3-edge/eV	Cu^+ L_3-edge/eV	$Cu^+/\%$
Cu-CHA-fresh	931.5	935.2	6
Cu-CHA-aged	931.4	935.1	13
Cu-MFI-fresh	931.2	934.9	8
Cu-MFI-aged	931.0	935.0	36

Table AIII3. Relative amounts of Al_{Oh}, tri-coordinated Al and Cu^+ of clusters Surface 1-4 in zeolite Cu-MFI-aged.

	$Al_{Oh}/\%$[a]	Integral pre-edge area[b]	$Cu^+/\%$[c]
Surface 1	12±2.3	1.14	49
Surface 2	12.1±2.2	1.02	45
Surface 3	10.7±2.2	1.00	41
Surface 4	14.6±2.2	0.73	35

[a] Determined by Least-Square Linear Combination (LSLC) fitting of Al K-edge X-ray Absorption Near-Edge Structure (XANES) spectra using zeolite ZSM-5 and $\alpha\text{-Al}_2O_3$ as tetrahedral and octahedral Al references, respectively, and a fitting range from 1560.35 to 1574.35 eV.
[b] Integral of the pre-edge region of 1560.35-1565.15 eV, representing tri-coordinated (3-fold) Al.
[c] Determined by peak area of Cu^{2+} and Cu^+ edge from Cu L_3-edge XANES.

A

Table AIII4. Relative amounts of Al_{Oh}, tri-coordinated Al and Cu^+ of clusters Center 1-5 in zeolite Cu-MFI-aged.

	$Al_{Oh}/\%$[a]	Integral pre-edge area[b]	$Cu^+/\%$[c]
Center 1	11.2±1.6	0.13	31
Center 2	9.7±1.3	0.25	34
Center 3	9.0±1.3	0.3	39
Center 4	8.8±1.3	0.37	42
Center 5	8.1±1.2	0.42	47

[a] Determined by Least-Square Linear Combination (LSLC) fitting of Al K-edge X-ray Absorption Near-Edge Structure (XANES) spectra using zeolite ZSM-5 and α-Al_2O_3 as tetrahedral and octahedral Al references, respectively, and a fitting range from 1560.35 to 1574.35 eV.
[b] Integral of the pre-edge region of 1560.35-1565.15 eV, representing tri-coordinated (3-fold) Al.
[c] Determined by peak area of Cu^{2+} and Cu^+ edge from Cu L_3-edge XANES.

B. Additional Figures of Chapter 4
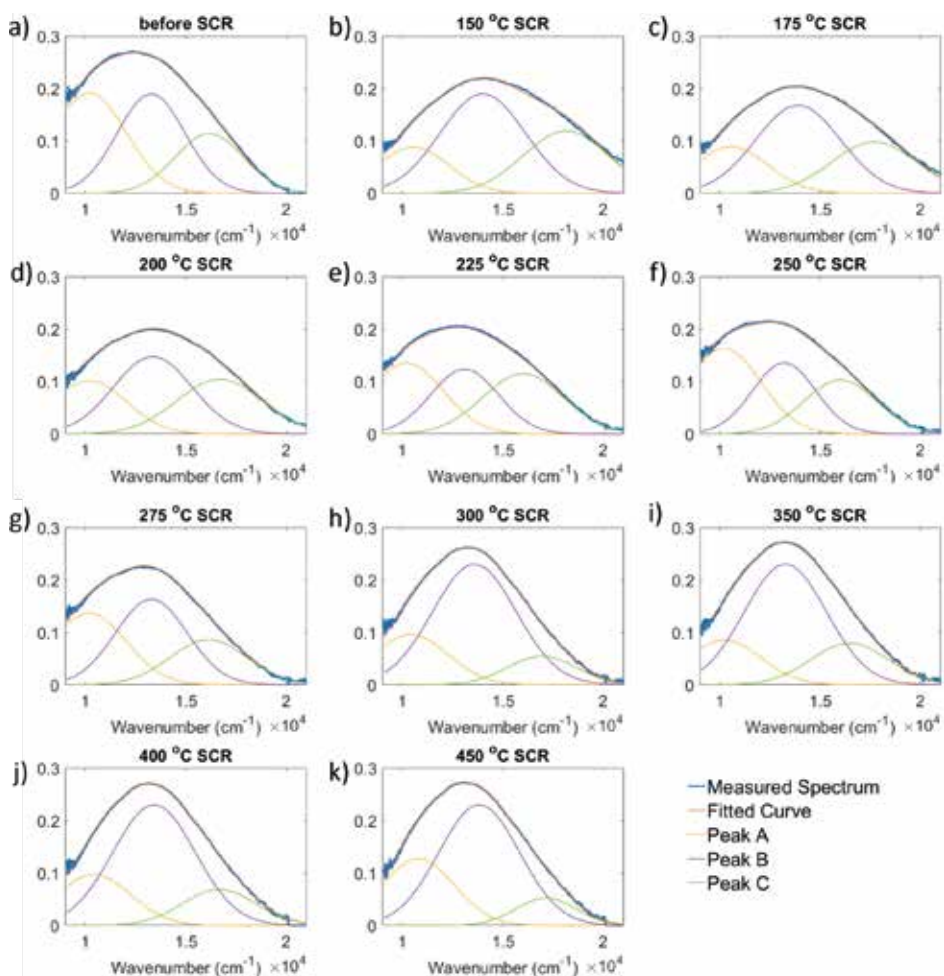
Figure AIII3. Fitting curves and the corresponding bands of the fitting model in the d-d transition region in UV-Vis diffuse reflectance spectra a) before standard NH_3-Selective Catalytic Reduction (SCR) reaction of NO and b-k) under steady-state conditions at different reaction temperatures performed on the fresh zeolite Cu-ZSM-5 material.
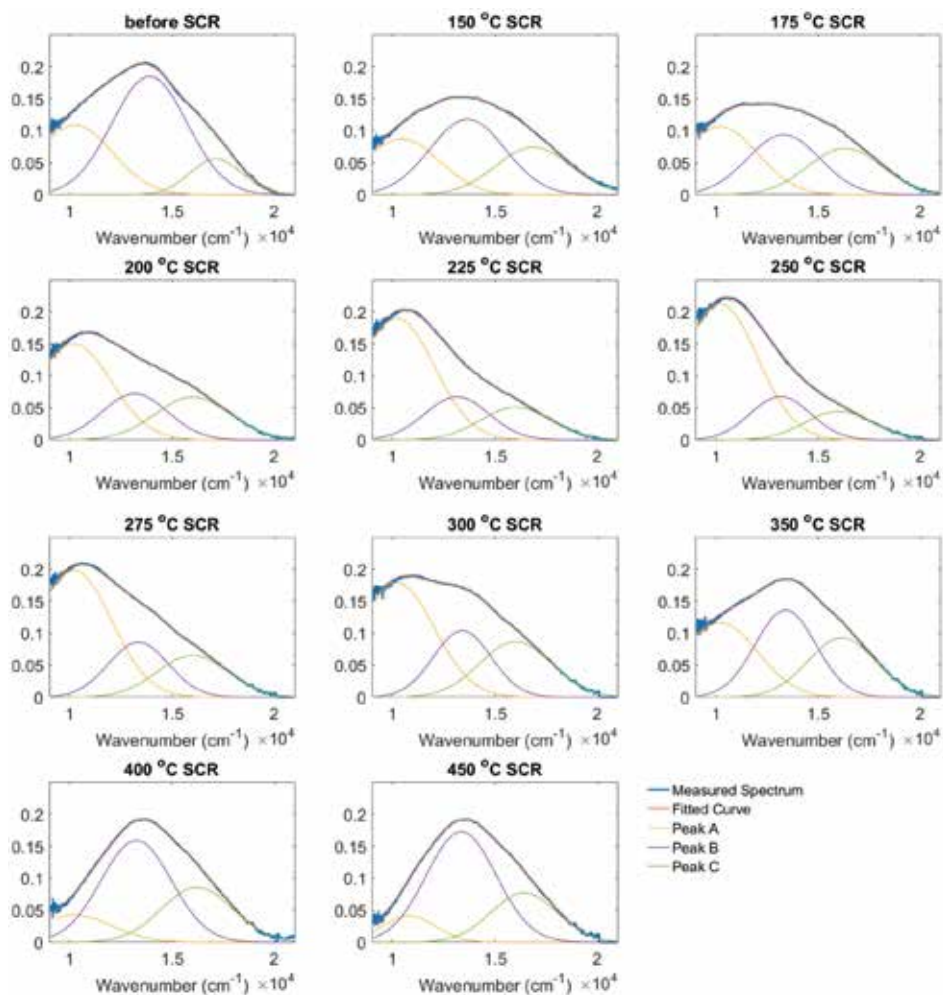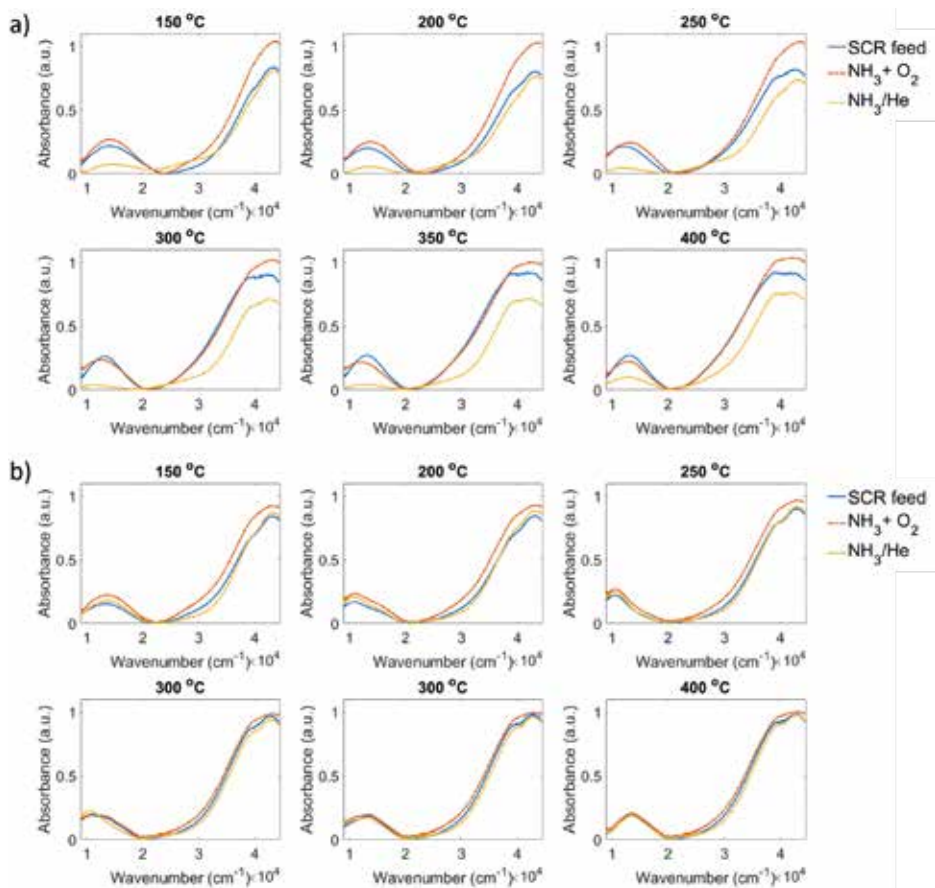
**Figure AIII4.** Fitting curves and the corresponding bands of the fitting model in d-d transition region in UV-Vis diffuse reflectance spectra a) before standard NH$_3$-Selective Catalytic Reduction (SCR) reaction of NO and b-k) under steady-state conditions at different reaction temperatures performed on 850 °C steamed zeolite Cu-ZSM-5 material.

Figure AIII5. UV-Vis diffuse reflectance spectra of a) fresh and b) 850 °C steamed Cu-ZSM-5 in standard NH$_3$-Selective Catalytic Reduction (SCR) reaction (blue), NH$_3$ oxidation reaction (red) as well as NH$_3$/He (yellow) flow at different reaction temperatures between 150-400 °C.
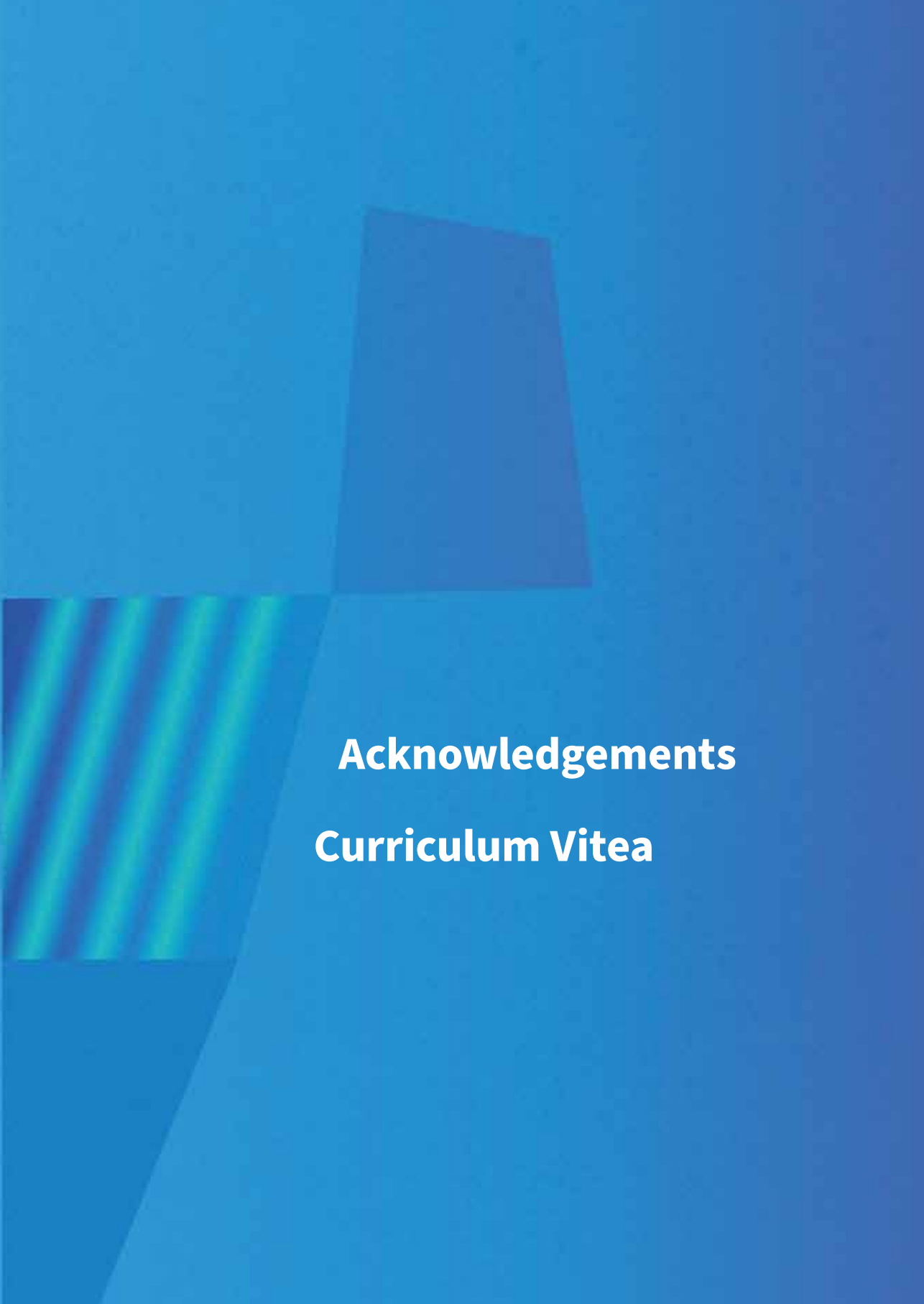
A
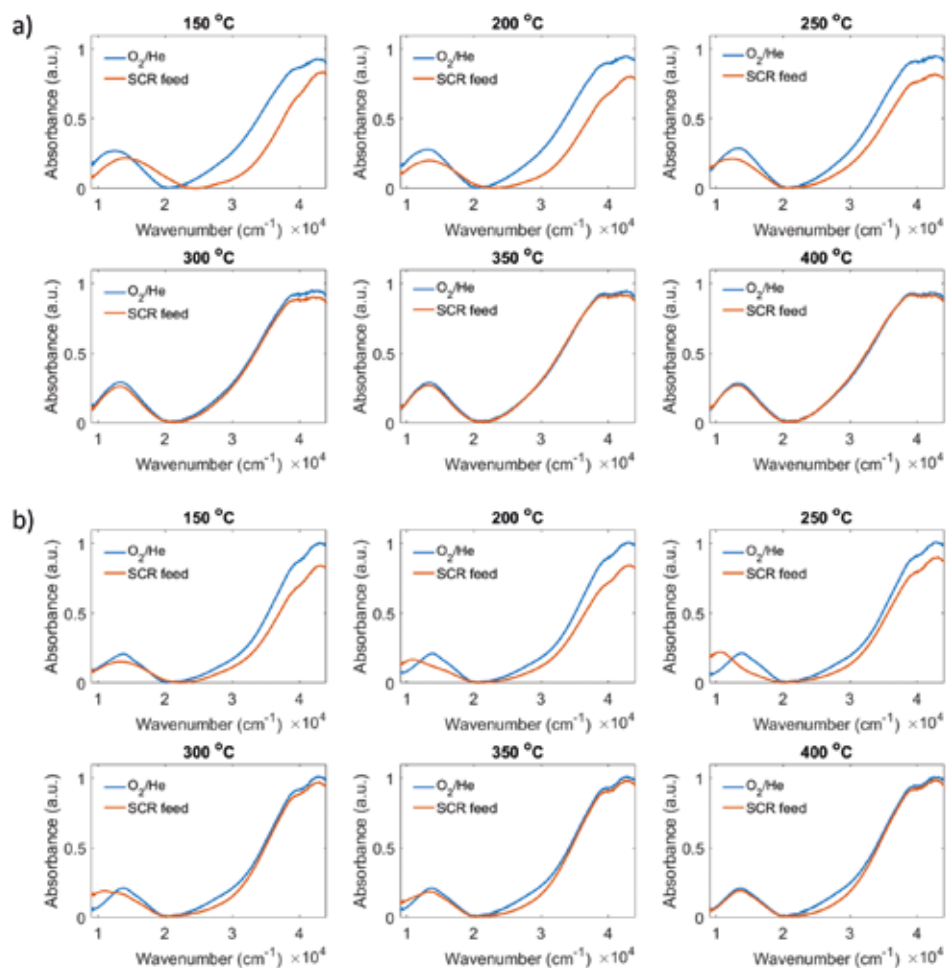
Figure AIII6. UV-Vis diffuse reflectance spectra of the a) fresh and b) 850 °C steamed zeolite Cu-ZSM-5 obtained after calcination during the cooling procedure in O_2/He (blue), and under Selective Catalytic Reduction (SCR) feed (red) at different reaction temperatures between 150-400 °C.

Figure AIII7. NO and NH$_3$ conversion of the NH$_3$-Selective Catalytic Reduction (SCR) of NO (in the temperature window of 150-450 °C) and its reversed cycle (450-150 °C) over the a) fresh and b) 850 °C steamed zeolites Cu-ZSM-5. The corresponding operando UV-Vis diffuse reflectance spectra of the c) fresh and d) 850 °C steamed zeolites Cu-ZSM-5 were also collected in the reaction, and cycle 2 represent the reversed cycle. The comparable catalytic performance and spectroscopic observations in the two NH$_3$-SCR cycles strongly suggest that the evolution of species observed during the first cycle was reversible, and not due to irreversible deactivation and degradation of Cu species (which may nonetheless occur over multiple catalytic cycles or prolonged testing).

147

Acknowledgements

Curriculum Vitea

ACKNOWLEDGEMENTS

I am grateful at this moment, sitting peacefully and taking a trip down the memory lane. It is an important and memorable piece in my life to have joined the Inorganic Chemistry and Catalysis (ICC) group in Utrecht University since October 2017. My PhD journey started in Nankai University (China) in 2015, during which I got a chance to continue my PhD project in Utrecht. During my time in the ICC group, I gained scientific knowledge and developed lab skills, but also experienced a very different working mode from my past research experience in China. This PhD Thesis is the closing chapter that concludes my 3.5 years stay in the ICC group. It could not have been accomplished without the support from my supervisors, colleagues, friends, and families. With this note, I would like to thank all of you sincerely with my feeling of gratitude.

Bert, you are the first person I would like to say thank you to. I am very grateful for the opportunity to perform a PhD project in your group. I can still remember our first meeting right after I arrived in the Netherlands. You told me that the meaning behind scientific research is most important to you and not the publications; and my goal during my PhD should be to develop into an independent researcher. No matter from formal meetings or casual talks, I can see how wide your scope and how deep your scientific insights are. I am really impressed by that. I also appreciate all the chances you gave for participating in beamtrips and international conferences. These are all bonuses in my daily lab and office life. I value every of your suggestion on my research work as well as your encouragement for finishing the thesis. Your positive response from the emails motivated me again and again, especially in the past few months when my motivation was sometimes lacking. Thank you very much for your trust, support, guidance, and the knowledge you shared with me.

Florian, I learnt a lot from you. You gave so much technical support in every research topic I worked on. I had my first experiences with synchrotron-based X-ray spectroscopy and gained basic Matlab coding skills from you. I am very grateful for your kind and patient supervision on the analysis of STXM data and operando spectroscopy data. All the research outcomes are built up based on the countless discussions with you. I am impressed by your sharp eyes on the results, and your cautiousness and logicality in research. I appreciate and enjoy all the discussions and meetings we had, which are always efficient, informative and inspiring, bringing me clarity in mind. New ideas can often arise in the

discussions with you, no matter which topics we discussed. Thank you so much for your time, kindness, and contributions on my research.

Frank, you are so kind and knowledgeable. Thank you for the ideas and inputs you provided when I encountered questions on X-ray spectroscopy and UV-Vis spectroscopy. Our discussions can always end up with the stories of your experiences and opinions on other matters.

Eelco, I also appreciate every meeting you were involved in, providing different angles that I have never thought about. Thanks a lot for your input and ideas.

Prof. Tiehong Chen (Nankai University), thank you for the occasional meetings to follow up my research in Utrecht. I am grateful for your guidance and support for my research and career planning.

Joel, you are a very responsible daily supervisor, with kindness, passion, and sincerity. You introduced me into the group and guided me to start up my own research in the group. Daily discussions with you helped me to adapt to the new group quickly. I am impressed by your high working efficiency, which also pushed me to extend my own limits. Thank you so much for all your suggestions on my research, from experiments design, to data analysis and papers writing. I appreciate for your continuous support even after you have left the group.

Ramon, you are a very good buddy. Although you are busy working for the group in the working days, you can still make time to fix any problem I met in the lab, which sometimes might make you work overtime. And thank you for the experience and knowledge you shared in any of our discussions.

Matteo, I am impressed by your enthusiasm in science. You share the new ideas and opinions on any of the topics we discussed, which I highly appreciate. Also thank you so much for your suggestions on outlining my recent paper.

Rupan, I enjoy the discussion and collaboration with you. Your solid background in physics brought great improvements in our research.

I would also like to thank my STXM beamtrip teammates, Ilse, Iris, Joel, Maarten and Ramon. Your humor and kindness made the trip more joyful. Nikos, Romy, Silvia and Sophie, I am happy to share the lab space with you. Also, many thanks to the technical team and the support teams in our group. The clear division of

work and responsibility enables the group functions smoothly. Dymph, thank you for taking care of many administrative works in the group.

Katarina and Marisol, you are my best friends in Utrecht. We have so many unforgettable moments full of laughter. I cherished our memories of dinners, trips, walks, and 'cycling'. I am happy that we still keep close contact after I went back to China. Your encouragements and support release my pressure and brighten my days. I am so grateful. And Marisol, don't forget our Christmas wish in 2019, keep going!

Fang, thanks for sharing your experience and stories with me although you have left the group for a while. We can have endless talk. I enjoy the time we spent on the trip to Leuven. Hopefully we could meet again soon. Nina and Heba, there are also great memories with you. We can make everything interesting and laugh so hard together. I am so proud that you can inherit my 'professional' dumpling recipes and developed your own styles. Shuang, Yaqi and Xiang, I am also happy to know you, thanks a lot for sharing your nice food to me. They taste much better than the boring food I always have. The dinners and outings we had are always relaxing and joyful!

Christia, I am lucky to have you as my neighbor in the office. I like our casual talks. Kordula and Florian (Zand), I enjoy the coffee break with you and thank you for your Austria herbal drink, Almdudler, if I remember correctly. For the dinner and beers we had together, Beatriz, Carlos, Donglong, Fabiane, Jogchum, Justine, Kang, Katarina, Nazila, Marianna, Marisol, Miguel, Rolf, Sirada, Shuang, Stano, Yaqi, the outings or dinners with you also build up my good memories in Utrecht. I would also like to thank to the Chinese colleagues in our group: Donglong, Fei Chang, Fei Wang, Guangxian, Hongyu, Jiadong, Juan, Kai, Kang, Longfei, Min, Peng, Qijun, Rupan, Shiyou, Shuai, Shuang, Xian, Xiang, Yaqi, Yunchao, I feel less homesick because at least I can still have chance to speak Chinese.

I am happy to know everyone from the new and old ICC group, Angela, Anne-Eva, Bas, Beatriz, Carlos, Caroline, Charlotte, Christia, Daan, Donglong, Egor, Ellen, Erik, Fei Chang, Fei Wang, Florian Zand, Fouad, Giorgio, Guangxian, Guusje, Hebatalla, Hideto, Hiroki, Hongyu, Ilse, Ina, Iris, Javier, Jessi, Jiadong, Jim, Jochem, Joel, Jogchum, Johan, Joren, Joris, Juan, Kai, Kang, Katerina, Katinka, Koen, Kordula, Lars, Laura B, Laura K, Laurens, Lennart, Lisette, Longfei, Luke, Luc, Maarten, Mark, Marianna, Matteo, Max, Michael, Miguel,

CURRICULUM VITEA

Xinwei Ye was born on 2nd of March 1993 in Guangzhou, China. She started a Bachelor in Chemistry in the South China Normal University (SCNU) in September 2011. From 2012, she did her first research project in Guangdong Academy of Agricultural Sciences granted by the *National University Student Innovation Program*. In 2013, she studied in Chung Yuan Christian University (CYCU) in Taiwan, China for one year as a visiting student. Her Bachelor thesis was titled 'Development of on-line Solid-phase Microextraction-Liquid Chromatography-Mass Spectrometry (SPME-LC-MS) for chiral secondary alcohol products analysis of yeast-mediated stereo-selective reduction of ketones' and was selected as the Outstanding Undergraduate Thesis in SCNU under the supervisor of prof. Yifan Luo (SCNU) and prof. Cheanyeh Cheng (CYCU). At the same time, she got a second bachelor's degree of English Language and Literature in SCNU.

In September 2015, she started her PhD in Physical Chemistry in the School of Materials Science and Engineering in Nankai University (NKU) via the *Direct PhD Program* in China. Her research focused on the evolution of transition metal ion under reaction conditions via pseudo in-situ X-ray photoelectron spectroscopy (XPS). The research was performed in the Institute of New Catalytic Materials Science under the supervision of prof. Tiehong Chen. In October 2017, she started her PhD project in the Inorganic Chemistry and Catalysis group under the supervision of prof. Bert Weckhuysen at Utrecht University in the Netherlands. The results of this work are summarized in this PhD thesis, entitled 'Structure-Performance Relationships in the Selective Catalytic Reduction of Nitric Oxide over Copper-Based Zeolites'.